KAUNAS UNIVERSITY OF TECHNOLOGY

TOMAS MATULAITIS

STUDIES OF SYNTHESIS AND PROPERTIES OF BIPOLAR COMPOUNDS FOR ORGANIC OPTOELECTRONIC DEVICES

Doctoral dissertation
Technological sciences, Materials engineering (08T)

2018, Kaunas

This doctoral dissertation was prepared at Kaunas University of Technology, Faculty of Chemical Technology, Department of Polymer Chemistry and Technology during the period of 2013–2017. The studies were supported by the Research Council of Lithuania.

Scientific Supervisor:

Prof. habil. dr. Juozas Vidas GRAŽULEVIČIUS (Kaunas University of Technology, Technological sciences, Materials engineering 08T).

Doctoral dissertation has been published at:
http://ktu.edu

Editor: dr. Armandas Rumšas (Publishing Office ''Technologija'')

KAUNO TECHNOLOGIJOS UNIVERSITETAS

TOMAS MATULAITIS

ORGANINIAMS OPTOELEKTRONINIAMS PRIETAISAMS SKIRTŲ BIPOLINIŲ JUNGINIŲ SINTEZĖ IR JŲ SAVYBIŲ TYRIMAS

Daktaro disertacija
Technologiniai mokslai, medžiagų inžinerija (08T)

2018, Kaunas

Disertacija rengta 2013–2017 metais Kauno technologijos universiteto Cheminės technologijos fakulteto Polimerų chemijos ir technologijos katedroje. Mokslinius tyrimus rėmė Lietuvos mokslo taryba.

Mokslinis vadovas:

Prof. habil. dr. Juozas Vidas GRAŽULEVIČIUS (Kauno technologijos universitetas, technologijos mokslai, medžiagų inžinerija, 08T).

Interneto svetainės, kurioje skelbiama disertacija, adresas:
http://ktu.edu

Redagavo: dr. Armandas Rumšas (leidykla „Technologija")

LIST OF ABBREVIATIONS

TWh – terawatt-hour
OLED – organic light emitting diode
TV – television
TADF – thermally activated delayed fluorescence
UV/Vis – ultraviolet/visible
BCE – before current era
LCD – liquid crystal display
PhOLED – phosphorescent organic light emitting diode
ISC – intersystem crossing
S_0 – ground singlet state
S_1 – the first excited singlet state
T_1 – the first excited triplet state
EQE – external quantum efficiency
k_{ISC} – intersystem crossing rate constant
rISC – reverse intersystem crossing
SOC – spin orbit coupling
MLCT – metal-ligand charge transfer
LCT – ligand-ligand charge transfer
CI – configuration interactions
$Ir(ppy)_3$ – Tris[2-phenylpyridinato-C2,N]iridium (III)
FRET – Förster (fluorescence) resonance energy transfer
DET – Dexter electron (energy) transfer
D – donor
A – acceptor
Å – Angstrom
IP – ionization potential
EA – electron affinity
HOMO – highest occupied molecular orbital
LUMO – lowest unoccupied molecular orbital
IQE – internal quantum efficiency
ΔE_{ST} – singlet-triplet energy splitting
PF – prompt fluorescence
TTA – triplet-triplet annihilation
ε – dielectric constant
CT – charge transfer
^1LE – the first locally excited singlet state
^3LE – the first locally excited triplet state
^1CT – the charge transfer excited singlet state
^3CT – the charge transfer excited triplet state
TAPC – 4,4′-cyclohexylidenebis[N,N-bis(4-methylphenyl)benzenamine]
PL – photoluminescence
PL QY – photoluminescence quantum yield
k_{IC} – internal conversion rate constant

k_{rISC} – reverse intersystem crossing rate constant
k_{rad} – radiative rate constant
k_{TADF} – thermally activated delayed fluorescence rate constant
IC – internal conversion
DF – delayed fluorescence
HFC – hyperfine coupling
RTP – room temperature phosphorescence
PMMA – poly(methyl methacrilate)
E_T – triplet energy
E_S – singlet energy
FIrpic – Bis[2-(4,6-difluorophenyl)pyridinato-C2,N](picolinato)iridium (III)
2CzPN – 4,5-di(9H-carbazol-9-yl) phthalonitrile)
CBP – 4,4′-Bis(N-carbazolyl)-1,1′-biphenyl
mCP – 1,3-Bis(N-carbazolyl)benzene
TCTA – Tris(4-carbazoyl-9-ylphenyl)amine
τ – fluorescence lifetime
τ_{DF} – delayed fluorescence lifetime
DPEPO – bis[2-(diphenylphosphino)phenyl] ether oxide
FWHM – full width at half maximum
mCPCN – 9-(3-(9H-carbazol-9-yl)phenyl)-9H-carbazole-3-carbonitrile
AIE – aggregation induced emission
^{1}H NMR – proton nuclear magnetic resonance
^{13}C NMR – carbon nuclear magnetic resonance
ppm – parts per million
$CDCl_3$ – deuterated chloroform
DMSO-d_6 – deuterated dimethyl sulfoxide
IR – infrared
FT-IR – Fourier transform infrared
ATR-FT-IR – attenuated total reflection Fourier transform infrared
MS – mass spectra
APCI – atmospheric pressure chemical ionization
EI – electron ionization
MALDI-TOF – matrix assisted laser deposition/ionization time of flight
Nd:YAG - neodymium-doped yttrium aluminum garnet
iCCD – intensified charge-coupled device
TGA – thermogravimetric analysis
DSC – differential scanning calorimetry
CV – cyclic voltammetry
THF – tetrahydrofuran
ITO – indium tin oxide
XTOF – xerographic time-of-flight
TOF – time of flight
CELIV – charge carrier extraction by linearly increasing voltage
t_{tr} – transit time
U_0 – surface potential

d – entire thickness of the film
μ – charge mobility
Al – aluminum
DFT – density functional theory
TD-DFT – time-dependent density functional theory
NTO – natural transition orbital
Cu – copper
$Pd(PPh_3)_2Cl_2$ – *bis*-triphenylphosphine palladium dichloride
$Pd(OAc)_2$ – palladium acetate
DPPF – 1,1'- bis(diphenylphosphino) ferrocene
n-Bu_4NF – tetrabutylammonium fluoride
PPh_3 – triphenylphosphine
t-BuOK – potassium *tert*-butoxide
t-BuONa – sodium *tert*-butoxide
$Pd(PPh_3)_4$ – *tetrakis*-triphenylphosphine palladium
dppf – 1,1'-bis(diphenylphosphino)ferrocene
TMHD – 2,2,6,6-tetramethyl-3,5-heptanedione
DCM – dichloromethane
DCB – *o*-dichlorobenzene
DMF – *N,N*-dimethylformamide
DMSO – dimethyl sulfoxide
FW – formula weight
m.p. – melting point
TLC – thin layer chromatography
OHF – optimal Hartree-Fock percentage
XC – exchange-correlation functional
q – amount of charge transferred in excited state
LEB – lowest energy band
HONTO – highest occupied natural transition orbital
LUNTO – lowest unoccupied natural transition orbital

CONTENTS

1. INTRODUCTION

We, humans, are the largest population (more than 7.5 billion) of mammals living on planet Earth [1]. Our history extends over 200,000 years [2,3]. We have proven to be one of the most intelligent and successful species on Earth. However, being the most intelligent also means taking the highest responsibility. Throughout the 200,000 years of history, our population has never been as huge as it currently is. For instance, 100 years ago, our population was only 1.6 billion people [4]. Such sudden growth of population has brought an extensive set of unprecedented challenges since the spread of *advanced technologies* and well-being brought by these technologies is definitely uneven globally [5]. These challenges include globally equal accessibility to medicine, food, living conditions of a higher standard, etc. In the course of maintaining such a huge population, other inevitable issues, such as disproportionate consumption and pollution, develop. The latter issues are of utmost importance. To a large extent, people are dependent on electricity. Urbanization speeds up, and currently almost 60% of the world population live in cities [6]. Life in a city is unimaginable without electricity. Electricity runs everything ranging from such mundane functions as object illumination to electric cars and smart houses fully operated by electric gadgets.

On July 4th, 2017, Swedish car manufacturing company Volvo declared in their Twitter page: *We are committed to electrification, so from 2019 all new Volvo car models will include an electric motor.* [7]. Two days earlier, the founder of Tesla Inc., Elon Musk declared that Tesla's long-awaited, lower-priced Model 3 passed all regulatory requirements for production [8]. The world is going to be electric.

During the last 25 years, the world's demand for electricity doubled (from 10 000 TWh to >20 000 TWh) [9]. Therefore, global necessity to solve the issues concerning *electricity consumption and pollution* is evident. The latter can be improved by using *energy-efficient electricity sources and devices*. The cost of fuel and the cost of waste neutralization generated by the electricity sources are the main factors defining the cost-efficiency of an electricity source. Sun, wind and water are infinite sources of energy on our planet. Electricity generated by solar cells, wind turbines and hydro power plants currently produces negligible amounts of waste compared to the traditional sources, such as fossil fuel or nuclear power. Therefore, the future electricity generation belongs to these renewable, *energy-efficient sources*, solar cells being the most promising among them [10]. On the other hand, the application of *less energy consuming technologies*, especially those including organic light emitting diodes (OLEDs), is an important approach on the way towards *reducing the consumption* of electricity. OLEDs represent an ambitious type of advanced devices which eventually are bound to substitute the majority of common light manipulating sources including light bulbs, car lights, building illumination sources, monitors, TV sets, and screens of most electronic devices [11]. The capacity to convert all the electric charges to light, the low operating voltage, as well as the wide

viewing angle, high brightness, color purity, light weight, flexibility, ability to produce large area panels and avoidance of use of noble metals make OLEDs the most attractive type of devices to be applied [12].

However, the issues of the lifetime and instability of blue-emitting OLEDs have not yet been fully solved [12]. The encapsulation of the device can improve the stability [13]; however, the organic materials used in OLEDs are sensitive to water and oxygen – thus need is observed to develop more oxygen and water tolerant materials. The issue of unstable blue emitters for OLEDs has been known for a relatively long time and has still not yet been solved [12]. This issue comes from the fundamental origin of blue light. The energy of blue light is higher if compared to that of green or red light. In a device, upon electrical excitation, an organic emitter tends to decompose under the action of high energy. Therefore, there is need to develop new and stable organic emitters which would emit in blue and would meet a set of other criteria including thermal and electrochemical stability, color purity as well as efficient exciton harvesting. The development of efficient and stable absorbers for organic solar cells is also an urgent problem.

The aim of this work is the development of new bipolar materials and a comparative study of their properties regarding their use in organic optoelectronic devices. In order to achieve the aim of the thesis, the following objectives were outlined:

- Synthesis, characterization and study of the properties and applicability in OLEDs of new star-shaped triazine derivatives.
- Synthesis of a new *meta*-conjugated derivative of 1,3,5-triazine and carbazole and investigation of its thermally activated delayed fluorescence (TADF) properties.
- Synthesis, characterization and investigation of the structure-property relationship of new carbazole and benzonitrile derivatives.
- Synthesis and comparative study of the properties of new isomeric derivatives of 9,9-dimethyl-9,10-dihydroacridine and benzonitrile.
- Synthesis, characterization and investigation of photovoltaic properties of a new derivative of benzothiadiazole having both donor and acceptor substituents.

Novelty of the work:

- Three new bipolar star-shaped derivatives of carbazole and 2,4,6-triphenyl-1,3,5-triazine were designed, synthesized and characterized. It was established that the introduction of a C–N bond into the molecules, if compared with a C–C bond, results in 0.3 eV higher triplet energy. Compounds are applicable as emitters in OLEDs.
- A new derivative of carbazole and 2,4,6-triphenyl-1,3,5-triazine was synthesized and characterized. A *meta*-linkage pattern of the chromophores was found to be responsible for the higher charge separation in the excited state, which results in a more pronounced

11

charge transfer state and a more efficient TADF if compared to those of the *para*-analogue. The compound is applicable as an emitter in OLEDs.

- Three new blue-emitting isomeric derivatives of 9,9-dimethyl-9,10-dihydroacridine and benzonitrile were prepared and characterized. It was discovered that *ortho*-linkage is responsible for the high-lying triplet state, as well as for the least polarity sensitive [1]CT state among the isomers resulting in the most efficient TADF. The compounds are applicable as emitters in OLEDs.

- A new donor-acceptor benzothiadiazole derivative was synthesized and characterized. It was established that the extension of the electron accepting benzothiadiazole part by means of tetrafluorobenzonitrile resulted in a wide range of UV/Vis absorption of the final molecule reaching 700 nm. The compound is applicable as an absorber in organic solar cells.

Contribution of the Author

The author has designed, synthesized and purified four different series of bipolar organic semiconductors. The author has also performed the theoretical calculations and analysis for all the compounds. In addition, the author has performed and analyzed the results of differential scanning calorimetry, thermogravimetric analysis, infrared spectroscopy, UV/Vis absorption, cyclic voltammetry, steady-state fluorescence, time-resolved fluorescence and temperature-resolved excited state dynamics measurements. The ionization potential and charge mobility investigations were performed in collaboration with dr. Dmytro Volyniuk (Kaunas University of Technology), the results of which were further independently analyzed by the author. The OLEDs described in Chapter 4.1.7. were fabricated with the assistance of dr. Nataliya Kostiv (Lviv Polytechnic University, Ukraine). The OLEDs described in Chapter 4.2.6. were fabricated with the help of prof. Saulius Juršėnas and his team (Vilnius University, Lithuania). The solar cells were manufactured with the help of prof. Karl Leo and his team (Dresden University of Technology, Germany).

2. LITERATURE REVIEW

2.1. Brief History and Understanding of the Phenomenon of Light

Light manipulation nowadays extends far beyond the classical purpose of object illumination. Currently, the use of light in such *smart* technologies as TVs, mobile phones, computer screens, sensors, optical cables, etc., is to transfer information. Also, light harvesting and conversion to electricity via solar cells has become a most sophisticated type of technologies. To begin with, we may wonder what *the light* is. *The light* is the brightness, radiant energy that makes things visible. In the Proto-Indo-European language the root '*leuk-*' means '*light, brightness*'. However, what is *the light* and how do we define it? In scholarly terms, *the light* usually refers to the part of electromagnetic radiation (solar, electric bulb, etc.) which is visible to the human eye. Electromagnetic radiation is a very broad range of radiation which has no upper and lower limits in terms of frequency/energy. Historically, it is roughly divided into six parts, as **Fig. 2.1.1** presents: gamma rays, X-rays, ultraviolet light, visible light, infrared, microwaves and radio waves.
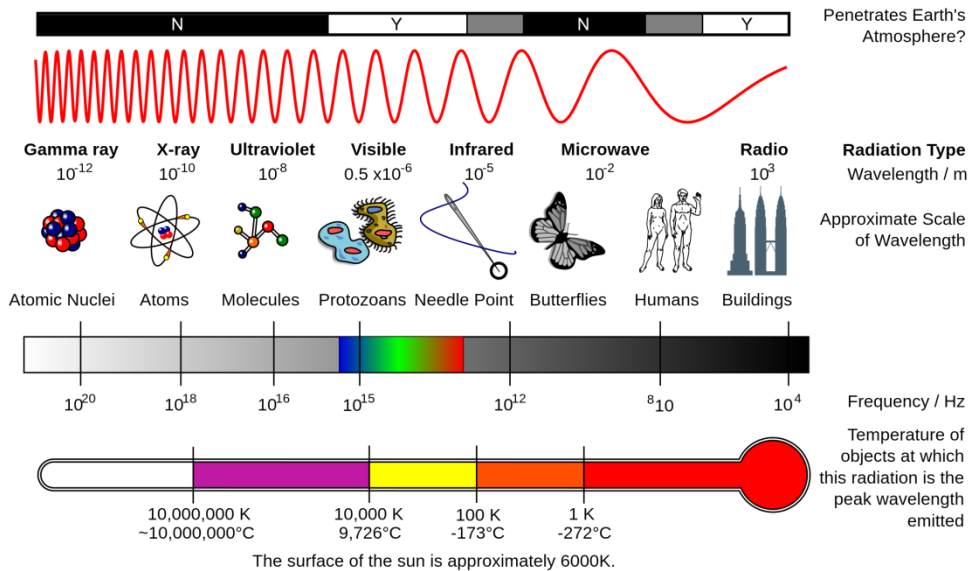
Figure 2.1.1. The electromagnetic spectrum

The earliest attempts to explain why we see and what the light is date back to the times of Ancient Greece (ca. 500 years BCE), when philosopher and mathematician Pythagoras proposed that *the sight is caused by visual rays emanating from the eye and striking objects*. Even though nowadays such an explanation may sound heretic, one may find it remarkable that the attempt of Pythagoras to explain the phenomenon of light was globally rejected only 1500 years later by Arab scientist al-Haytham who opined that *the vision is passive*

reception of light rays reflected from objects rather than active emanation of light rays from the eyes.

Further studies of the light and optics emerged only in the beginning of the 17th century when the first telescopes were invented. Two competing models of light, the first defining light as a collection of fast-moving particles and the second treating light as a propagating wave, were advanced. The most prominent scientist of the *particle theory of light* was Isaac Newton (1642–1727) who discovered that the white light consists of a mixture of colors. He also postulated that the light particles of different colors have slightly different masses leading to different speeds in transparent media and hence to different angles of refraction. This model survived until the beginning of the 19th century, when *the wave nature of light* overwhelmed it. English scientist Thomas Young (1773–1829) performed a series of diffraction experiments and concluded that *light possesses the behavior of a wave*. However, the wave theory of light was unable to explain the origin of light. In the 1860s, Scottish scientist James Clerk Maxwell described *light as a propagating wave of electric and magnetic fields* and claimed that the coupled electric and magnetic fields are travelling as waves at the speed of light. Grounded by Michael Faraday's (1845) and Heinrich Hertz's (1888) experiments, Maxwell's theory of *light as electromagnetic radiation* boosted up the development of the modern radio, radar, television, electromagnetic imaging, and wireless communications.

However, in the year 1900, German physicist Max Planck proposed a model which matched the experimental results of the blackbody spectrum [14]. Moreover, he suggested that even though light was being considered to be of the origin of electromagnetic waves, these waves could gain or lose energy only in finite amounts related to their frequency. Five years later, another physicist Albert Einstein shook the grounds of the light theory with the declaration that electromagnetic radiation itself is granular, and it consists of *quanta* (particle), each with definite energy of *hf* (*h* – the Planck constant, *f* – the frequency) [15]. Einstein supported his photon hypothesis with analysis of the photoelectric effect, a process in which electrons are ejected from a metallic surface illuminated by light. Einstein supposed that some minimum amount of energy is required to liberate an electron from a surface and that only photons with energies greater than this minimum can induce electron emission. This requires minimum light frequency as well, as shown by the experiment.

Eventually, in the year 1913, Danish physicist Niels Bohr introduced the model that an atom consists of a tiny positively charged heavy core called a nucleus which is surrounded by light, planetary negative electrons revolving in circular orbits of arbitrary radii [16]. Light, as he proposed, radiated from hydrogen atoms only when an electron made a transition from an outer orbit to one closer to the nucleus. The energy lost by the electron in the abrupt transition is precisely the same as the energy of the quantum of the emitted light. Bohr's atomic model is presented in **Fig. 2.1.2**.
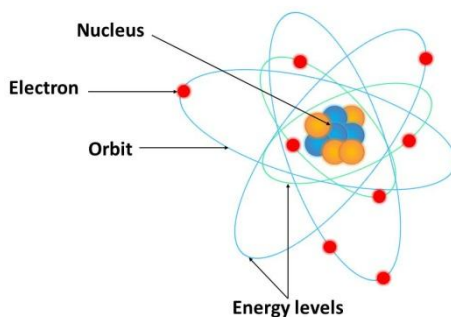
Figure 2.1.2. Bohr's atomic model

2.2. OLEDs. Working Principles, Structures and Types

2.2.1. OLED Structures and Excitation Types

The current understanding of the phenomenon of light based on Bohr's model has allowed achieving tremendous improvement in the field of the light harvesting technologies. Among the energy-efficient technologies, OLEDs and organic solar cells are on the edge of the market. OLEDs can be and are being applied in the screens and displays, as well as in solid state lightning applications [17]. The advantages of OLEDs include light weight, flexibility, absence of need to use rare elements, low costs (especially for large area illumination applications), a greater contrast ratio compared to LCD displays, a wider viewing angle, etc. However, there are some disadvantages which have to be solved in order to unleash the OLED market. These include the short lifetime of OLEDs, color degradation, efficiency and the lifetime of blue-emitting organic semiconductors and OLEDs themselves, etc. Among these issues, the latter is of great interest among scientists all over the globe. During the last 10 years, the amount of research articles concerning the development of blue-emitting compounds for OLED applications increased ca. 2.4 times as shown in **Fig. 2.2.1**. The data is taken from five largest and most frequently quoted publishers – *American Chemical Society*, *Royal Chemical Society*, *Wiley Online Library*, *ScienceDirect* and *Nature*.
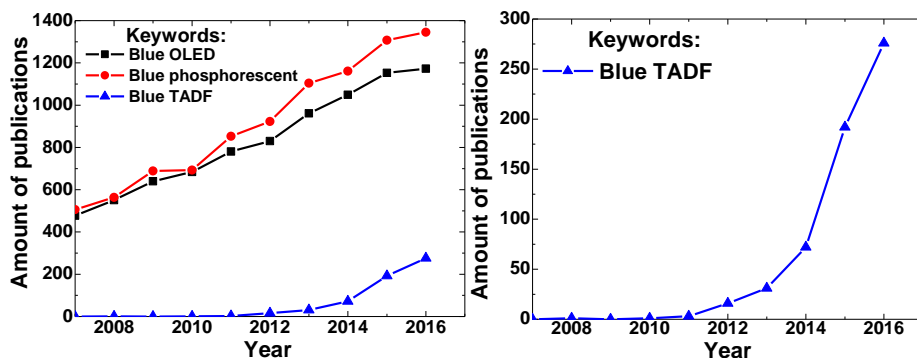
Figure 2.2.1. Statistics on the yearly amount of publications about blue-emitting materials and OLEDs within the period of years 2007–2016

We also performed a search for the year 2017, but since this search was performed on July 12, 2017, we obtained results which are not relevant to fit within the yearly statistics. However, the trends are maintained, and by the end of this year, an even higher amount of publications is expected to appear on the topic of blue-emitting materials for OLEDs, which points out the relevance of the topic. Moreover, in the right chart of **Fig. 2.2.1.**, one can observe the exponential growth of the research on the topic of *blue thermally activated delayed fluorescence* (TADF).

Among the energy-efficient OLEDs, we can single out two distinctive categories – *phosphorescent* (PhOLED) and *TADF* OLEDs. The principal differences between these two groups of OLEDs are the different light emission mechanisms occurring within the emissive layer. In order to better understand these differences and identify the criteria needed to design new and stable compounds for blue OLEDs, at first we must take a look at the OLED structure. As it is depicted in **Fig. 2.2.2.**, an OLED consists of the following layers: the transparent substrate (glass, etc.), the anode, the hole transport layer (HIL), the emissive layer (EML), the electron transport layer (ETL), and the cathode. We should note that additional charge injection/blocking layers can be added in order to improve the performance of a device. The emissive layer usually consists of a blend of the host-guest system where the host transports and transfers both positive and negative charges to the guest thus exciting the guest. After the excitation, the guest emits light. There are two different ways of excitation: optical and electrical excitation. The device is being driven by electrical excitation; however, in most spectroscopies used in the characterization of organic semiconductors, optical excitation takes place. The differences between optical and electrical excitations are visually demonstrated in **Fig. 2.2.3**.
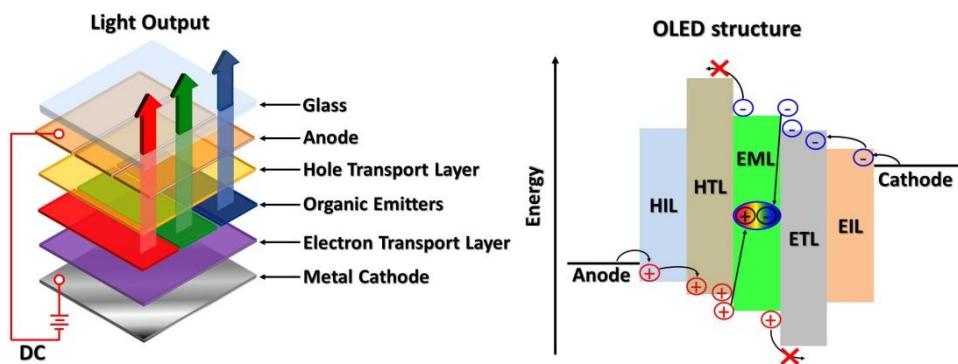
Figure 2.2.2. Schematic representation of OLED

When an organic semiconductor (the emitter) is optically excited (transition S_{0-1}), only singlet excitons[1] are produced. As it can be seen in **Fig. 2.2.3.**, after optical excitation, there are the following possible ways of deactivating the excited emitter: emission via fluorescence (S_{1-0}), nonradiative decay (S_{1-0}),

---

[1]Electronic excitation (recombination of charges) produces an exciton – a bound electron-hole (neutral quasi-particle) capable of migrating and transferring its energy [174].

intersystem crossing (ISC) from the excited singlet (S_1) to the triplet (T_1) state, and, if possible, emission via phosphorescence, or nonradiative decay (T_1-S_0). We must also note that here we only present a simplified scheme along with the processes occurring after excitation. In case of electrical excitation, electrical charges travel from electrodes and recombine within the sandwiched emitter. Differently from optical excitation, this electric charge recombination within the emitter is expected to produce singlet and triplet excitons at a ratio of 1:3 as it is dictated by the spin statistics [18]. Such differences pertaining to the origin of excitation lead to fundamental drawbacks of the devices on fluorescent materials since phosphorescence of purely organic compounds normally does not occur at room temperature thus making fluorescent OLEDs able to convert the maximum of 25% of electricity to light. Moreover, the emissive layer in OLED is sandwiched between other layers, and the cathode is usually non-transparent, overall resulting in up to 80% of electrically generated light getting trapped within the device [18], which leads to the maximum possible external quantum efficiency (EQE) values of no more than 5% in ideal fluorescent OLEDs.
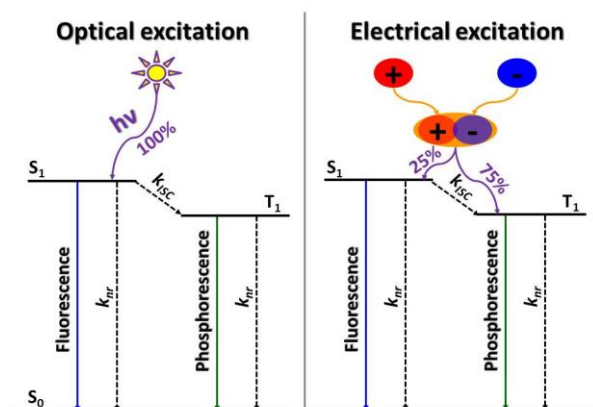
Figure 2.2.3. Differences between optical and electrical excitation of organic/hybrid semiconductors. S_0 – ground state, S_1 – the first excited singlet state, T_1 – the first triplet state, hv – optical excitation, k_{nr} – nonradiative rate constant, k_{ISC} – intersystem crossing rate constant

2.2.2. Phosphorescent OLEDs and Excitation Harvesting Mechanisms

The fundamental limitations of fluorescent OLEDs urge scientists to search for ways of utilizing those 75% of triplet excitons formed after the electrical charge recombination. As in usual organic semiconductors the energy gap between the first singlet and the triplet states is large (>0.5 eV), there is no possibility for triplet excitons to undergo reverse intersystem crossing (rISC) back to the singlet state, so usually 75% of triplet excitons deactivate via nonradiative pathways. However, this problem of radiative utilization of triplet excitons can be solved if a heavy metal atom (iridium, platinum, gold, etc.) is used. Back in the year 1998, Baldo et al. [19] reported organometallic complexes as phosphorescent emitters in OLEDs which utilized nearly all the excitons generated from charge recombination within the device. The usage of the organometallic complex was

found to be capable of harvesting not only triplet excitons, but singlets as well, since due to the presence of a heavy metal ion, strong spin-orbit coupling (SOC) induces fast and efficient ISC thus converting singlet excitons to the triplet ones and radiating up to 100% of electrically generated excitons via phosphorescence. The key factor in these complexes is the involvement of *d* orbitals of the heavy metal atom (**Fig. 2.2.4.**) into the excitation processes. Excitation affects *d* orbitals of the metal and π orbitals of the organic ligand – thus there are two types of transitions arising in the course of excitation: dπ*, the metal-ligand charge transfer (MLCT), and ππ*, the ligand-ligand charge transfer (LCT) [19–21]. This produces four types of electronically excited states: two singlets ([1]LCT and [1]MLCT), and two triplets ([3]LCT and [3]MLCT). SOC and configuration interactions (CI) between these states mix all of them efficiently, and, in such a way, 100% of excitation can be converted into light via phosphorescence in these organometallic complexes.
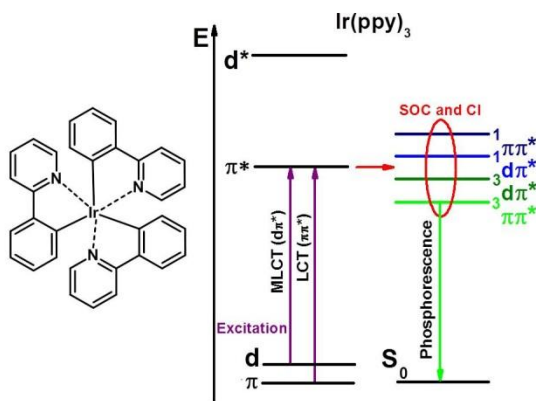
Figure 2.2.4. Chemical structure and energy diagram of the most important orbitals and states in Ir(ppy)$_3$. SOC – spin-orbit coupling, CI – configuration interaction

However, in order to construct an efficient device, only the use of the organometallic complex usually is not sufficient since most organometallic complexes suffer from severe concentration quenching effects including emission quenching and triplet-triplet annihilation [20]. In order to solve these issues, the emitter must be doped into a suitable host. A suitable host must ensure efficient energy transfer to the emitter. Energy can be transferred by employing three processes: (i) Förster (fluorescence) resonance energy transfer (FRET) [22], (ii) Dexter electron (energy) transfer (DET) [23], and (iii) direct recombination of charges on the guest. The different origin of these processes gives rise to different criteria required to be fulfilled by the host in order to achieve efficient energy transfer. To start with, the driving force of FRET is the Coulomb interaction between the electrons of the host and the guest. After the excitation of the host, an excited electron nonradiatively comes back to the ground state of the host. If the energy of this electron is sufficiently high and the guest is within a distance of 10 nm from the excited molecule of the host, the repulsive Coulomb force will start interacting between these adjacent electrons of the host and the guest, and the

18

guest electron will get excited upon being driven by this repulsive force (**Fig. 2.2.5a.**). For this to occur, the main condition is the overlapping of the host's emission with the absorption of the guest (**Fig. 2.2.5b.**).
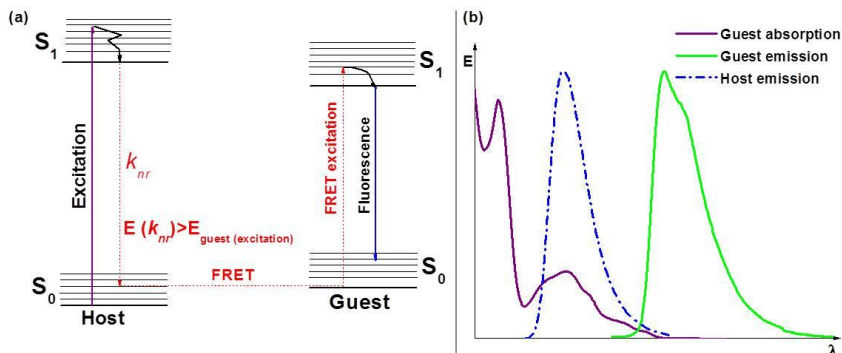
Figure 2.2.5. FRET mechanism and representative spectral overlap of host emission and guest absorption

   It is of utmost importance to note that FRET involves only singlet-singlet transitions since such transitions are spin-allowed. Triplet excitons formed on the host during electrical excitation, however, would not be affected by FRET. Thus we come to the second type of energy transfer – the Dexter electron transfer. The main difference between FRET and DET is that, during DET, actual electron transfer occurs (it can be either inter- or intramolecular), whereas FRET is energy transfer. Since electron exchange is involved in DET, the efficiency of DET exponentially depends on the distance between the host and the guest (in case of the intramolecular process – between the donor (D) and the acceptor (A) fragments within the molecule) and the maximum limit for DET to occur is as short as 10 Å (1 nm) [20]. The energetic levels of singlet and triplet excitons of the host and the guest should match for DET to occur as well. In other words, the host and the guest should share the orbital clouds; the wave functions should overlap (**Fig. 2.2.6.**). If these conditions are satisfied, then the electron jump from S_1 (T_1) level of the host to S_1 (T_1) level of the guest will occur, and also the subsequent electron transfer from the guest's to host's ground state will take place. In such a way, the host will transfer its excitation to the guest. In device applications, DET is very important since it enables 75% of electrically generated excitons to be transferred from the host to the guest. If the guest in use is an organometallic complex, it will further successfully harvest these triplets, as well as singlets, and will convert up to 100% of the generated charges to light.
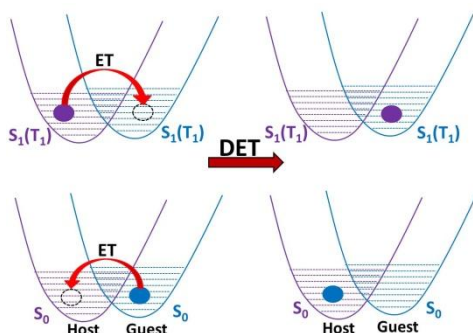
Figure 2.2.6. Dexter electron transfer process

For direct recombination of charges on the emitter, the following criteria must be met: the energetic levels of the host – the ionization potential (IP) and electron affinity (EA) (often referred to as HOMO/LUMO) – should straddle the IP and EA levels of the guest. Moreover (which is also of major importance), the host should possess bipolar and balanced charge carrier mobility in order to be able to simultaneously carry the positive and negative charges to the guest. Other factors, such as the thermal, electrochemical and morphological stability, are highly desirable as well. Ultimately, we should emphasize that efficient triplet harvesting by the guest can only be achieved if the T_1 level of the host is larger than that of the guest (in order not to result in the energy back transfer from the guest to the host).

To summarize, the appropriate host materials should:

- be chemically, thermally and electrochemically stable;
- possess the energy level of the first triplet state (T_1) higher than that of the guest;
- possess bipolar and balanced charge carrier mobility;
- possess IP and EA levels which would straddle the ones of the guest;
- possess the spectral overlap of their singlet emission with the guest's absorption.

2.2.3. Thermally Activated Delayed Fluorescence Phenomenon and Requirements for the Emitters

Even though organometallic complexes provide a possibility to harvest all the excitons and achieve up to 100% of internal quantum efficiency (IQE), still PhOLEDs bring us to a major issue – the use of expensive rare metals. Even though the amount of these metals (iridium, platinum, etc.) within the device is relatively small, their resources are limited, and in the long term perspective, it would result in the global need to substitute these non-renewable elements within the OLEDs. Due to this, another urgent topic that scientists all over the world are currently working on is the application of the thermally activated delayed fluorescence (TADF) phenomenon in OLEDs. Discovered 56 years ago [24], TADF was applied to OLEDs for the first time only 5 years ago by Adachi and

team [25]. TADF offers the possibility to harvest all the excitons electrically generated in the device. Differently from PhOLEDs, where excitons are harvested by the means of the heavy metal atom effect, TADF offers an opportunity to harvest up to 100% of excitons by using purely organic compounds thus excluding the use of heavy metals. Such a revolutionary application of purely organic compounds as emitters which are capable of harvesting 100% of excitons has exponentially accelerated the interest of researchers worldwide in exploring this phenomenon (**Fig. 2.2.1.**).

Commonly, organic semiconductors possess the energy gap between the lowest singlet and triplet states (ΔE_{ST}) larger than 0.5 eV. However, if we design organic compounds according to a specific manner, it is possible to achieve the reduced ΔE_{ST} gap of <0.5 eV (actually, efficient TADF occurs if the ΔE_{ST} gap is <0.1 eV), which enables the possibility of thermally assisted reverse intersystem crossing (rISC) from the higher vibrational levels of the first triplet state (T_1) to the first singlet state (S_1). The resulting emission is of the same spectral characteristics as fluorescence, and only its lifetime is a few orders of magnitude higher than that of the prompt fluorescence (PF) which is resolved by direct singlet exciton generation. These processes are presented in **Fig. 2.2.7**.
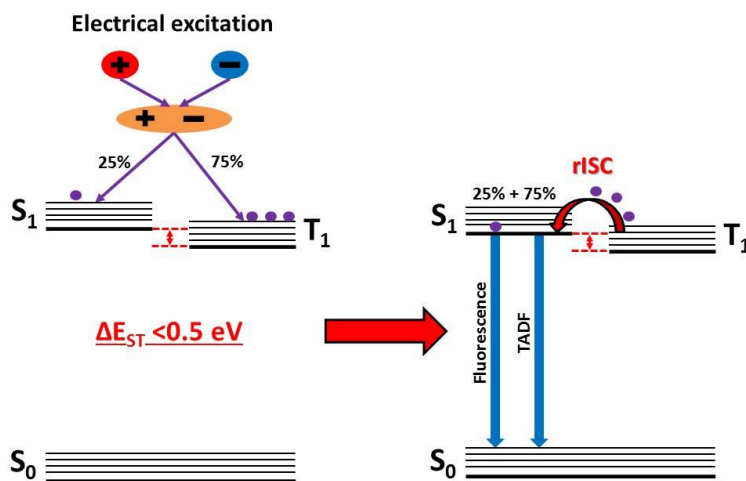
Figure 2.2.7. A simplified scheme of the TADF process

After the first application of TADF in OLEDs, more and more reports covering all-color highly efficient OLEDs have been appearing, and some OLEDs even exceeded >20% values of EQE [26–37]. However, the lion's share of the reported emitters showed a different photophysical behavior, and the earlier proposed mechanism (**Fig. 2.2.7.**) proved to be insufficient to explain the obtained results. Significant scientific efforts, including theoretical [38–44] and mechanistic approaches [45–54], were invested in revealing the mechanism behind the efficient OLEDs. However, debates within the scientific community are still ongoing, and we are still bound to obtain exhaustive explanations of the TADF mechanism.

Probably the most significant study on the TADF mechanism was performed by Monkman's group [43,46–53,55,56]. We shall overview some of their recently reported compounds in order to fluently explain the sequence of the factors influencing TADF. The most important examples of compounds reported by Monkman and peers are presented in **Fig. 2.2.8**.

Figure 2.2.8. Structures of compounds **I–X**

These compounds can roughly be divided into two groups: 'linear' compounds **I**, **III**, **V**, and 'angular' compounds **II**, **IV**, **VI–X**. Starting with the 'linear' and 'angular' compounds, Dias et al. [45] investigated how the CT properties depend on the electron donating and accepting strength of chromophores, and also how the change in the substitution pattern (from 'linear' to 'angular') develops, etc. The 'linear' substitution was found to decrease the intensity of phosphorescence independently from the D and A moieties in use. In the meantime, when the 'angular' substitution was used, and a heteroatom was present within the molecular structure, strong phosphorescence was observed even at room temperature during steady-state measurements. The necessity of a heteroatom to be present in the molecular structure of a CT compound in order to achieve high intensity delayed emission (phosphorescence and/or TADF) revealed that the nπ* orbitals play a fundamental role within the photophysics of delayed emission. Moreover, it was discovered that the 'linear' compounds demonstrated

22

DF via triplet-triplet annihilation (TTA), whereas the 'angular' ones showed intense TADF in the polar media. The increase of the electron accepting strength of the inner chromophore among the series (compounds **VII**→**IX**→**VIII**→**II**) resulted in higher CT energies and a stronger contribution of TADF. However, in low polarity media, emission from ^{1}LE states was observed, and efficient TADF was observed in high polarity media (ethanol, dielectric constant ε=24.5). Nonetheless, Jankus et al. [57] fabricated efficient OLEDs containing the most promising compound **II**. OLED exhibited >14% EQE, whereas compound **II** was found not only to successfully harvest up to 100% of triplet excitons but also to form efficient exciplexes with the 4,4′-cyclohexylidenebis[*N,N*-bis(4-methylphenyl)benzenamine] (TAPC) host.

Encouraged by the results obtained from compound **II**, Dias et al. [46] conducted thorough photophysical investigation and provided the OLED data of the new compound (**XI**). In this publication, the authors presented a detailed mechanism of TADF occurring in **XI**. This compound differs from the previously reported **II** in terms of the donor moiety – phenothiazine – which was used instead of carbazole. The use of the inner six atom-membered ring possessing a donor resulted in donors perpendicularly oriented to the acceptor. Moreover, phenothiazine was found to be a stronger donor than carbazole; consequently, **XI** was found to possess only ^{1}CT emission even in nonpolar media, such as methylcyclohexane (ε=2.02). In the meantime, T_1 level was found to be of the same energy as S_1 in methylcyclohexane, resulting in ΔE_{ST} gap as small as ~0.03 eV. A three-layered OLED was fabricated, and it reached EQE values as high as ~16%. It was confirmed that in OLED, nearly 100% of triplet excitons were harvested by **XI**, and that efficient emission via TADF was achieved (PL QY within the device reached ~60%). Based on their profound photophysical investigation, the authors proposed a TADF mechanism occurring in **XI** and similar molecular structure compounds (**Fig 2.2.9.**).
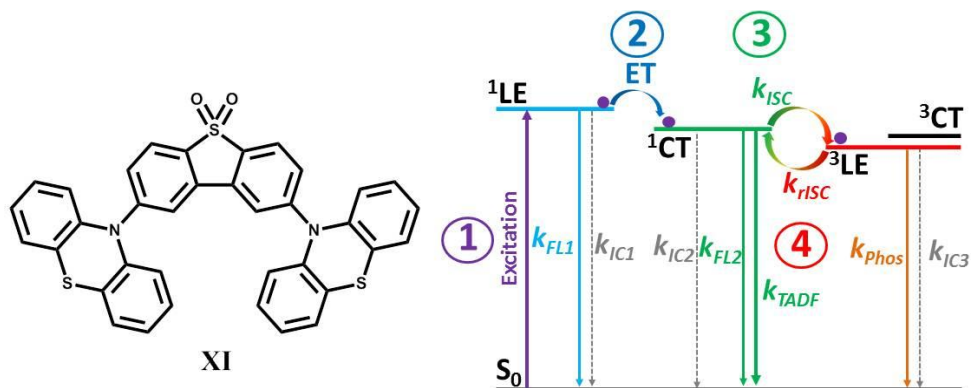

Figure 2.2.9. TADF mechanism in compound **XI**

The excited state processes occur, as follows: the locally excited singlet state of the donor moiety (^{1}LE) is populated upon excitation (①, **Fig. 2.2.9.**). Then, electron transfer from D to A occurs, and the charge transfer excited singlet state (^{1}CT) is populated (②, **Fig. 2.2.9**), which is followed by ISC (③, **Fig.**

23

2.2.9.). As shown by Dias et al. [46,56], in order to achieve efficient TADF, it is required to satisfy the following: $k_{ISC} \gg k_{FL1}+k_{IC1}$, and the rate of rISC ($k_{rISC}$) should be higher than those of phosphorescence and internal conversion (IC) from the triplet to the ground state ($k_{rISC} \gg k_{Phos}+k_{IC3}$). In such a way, the ^{1}CT state will be efficiently populated via rISC (④, **Fig. 2.2.9.**). The total emission of the TADF emitter (Φ_F) can be described by equation (1):

$$\Phi_F = \Phi_{PF} + \Phi_{DF} = \Phi_{PF} \frac{1}{1-\Phi_{ISC}\Phi_{rISC}}; \tag{1}$$

Here, Φ_{PF} is the yield of prompt emission, Φ_{DF} stands for the yield of delayed emission, Φ_{ISC} denotes the triplet formation yield, and Φ_{rISC} represents the yield of singlet states formed by rISC. If the compound under investigation shows a high intensity ratio between prompt fluorescence (PF) and delayed fluorescence (DF) ($\Phi_{PF}/\Phi_{DF} \geq 4$), the triplet formation yield can thus be easily derived from equation (2):

$$\Phi_{ISC} = \frac{\Phi_{DF}/\Phi_{PF}}{1+\Phi_{DF}/\Phi_{PF}} = \frac{\Phi_{DF}}{\Phi_{PF}+\Phi_{DF}}. \tag{2}$$

One of the easiest and the most accurate ways in determining the triplet formation yield (Φ_{ISC}) is to perform a steady-state PL experiment in ambient and degassed atmospheres and to compare the intensity ratios of these PL spectra. Since triplet states are easily quenched by the atmospheric oxygen, the PL spectrum obtained in ambient conditions is proportional to Φ_{PF}; subsequently, the PL spectrum, obtained in the oxygen-free atmosphere is proportional to the sum of PF+DF, i.e. $\Phi_{PF}+\Phi_{DF}$. Having in mind that both PF and DF come from the same S_1 state, the ratio of these integrated PL spectra therefore gives Φ_{PF}/Φ_{DF} according to equation (3):

$$\frac{\int I_{DF}^{O2\,free}(\lambda)d\lambda}{\int I_{PF}^{O2}(\lambda)d\lambda} = \frac{\Phi_{PF}+\Phi_{DF}}{\Phi_{PF}} = 1 + \frac{\Phi_{DF}}{\Phi_{PF}}. \tag{3}$$
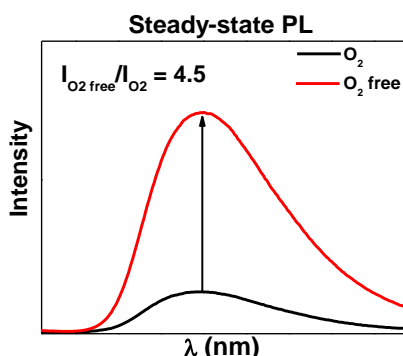

Figure 2.2.10. An example of the steady-state photoluminescence experiment performed in ambient and degassed atmosphere

For example, upon degassing the sample, an increase was observed in the PL intensity of ca. 4.5 times (**Fig. 2.2.10.**). Following equations (2) and (3), we obtain $\Phi_{PF}/\Phi_{DF}=3.5$ and $\Phi_{ISC}=78\%$. Other relevant photophysical parameters

(fluorescence quantum yield (PL QY), lifetimes of PF, DF, etc.) can be then determined by employing the usual techniques, and the relative rate constants can be estimated by using classical derivations [58,59]. By comparing the rate constants of all the relevant photophysical processes, one can build up the mechanism of the excited state dynamics in the compound under investigation.
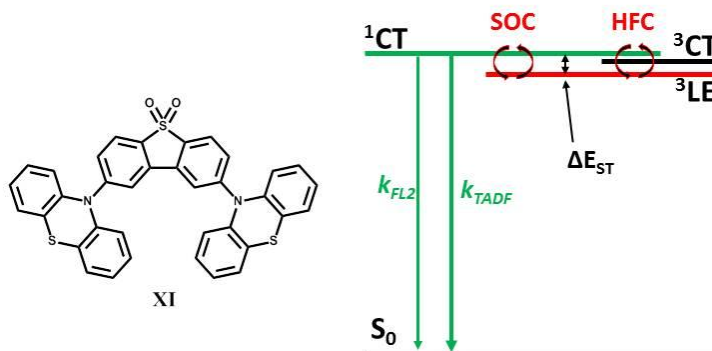

Figure 2.2.11. Driving forces of TADF in compound **XI**

Now let us take a look at the driving forces of TADF. The rISC involves transition between the singlet and triplet states. Thus there are two types of driving forces for rISC to appear: the spin-orbit coupling (SOC) and the hyperfine coupling (HFC) (**Fig. 2.2.11**). There is no heavy metal atom which would ensure efficient mixing of singlet and triplet states via its *d* orbitals. However, since the organic compound is designed in a special way (D and A are perpendicular to each other and are electronically weakly coupled), the former states are energetically close, and this energy is sufficient to couple them and enable SOC. This SOC is not that strong if we compare it to the heavy metal atom-derived SOC; however, it is enough to be the main driving force for TADF. It should be noted that SOC occurs between the states of different orbital origins (i.e. ^{1}CT and ^{3}LE, not ^{1}CT and ^{3}CT), since a prerequisite for SOC is a change in the orbital angular momentum [60]. Therefore, as various authors proved both experimentally [46,48,49] and theoretically [43,52], the crucial ΔE_{ST} gap for efficient TADF is the one between ^{1}CT and ^{3}LE states. Moreover, it was demonstrated that hyperfine coupling (HFC) provides minor contribution to the rISC process in **XI** since as soon as the energies of ^{1}CT and subsequent ^{3}CT states are lowered when compared to ^{3}LE energy, a significant decrease in TADF intensity is observed [46].

The polarity-sensitive behavior of the excited states involved in TADF allowed Etherington et al. [52] to propose three types of a TADF mechanism occurring in **XI** and similar compounds dispersed in different polarity media. The triplet state of local excitation, i.e., ^{3}LE, is polarity-insensitive. Thus its energy remains of the same value independently of the polarity of the media where the compound under consideration is dispersed. However, the increasing polarity of the surrounding media stabilizes the CT states thus lowering their energy. This is how the three types of polarity-dependent mechanisms appear for triplet harvesting in **XI** and other compounds of a similar structure (**Fig. 2.2.12.**). For

25

example, compound **XI** is dispersed in the rigid nonpolar host − cyclo olefin polymer *Zeonex*. In such a rigid (the glass transition temperature of *Zeonex* is >100 °C) and nonpolar matrix, the energy of the CT states of **XI** was found to be higher than that of [3]LE [52]. The internal conversion (IC) from the vibronically coupled [3]CT state to the lower-lying [3]LE state takes place and enables SOC to transfer excitons from the [3]LE state to the [1]CT state (Type I mechanism). The ideal case of triplet harvesting would appear to be the Type II mechanism when all the states involved are in resonance, and both SOC and HFC would efficiently harvest all the triplet excitons with minimal non-radiative losses. However, if the polarity of the host increases (whereas the rigidity decreases), the CT states are getting more stabilized; thus they can become lower in energy compared to the [3]LE state. This is illustrated by Type III TADF mechanism. It is noteworthy that this is a lower efficiency mechanism in comparison with Type I, since, here, IC from the higher-lying [3]LE state will take place prior to the rISC, and the [3]CT state will become a 'triplet reservoir'. A group of authors proved experimentally and theoretically [52] that, in this way, the efficiency of TADF drops, which indicates that HFC is weak and that other nonradiative deactivation processes take place in **XI** (when the [3]CT state is the lowest energy state).
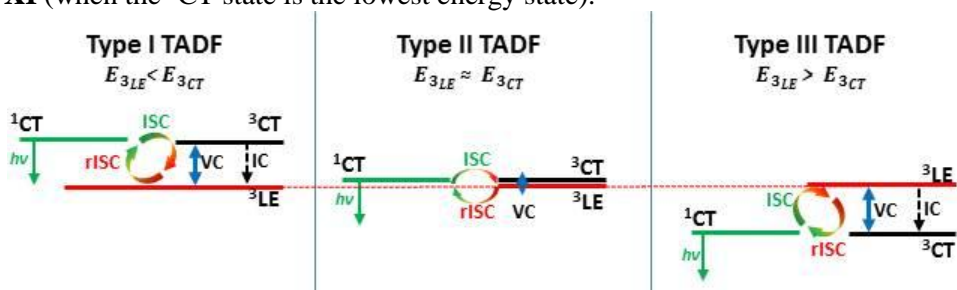
Figure 2.2.12. Three types of polarity-rigidity-dictated TADF mechanisms

These three polarity-rigidity-dependent TADF mechanisms were confirmed by *dos Santos* et al. [48,53]. The TADF behavior of compounds **XII** and **XIII** (**Fig. 2.2.13.**) was investigated in solvents and solid hosts of different polarity. Both compounds were found to behave similarly to **XI**, and clear influence of the host polarity on the TADF efficiency was observed. Moreover, by fabricating OLEDs based on **XII** and **XIII**, the authors showed how important it is to design the hosts and guests in parallel in order to get the appropriate polarity of the host and thus minimize ΔE_{ST} while maximizing the rISC. It is noteworthy that *dos Santos* et al. [53] revealed that the [1]CT state undergoes dynamic relaxation in time, and it can mislead other scientists when calculating ΔE_{ST}. The energy of the [1]CT state should be taken at the earliest possible time after the excitation.

Figure 2.2.13. Chemical structures of D–A–D compounds **XII** and **XIII**

Another family of compounds (**XIV–XX**, **Fig. 2.2.14**) was investigated by Ward et al. [47]. All the compounds use the same D (phenothiazine) and A (dibenzo[b,d]thiophene 5,5-dioxide) moieties and are in princip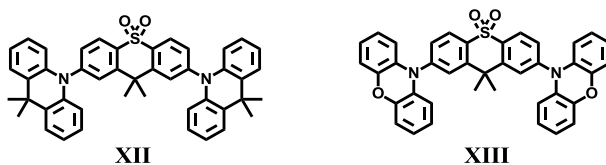le similar to their parent compound **XI**. However, steric hindrance was introduced to the D moiety, and scholars investigated how the restriction of rotations around the D–A bond affects the TADF behavior within the family. Apparently, the introduction of steric hindrance suppressed the vibrations around the D–A bond, which was followed by the quenching of TADF. The bulkier hindrance was introduced, the more TADF was quenched. The impact of steric hindrance followed: methyl<*i*-Pr<*t*-Bu. However, steric hindrance was found not only to quench TADF but also to simultaneously switch on room temperature phosphorescence (RTP) in these series of compounds. This discovery opened up a new strategy in the design of RTP emitters. Moreover, the work of Ward et al. [47] raised global interest among scientists with the objective to explain what is the factor controlling TADF and RTP since both processes can be enabled in the compounds bearing the same chromophores.

	R	R1
XIV	Me	H
XV	*i*-Pr	H
XVI	*t*-Bu	H
XVII	Me	Me

	R
XVIII	H
XIX	Me
XX	*i*-Pr
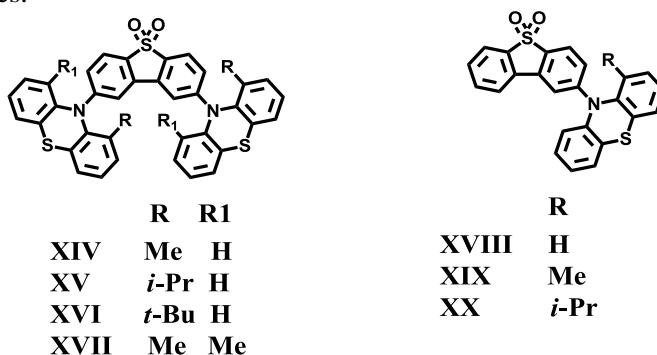
Figure 2.2.14. Chemical structures of sterically restricted compounds **XIV–XX**

To summarize, the requirements for TADF emitters are:
- Electron donor and acceptor moieties are perpendicular to each other; this leads to weak electronic coupling between them (strong CT character);
- A rigid molecular structure, a fixed D–A angle;
- With the molecular structure being rigid, some certain molecular vibrations (around the D–A bond) must not be suppressed;
- High PL QY in the solid state;
- The compound has to show the CT character even in nonpolar media; however, CT should not be too much polarity-sensitive;
- Due to the sensitivity of TADF to the polarity of the environment, a host material should be designed along with the emitter (guest).

2.3. Materials for Emitting Layers of OLEDs

Carbazole   **9,9-Dimethyl-9,10-dihydroacridine**   **1,3,5-triazine**   **Nitrile**

Figure 2.3.1. Chemical structures of chromophores mostly used as hosts and emitters in OLEDs

Both TADF and phosphorescence include triplet exciton harvesting. As it was mentioned in Chapter 2.2.2., the host should possess bipolar and balanced charge mobility, whereas the triplet energy of the host should be higher than that of the guest. In the meantime, TADF emitters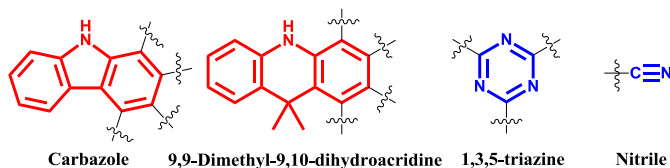 feature their own set of criteria; however, the bipolar molecular structure was proved to be the leading way in the design of both host and guest materials for PhOLEDs and TADF OLEDs [36,61–78]. Among bipolar compounds used in the emissive layers of OLEDs, four chromophores proved to be the most successful (**Fig. 2.3.1.**): electron donors carbazole [25,28,41,62,72,77,79–89], acridine [30,38,53,62,72,77,79,87,88,90–96], and acceptors triazine [34,62,72,74,79,83,84,88–90,96–102] and nitrile (cyano group) [25,29,31,77,88,100,103–108]. As it can be perceived from the repeating numbers of references after each of these chromophores, each donor chromophore is often found in the combination with each acceptor. Thus we will dedicate this chapter only to the observation of the results of the D–A compounds comprising a combination of these chromophores. Moreover, there are numerous reports of new emitters hosts for OLED applications; however, in our thesis, we will report only those compounds which were applied in devices. Since the device structure can vary from one up to >10 layers, and the efficiency of an OLED directly depends on the energetic confinement of the layers, their thickness, etc., we find it pointless to make a comparison of OLED characteristics; instead, we will focus on how the differences among similar structures impact the energetic levels as well as the photophysical and thermal properties of the emitting layer compounds.

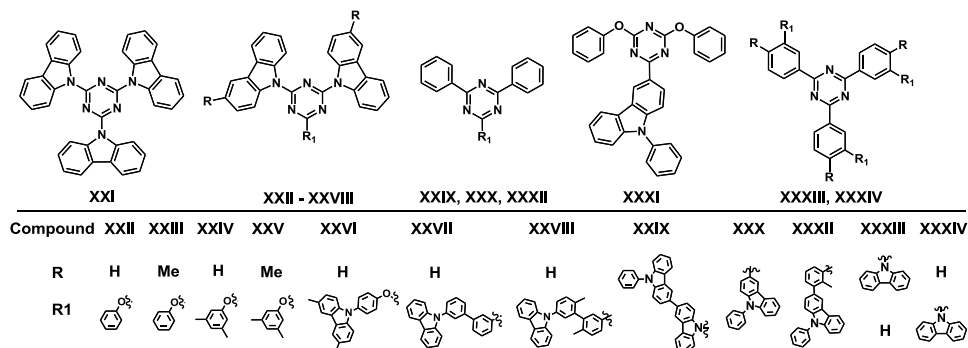### 2.3.1. Host Materials. Triazine-Carbazole Hybrids

Figure 2.3.2. Triazine-carbazole host materials

To start with, bipolar triazine-carbazole derivatives have been exploited for many years in the field of PhOLEDs. Significant application of such hybrid materials in PhOLEDs has been reported by Adachi and peers [68,109,110], as well as by Strohriegl and peeers [66,76,111]. A few structures of these hybrid materials are presented in **Fig. 2.3.2**.

Compounds **XXI–XXXIV** were successfully used in green and blue PhOLEDs as hosts. However, we shall focus on the ways the differences in the molecular structure affect the photophysical properties and energetic levels as well as the thermal properties of these compounds. A summary of the latter is presented in **Table 2.3.1**. Compound **XXI** [110] contains three carbazoles directly connected to triazine via C–N bonds, whereas among compounds **XXII–XXVIII**, one carbazole is changed by various groups, mostly via an ether bridge (**XXII–XXVI** [66,111]). The substitution of one carbazole (**XXI**) to the phenyl ether moiety (**XXII**) results in the increased energy of both S_1 and T_1 states of ca. 0.1 eV. While S_1 and T_1 energies of **XXI** are 3.16 eV and 2.81 eV, respectively, those of **XXII** were found to be 3.33 eV and 2.95 eV, respectively. However, all compounds **XXI–XXV** showed quite high ionization potential (IP) values (6.00–6.14 eV) compared to those of the derivatives with the increased electron donating strength (**XXVI–XXIX**, 5.48–5.60 eV). It is remarkable that when only one C–N bonded carbazole moiety is connected to triazine (as it is in **XXIX** and **XXX**), an increase of electron affinity is observed. Bipolar charge mobility was detected across the entire series. The thermal characteristics mainly depend on the molecular weight of the material; thus compounds with a higher molecular weight demonstrated higher thermal stability as well as glass transition temperatures compared to those of compounds of a smaller molecular weight. For example, compounds **XXII** and **XXXII** of a similar molecular weight showed almost identical thermal characteristics. Their glass transition and thermal decomposition temperatures differ only by 1 °C. The increasing molecular weight results in higher thermal stability. An example can be sourced by comparing **XXX** of a lower molecular weight to **XXIX** which is one carbazole 'heavier'.

The glass transitions are 86 °C and 134 °C, whereas the thermal decompositions are 373 °C and 425 °C for **XXX** and **XXIX**, respectively. Compound **XXIX**, however, deserves some further attention because it was shown by Serevičius et al. [112] that this compound is denoted by oxygen-sensitive PL behavior. The authors investigated the behavior of this PL in solutions as well as in the solid state and tested **XXIX** as an emitter in OLED. The obtained 6% value of EQE manifested the input of the up-converted triplet excitons to the singlets in **XXIX**.

Meta-linking together with the introduction of the steric hindrance strategy was employed as well with the objection to reduce the coupling between D and A moieties in compounds **XXVII** and **XXVIII** [76]. The breakage of conjugation by the means of two *ortho*-methyl units within the biphenyl moiety in **XXVIII** resulted in a 0.1 eV higher E_T value (2.81 eV) compared to the analogue **XXVII** without additional steric twisting (2.71 eV). Interestingly, the peak of fluorescence of **XXVIII** was found to be located at 440 nm, which equals the

same energy as its T_1 (2.81 eV). However, the fluorescence spectrum was recorded in the neat film of **XXVIII**, while for phosphorescence measurements, a solid solution of 2 wt.% of **XXVIII** dispersed in PMMA was used.
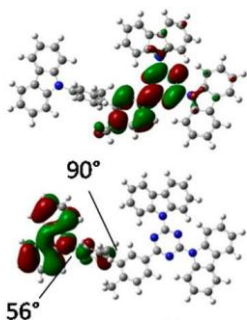

Figure 2.3.3. HOMO and LUMO orbital distribution in **XXVIII**

It is likely that **XXVIII** is a less polar host than PMMA (PMMA contains the polar keto group), thus the S_1 level of **XXVIII** in PMMA is expected to be shifted in comparison with that obtained in the neat film. In source [76], the authors performed basic theoretical calculations and consequently revealed that the S_{0-1} excitation is dominated by the HOMO→LUMO transition and that HOMO is situated on the phenylcarbazole moiety whereas LUMO is situated on triazine and another adjacent phenylene unit (**Fig. 2.3.3.**). The authors assumed that fluorescence is dictated by this S_{0-1} CT type transition, which could be possible after certain planarization of the molecule in the relaxed excited state with a potentially improved orbital overlap. It is worth highlighting that during the phosphorescence measurement, the authors used 1μs delay after the excitation. This is enough for prompt fluorescence to fully decay; however, the μs time range is the range where, if present, the delayed fluorescence takes place. To the date of writing the present thesis, publication [76] has been quoted 36 times; however, only in the framework of *a host material* for PhOLEDs and TADF OLEDs. We opine that this material could possess TADF as well.

Table 2.3.1. Main characteristics of hosts **XXI**, **XXII**, **XXVI–XXXIV**

Compound	λ_{FL}, nm[a]	E_T, eV[b]	IP / EA, eV[c]	T_g / $T_{dec-5\%}$, °C[d]	μ[e]
XXI	392	2.81	6.00/2.60	n.a.*	Bipolar
XXII	372	2.95	6.14/1.92	80/356	Bipolar
XXVI	353	2.91	5.48/2.20	148/453	Bipolar
XXVII	431	2.70	5.60/2.36	134/445	Bipolar
XXVIII	440	2.81	5.58/2.28	154/475	Bipolar
XXIX	526	2.67	5.49/2.77	134/425	Bipolar
XXX	415	2.79	6.04/2.70	109/375	Bipolar
XXXI	416	2.78	5.69/2.76	86/373	Bipolar
XXXII	401	2.86	5.70/2.64	79/357	Bipolar
XXXIII	n.a.	2.71	6.15/3.00	n.a.	Bipolar
XXXIV	467	2.52[f]	6.18/3.23	162/n.a.	Bipolar

[a]Peak of fluorescence; [b]Triplet energy value; [c]Ionization potential and electron affinity; [d]Glass transition and thermal destruction temperature; [e]Charge mobility; [f]Value of triplet energy was taken at an extremely long delay (>10ms); thus it is expected that this value is not reliable; *Not available.

The appearance of an aromatic ether within the bipolar structure and the subsequent increase of both E_S and E_T in triazine-carbazole hybrid materials was confirmed by Liu et al. [113] who synthesized and applied compounds **XXX** and **XXXI** as hosts for blue PhOLEDs. The phenyl ether moiety in **XXXI** if compared with a simple phenylene containing unit in **XXX** was found to decrease the thermal stability of **XXXI** by ca. 20 °C; however, both compounds showed glass-transition temperatures within the practical application range (>80 °C). The enhanced electron donating properties of the oxygen atom in **XXXI** were found to reduce the values of IP by ca. 0.3 eV compared to those of **XXX** (**Table 2.3.1**). Similarly to compound **XXX**, Kim et al. [79] synthesized *meta*-phenylene spacer containing compound **XXXII**; the spacer just included one extra methyl steric hindrance. The more separated donor and acceptor in **XXXII** (in comparison to **XXX**) were found to be responsible for the slightly increased energies of E_S and E_T in **XXXII**. However, IP was found to decrease in **XXXII** (5.70 eV).

Dendrimers and star-shaped compounds possess enhanced light harvesting properties; such structures are frequently used in nonlinear optics applications [114–117], etc. The star-shaped molecular architecture was applied in order to realize the host materials as well [99,118]. Compounds **XXXIII** and **XXXIV** represent an example of triazine substituted with three carbazoles via *para*- and *meta*-phenylene spacers. Compound **XXXIV** was successfully applied as a host for green, red and even blue PhOLEDs despite its relatively low E_T (2.52 eV). We should note that the authors estimated E_T for **XXXIV** at an extremely long delay time (>10 ms). Despite our general knowledge that in case of such long delays only T_{1-0} emission can be observed [59], we still believe that this compound should possess higher E_T. Even a comparison of E_T with its *para*-analogue **XXXIII** causes some doubts whether the *meta*-isomer can possess a lower E_T since the E_T of **XXXIII** was found to equal 2.71 eV. It was recently shown by Dias et al. [46] that in electronically weakly coupled D–A compounds, all the three triplet states (^3LE_D, ^3LE_A, ^3CT) are in the competition and the overall triplet emission spectrum is evolving with time. Therefore, any estimation of E_T should be considered with caution. Moreover, in Chapter 4.2, we present a triazine-carbazole hybrid material which, in principle, features a similar structure to that of **XXXIV**, and our measurements show that the E_T of such a compound should be of 2.77 eV.

2.3.2.   Host Materials. Nitrile-Carbazole Hybrids

The nitrile (CN) group was identified as a relatively strong electron acceptor compared to other linear analogues (i.e. trifluoromethyl-, acetyl-, etc.), and it is successfully used in the design of both host and emitter materials for OLEDs. Nitrile is a linear rigid moiety which is easy to substitute with any leaving group (halogen) within the molecule. Since almost every position of carbazole can be easily modified, a combination of these two units is found in many scientific publications. **Fig. 2.3.4**. presents a few structures of carbazole-nitrile hosts for blue PhOLEDs and TADF OLEDs.
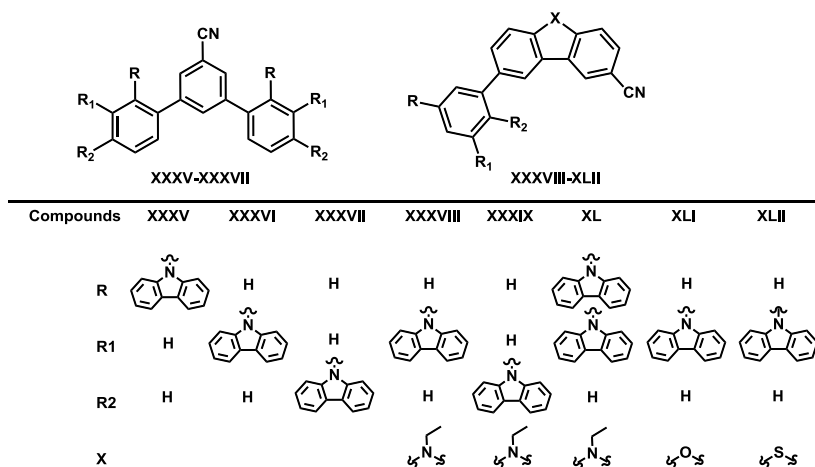
Figure 2.3.4. Carbazole-nitrile host materials

Li et al. [119] reported three isomeric carbazole-cyano-terphenylene derivatives **XXXV–XXXVII**. *Ortho-* and *meta*-derivatives demonstrated high E_T (3.01 and 2.81 eV, respectively), while the E_T of the *para*-isomer was found to be slightly lower (2.77 eV). It was discovered that the donor substitution pattern impacted IP: directly connected D and A in **XXXVII** resulted in the lowest values of IP (5.59 eV), whereas **XXXV** bearing the most twisted molecular skeleton showed the highest values of IP (5.74 eV). *Ortho*-conjugation in **XXXV** was also identified to be responsible for the lowest T_g among the series (94 °C). All the compounds were tested in single-carrier devices, and bipolar mobility was detected in all the samples. All the three isomers were successfully applied as hosts in blue PhOLEDs (emitter FIrpic) and TADF OLEDs (emitter 2CzPN). It is noteworthy that the best device performance was registered when a *meta*-isomer (**XXXVI**) was used as a host while *para*-host containing devices (**XXXV**) showed the lowest turn-on voltage.

Another five carbazole-nitrile hosts (**XXXVIII–XLII**) were synthesized and investigated by Deng et al. [120]. The chemical structures of these compounds are presented in **Fig. 2.3.4**. Within this family, the nitrile group is attached to carbazole, or dibenzothiophene, or dibenzofuran in order to enhance the electron withdrawing capacity of these chromophores. Such modified chromophores were linked with carbazole via *meta*- or *ortho*-phenylene junctions. It is of interest that the use of dibenzofuran resulted in the highest energy emitting material: **XLI** emitted fluorescence at 363 nm, whereas its E_T was found to be as high as 2.89 eV. The ionization potentials were found to be of the same energy among all the family, yet the use of *ortho*-phenylene connection in **XXXIX** resulted in the highest EA (2.37 eV) among the series. In the meantime, both dibenzothiophene and dibenzofuran were identified as weaker electron donors than carbazole; **XLI** and **XLII** showed the lowest values of EA among all the series (2.19 eV and 2.20 eV, respectively). It should also be mentioned that compound **XXXVIII** of the smallest molecular weight demonstrated the poorest thermal characteristics. The glass transition temperature was not detected, and the thermal decomposition

temperature as low as 186 °C was observed. However, the remaining compounds of the series demonstrated decent thermal behavior (**Table 2.3.2.**).

Table 2.3.2. Main characteristics of hosts **XXXV–XLII**

Compound	λ_{FL}, nm^a	E_T, eV^b	IP / EA, eV^c	$T_g / T_{dec\text{-}5\%}$, $°C^d$	μ^e
XXXV	403	3.01	5.74/2.16	94/420	Bipolar
XXXVI	403	2.81	5.62/2.14	121/350	Bipolar
XXXVII	406	2.77	5.59/2.16	140/440	Bipolar
XXXVIII	390	2.82	5.62/2.20	n.a./186	Bipolar
XXXIX	384	2.82	5.62/2.37	104/320	Bipolar
XL	402	2.78	5.66/2.23	167/437	Bipolar
XLI	363	2.89	5.63/2.19	98/334	Bipolar
XLII	404	2.78	5.63/2.20	111/330	Bipolar

[a]Peak of fluorescence; [b]Triplet energy value; [c]Ionization potential and electron affinity; [d]Glass transition and thermal destruction temperature; [e]Charge mobility; *Not available.

2.3.3.   TADF Emitters

Carbazole is a universal chromophore since it is found not only in donor-based host materials for OLEDs (CBP, mCP, TCTA, etc.) but also within the structures of TADF emitters as well. Among them, the first family of all color TADF emitters to be applied in OLEDs exceeding the theoretical limit of 5% EQE was the family of carbazole-phthalonitrile (dicyanobenzene) derivatives, as reported by Uoyama et al. [25]. The structures of these compounds are presented in **Fig. 2.3.5**.
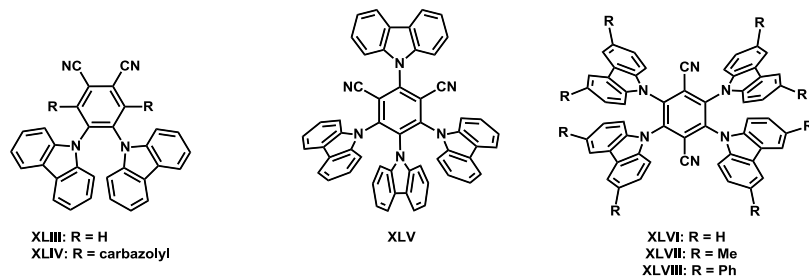

XLIII: R = H
XLIV: R = carbazolyl

XLV

XLVI: R = H
XLVII: R = Me
XLVIII: R = Ph

Figure 2.3.5. Structures of carbazole-phthalonitrile derivatives **XLIII–XLVIII**

Compounds **XLIII–XLVIII** differ by the number of peripheral carbazolyl groups and the donating strength of these carbazolyl groups. By connecting different ratios of peripheral groups of different donating strength to *ortho-*, *meta-* and *para-*dicyanobenzene cores, the authors managed to synthesize compounds emitting light in the range from the sky-blue to the orange color. The use of only two donors within the molecule resulted in the weakest overall donating strength, which susequently led to blue emission in **XLIII**. On the other hand, the increase of the electron donating strength from carbazole <3,6-dimethylcarbazole <3,6-diphenylcarbazole resulted in the consequent red-shift of emission among **XLVI**,

XLVII and **XLVIII**, respectively. The isomeric differences among the cores also influenced the overall electronic communication among isomers **XLIV**, **XLV** and **XLVI**. The emission of *meta*-dicyanobenzene core bearing **XLV** was found to be the most blue-shifted, whereas that of *para*-dicyanobenzene analogue **XLVI** was found to be the most red-shifted.

Table 2.3.3. PL characteristics of dilute toluene solutions of **XLIII–XLVIII** under argon atmosphere

Compound	λ_{SI}, nm[a]	PL QY, %[b]	Lifetime[c]	
			τ_{PF}, ns	τ_{DF}, μs
XLIII	473	26.3	28.5	166.0
XLIV	525	74.4	14.3	13.9
XLV	507	93.8	17.8	5.1
XLVI	535	71.6	8.8	1.9
XLVII	561	47.4	9.2	1.5
XLVIII	577	46.5	9.0	1.1

[a]Steady-state photoluminescence peak values; [b]Photoluminescence quantum yield; [c]Prompt (PF) and delayed fluorescence (DF) lifetimes.

Photoluminescence quantum yield (PL QY) and lifetime (τ) are among the most important parameters in characterizing the emitters since these parameters determine the efficiency of emission. As it can be derived from **Table 2.3.3.**, the use of 4 carbazoles appeared to be a successful strategy when seeking to achieve high values of PL QY since all the compounds with 4 carbazoles demonstrated 2 to 3 times higher values of PL QY compared to **XLIII** bearing 2 carbazoles. The isomeric core differences also impacted the PL efficiency: *meta*-dicyanobenzene core bearing **XLV** was found to possess the highest PL QY of 93.8%; it it was followed by an *ortho*-analogue (**XLIV**, 74.4%), whereas the poorest PL QY was shown by a *para*-isomer (**XLVI**, 71.6%). All the compounds showed broad and structureless emission bands in toluene, which indicates the formation of CT states. In the case of TADF-possessing compounds, the lifetime of the singlet state (10^1 ns) is around 1 order of magnitude longer than that of typical fluorescent emitters (10^0 ns). Since this ^{1}CT state is repopulated by excitons via rISC, its lifetime increases. This was observed for argon saturated toluene solutions of **XLIII–XLVIII**. Prompt fluorescence lifetimes fit in the range of 9–28 ns. What concerns the lifetime of delayed fluorescence, the most notable difference is between **XLIII** and the rest of the series. The τ_{DF} of **XLIII** was found to equal 166 μs, whereas all the other compounds bearing 4 carbazoles showed values of τ_{DF} falling in the range 1–14 μs. Moreover, the isomeric influence of the core was estimated as well: the values of τ_{DF} are decreasing in the direction of *ortho-* >*meta-* >*para*-dicyanobenzene. The relevant τ_{DF} values are: 13.9 μs, 5.1 μs and 1.9 μs for **XLIV**, **XLV**, **XLVI**, respectively. We should note that an excessively long DF lifetime (>100 μs) can accelerate other excited state

processes, such as triplet-triplet annihilation, internal conversion, etc. thus decreasing the TADF efficiency. The authors tested compounds **XLIII**, **XLV** and **XLVIII** as emitters in OLEDs. The fabricated OLEDs emitted in sky-blue (**XLIII**), green (**XLV**) and orange (**XLVIII**) colors with EQE values of 8.0%, 19.3%, and 11.2%, respectively. Such high EQEs demonstrated that purely organic emitters are now ready to challenge the rare-earth-metal containing ones.
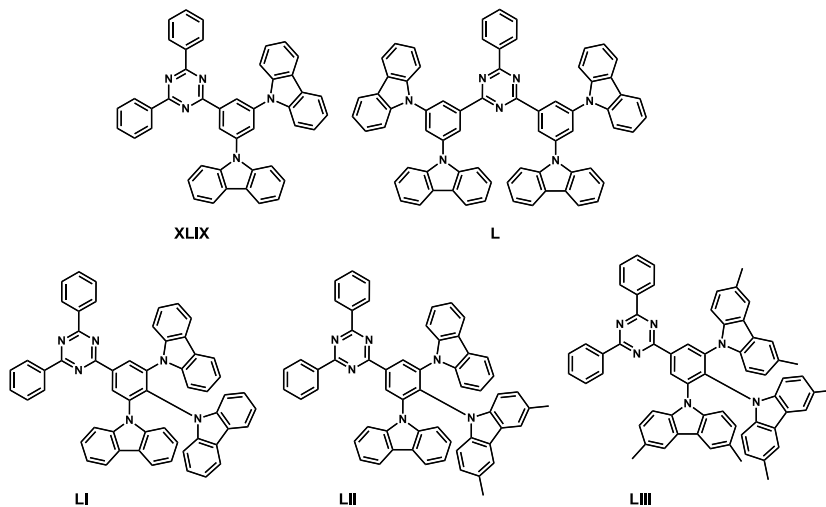

Figure 2.3.6. Chemical structures of compounds **XLIX–LIII**

Continuous research of certain types of molecular structures leads to improved understanding of the ways how structural modifications impact the resulting properties. This was shown by Kim et al. [121] in terms of two triazine-carbazole TADF emitters **XLIX** and **L** (**Fig. 2.3.6.**). *Meta*-linkage was used to connect carbazoles to the triazine core in order to avoid the red-shift in the emission color. It was achieved since 2 carbazoles bearing **XLIX** emitted at 420 nm, while 4 carbazoles possessing **L** demonstrated only a 10 nm bathochromic shift compared to **XLIX**. However, a higher quantity of donors led to more efficient emission: the PL QY of **L** was found to be 66% in the toluene solution, while that of **XLIX** was 23% lower. In the meantime, *meta*-linkage proved to suppress both E_S and E_T, since the values of ΔE_{ST} for **XLIX** and **L** differ only by ca. 0.02 eV. Both compounds were tested as emitters in OLEDs. Despite EQEs being comparable (17.8% and 18.9% for **XLIX** and **L**, respectively), the stability of devices appeared to be completely different. While OLED containing **L** as the emitter demonstrated the LT_{80} value of 52 h (the time required for luminescence to drop to 80% of its initial value); the device containing **XLIX** showed only a lifetime of 5 h. A lifetime of 52 h was estimated to be 3 times longer than that of analogue blue PhOLED. Such astonishing differences in the device lifetime were explained by the differences in the molecular structures: a relatively planar molecular structure enhances conjugation between chromophores thus enhancing the D–A bond stability; carbazole and triazine polarons are stable, and they recombine within the emitter; also, high glass transition temperatures of emitters

(160 °C and 218 °C for **XLIX** and **L**, respectively) are observed. However, a device containing **XLIX** demonstrated 1 order of magnitude shorter lifetime. The authors explained this by a combination of two factors: the higher energy of **XLIX** emissive state enhances the degradation, and PL QY of **XLIX** was found to be lower (43%) in comparison to that of **L** (66%), which indicates more pronounced nonradiative pathways in **XLIX**.

As the next step, the authors decided to check their assumption that the extra carbazole moiety increases PL QY and also reduces the ΔE_{ST} in addition to synthesizing three new derivatives which are similar in structure to **XLIX** [122]. The structures of these compounds (**LI**, **LII** and **LIII**) are presented in **Fig. 2.3.6**. Indeed, the incorporation of an extra carbazole within the parent structure resulted in the enhancement of PL QY values reaching unity. It should be observed that solid state PL QY is equally high, which indicates negligible concentration quenching for multi-carbazole-based triazine derivatives **LI–LIII**. Another fundamental difference among the structures is that the extra carbazole acts as steric hindrance as well; therefore, larger localization of HOMO and LUMO orbitals is expected, which leads to a lower exchange energy and the subsequent lower values of ΔE_{ST}. As the authors claim, the addition of an extra carbazole results in ca. 0.09 eV smaller ΔE_{ST}. An example of this phenomenon is compounds **XLIX** and **LI** which showed ΔE_{ST} values of 0.25 eV and 0.16 eV, respectively. **Table 2.3.4.** summarizes the most important parameters of TADF emitters **XLIX–LIII**. All the compounds were tested as emitters in OLEDs, and high EQEs were obtained: 25.0%, 21.3% and 25.5% for **LI**, **LII** and **LIII**, respectively. Since **LI** contains unsubstituted carbazoles, the device was found to emit in the sky-blue region whereas the other two devices were green-emitting. The obtained >20% values of EQEs confirmed the overall benefits provided by extra carbazole units within the molecular structures of blue and green TADF emitters.

Table 2.3.4. PL characteristics of dilute toluene solutions of **XLIX–LIII** under argon atmosphere

Compound	λ_{SI}, nm[a]	PL QY, %[b]	ΔE_{ST}, eV[c]	τ_{DF}, µs[d]
XLIX	420	43	0.25	3.1
L	430	66	0.27	2.8
LI	418	100 (100)	0.16	13.5
LII	423	84 (98)	0.20	9.7
LIII	433	99 (100)	0.07	13.3

[a]Steady-state photoluminescence peak values; [b]Photoluminescence quantum yield in toluene solutions. Values in parentheses: 30% of emitter doped into DPEPO film; [c]Singlet-triplet energy splitting; [d]Delayed fluorescence (DF) lifetime.
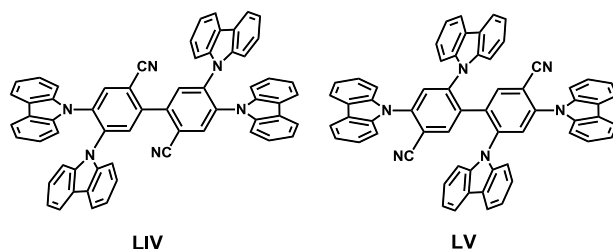
LIV   LV

Figure 2.3.7. Chemical structures of compounds **LIV** and **LV**

Table 2.3.5. PL characteristics of dilute toluene solutions of **LIV** and **LV** under argon atmosphere

Compound	λ_{Sl}, nm[a]	PL QY, %[b]	ΔE_{ST}, eV[c]	τ_{DF}, µs[d]	FWHM, nm[e]
LIV	458	45 (46)	0.27	24.3	71
LV	453	20 (76)	0.27	48.2	55

[a]Steady-state photoluminescence peak values; [b]Photoluminescence quantum yield in air-saturated toluene solutions. Values in parentheses: oxygen-free toluene solutions; [c]Singlet-triplet energy splitting; [d]Delayed fluorescence (DF) lifetime; [e]Photoluminescence full width at half-maximum.

Another interesting molecular design strategy was demonstrated by Cho et al. [123] who synthesized two isomeric derivatives of carbazole and benzonitrile by employing the so-called 'donor interlocked' strategy. The structures of these compounds (**LIV** and **LV**) are presented in **Fig. 2.3.7**. These isomeric compounds are derivatives of a well-known host material CBP; however, the authors incorporated two additional carbazoles and two nitrile units into the central biphenyl. Such highly twisted multichromophore structures were expected to possess a high triplet energy as well as a small ΔE_{ST}. Theoretical calculations predicted different twistings of the central biphenyl unit as well as side carbazoles connected to the biphenyl core. Apparently, the use of two rigid linear CN groups in 2,2'-positions of the biphenyl core in **LIV** led to 60° twisting of the biphenyl core, whereas the lower twisting degree of the core was achieved in **LV** (47°) where two *ortho*-carbazoles were employed. On the other hand, when these side carbazoles were connected to the biphenyl via 3,3' positions (**LIV**), there was more rotational freedom. Thus the dihedral angle between phenylene and the adjacent carbazole was found to be 60°. This rotational freedom was completely suppressed in **LV** since these *ortho*-carbazoles were found to be perpendicular to the adjacent phenylenes. The most important characteristics of compounds **LIV** and **LV** are presented in **Table 2.3.5**.

Both compounds were found to possess deep blue emission and relatively small ΔE_{ST}; however, only **LV** showed oxygen-sensitive PL behavior. Independently from the measurement conditions (air saturated or oxygen-free toluene solutions), the PL QY of **LIV** was found to remain constant, while that of **LV** showed intense increase upon elimination of oxygen (20→76%). Most surprisingly, the PL spectrum of **LV** was found to be as narrow as that of a conventional fluorescent emitter. The full width at half maximum (FWHM) of EL was found to be even narrower (48 nm) compared to that of PL (55 nm). The

authors attributed this phenomenon to 'donors interlock', which increases the rotational barrier within the biphenyl unit resulting in a narrow emission spectrum. This is the narrowest up-to-date known emission spectrum of a TADF compound.
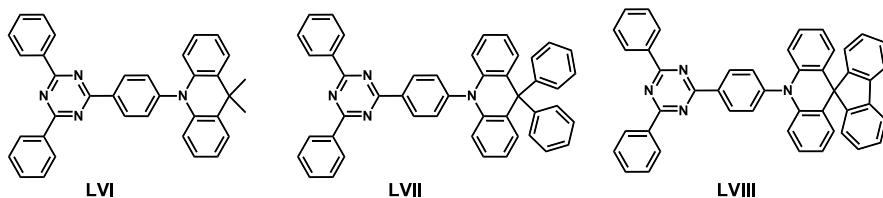

Figure 2.3.8. Chemical structures of triazine-acridine blue TADF emitters

While carbazole-based compounds demonstrate their universal potential as hosts and guests, probably the most attractive donor in the construction of blue and green TADF emitters is 2,7-di-tert-butyl-9,9-dimethyl-9,10-dihydroacridine. Compounds **LVI–LVIII** (**Fig. 2.3.8.**) were synthesized in the laboratories of Wong and his team [96,124]. 2,4,6-triphenyl-1,3,5-triazine was connected via *para*-linkage to different derivatives of acridine. Methyls (**LVI**), phenyls (**LVII**) or biphenyl (**LVIII**) were introduced in order to modify the C–9 positions of the carbon atom in acridine in order to achieve a different electron donating strength. At first, compound **LVI** was reported [124]. Dilute **LVI** solution in toluene demonstrated desirable PL characteristics: emitting in green (495 nm), possessing ΔE_{ST} of 0.046 eV, PL QY values reaching 90%, and a relatively short DF lifetime (1.9 μs). Unexpectedly, neat films of **LVI** demonstrated superb characteristics as well: emitting at 500 nm (we should note that very little concentration caused the red-shift of emission), ΔE_{ST} as low as 0.05 eV, and PL QY of 83%, while τ_{DF} maintained the same order of magnitude (3.6 μs). Due to these astonishing findings, the authors manufactured OLEDs with **LVI** doped in mCPCN (8%) and with neat **LVI**. Both devices showed bluish-greenish and green EL spectra with EQEs reaching 26% and 20%, respectively. These results manifested the substantial design strategy of self-hosting emitters. Such compounds do not require hosts; therefore, the device fabrication process is relatively simplified.

Inspired by the characteristics of **LVI** and the promising device performance, Lin et al. [96] extended the parent **LVI** compound by modifying acridine via C–9 position by the means of the substitution of methyls to phenyls (**LVII**) and biphenyl (**LVIII**). Even though theoretical calculations predicted that the acridine moiety is flat, single crystal X-Ray diffraction analysis revealed crucial differences among **LVI–LVIII**. The substitution of C–9 position yielded the flat acridinyl part only when rigid biphenyl was used (**LVIII**). However, the acridinyl part was found to be almost perpendicularly twisted to the triphenyltriazine plane, which ensured a high degree of frontier orbitals separation. The highest rigidity of **LVIII** was reflected by the highest glass transition temperature among the three compounds. The glass transition of **LVIII** reached 155 °C, while that of **LVII** was 20 °C lower, and **LVI** manifested the temperature as low as 90 °C. Acridine modification influenced the properties of

emission as well: while the emission of two methyls bearing **LVI** was found to be located at 495 nm, flexible phenyls in **LVII** pushed the PL spectra to the blue side (478 nm). Moreover, the ΔE_{ST} of **LVII** was found to be the largest among the series (0.133 eV). The rigidity of the molecule enhances its thermal stability and also supresses nonradiative decay pathways from the excited state as it can be observed in the data derived from PL QY measurements. **LVI** bearing two methyls emits 90% of photons, whereas the most distorted molecular structure possessing **LVII** emits only 82%, while the most rigid structure **LVIII** produces the unity value of PL QY. It is worth noting that the authors performed PL QY measurements for **LVIII** with varying doping concentrations in the mCPCN host and found that even a neat film of **LVIII** possesses >90% PL QY. Such a small decrease in PL QY indicates the presence of the aggregation induced emission (AIE) phenomenon in **LVIII**. All the compounds showed relatively short τ_{DF} (2–3 μs), which is beneficial for device application. Moreover, the scholars measured the dipole moment orientation within the emitting layers and found out that the majority of emitting dipoles are horizontally oriented in these compounds. Special attention should be paid to compound **LVIII** which is the first example of TADF emitter showing 100% PL QY and >80% of horizontal emitting dipole orientation. This horizontal (in-plane orientation within the layer) emitting dipole orientation contributes mostly to the EQE in OLEDs, thus it is expected that an OLED fabricated with this type of material should be highly efficient. Indeed, the sky-blue emitting OLED based on **LVIII** (12% doped into mCPCN) showed a record breaking value (36.7%) of EQE. This is the most efficient TADF OLED to date of this thesis [125]. The most important characteristics of compounds **LVI**–**LVIII** are presented in **Table 2.3.6**.

Table 2.3.6. The main characteristics of **LVI–LVIII**

Compound	λ_{SI}, nm[a]	PL QY, %[b]	ΔE_{ST}, eV[c]	τ_{DF}, μs[d]	$\Theta_{//}$, %[e]	T_G, °C[f]
LVI	495	90	0.062	1.9	72	90
LVII	478	82	0.133	2.9	78	136
LVIII	480	100	0.072	2.1	83	155

[a]Steady-state photoluminescence peak values; [b]Photoluminescence quantum yield in air-saturated toluene solutions. Values in parentheses: oxygen-free toluene solutions; [c]Singlet-triplet energy splitting; [d]Delayed fluorescence (DF) lifetime; [e]Horizontal dipole ratio. Measured in doped mCPCN films (12 wt.%); [f]Glass transition temperature.

2.4. Summary of Literature Review

To sum up, in this literature review we analyzed the phenomenon of light and the working principles of OLEDs. We also reviewed materials used in modern electroluminescent devices. Currently, there are two leading approaches of efficient conversion of energy into light using organic materials: phosphorescence and thermally activated delayed fluorescence. We overviewed the mechanisms behind these phenomena and identified the requirements for host and guest materials. Moreover, we conducted literature analysis and presented some of the recent discoveries and trends in the molecular design of materials for

OLED applications. The application of high triplet energy bipolar hosts in PhOLEDs provides an opportunity to significantly increase the EQE and decrease the turn-on voltage, etc., due to the efficient triplet exciton and IP/EA confinement, bipolar charge transport, aggregation-caused quenching prevention, and the superior thermal and electrochemical stability of hosts. Bipolar hosts used in phosphorescent OLEDs can be applied to TADF OLEDs as well. However, it is still a major challenge to prepare a high triplet energy multifunctional bipolar host for blue emitters. In turn, the involvement of TADF emitters allows fabrication of noble-metal-free highly efficient devices which function on the grounds of the singlet-triplet upconversion mechanism. Even though several highly efficient TADF OLEDs have already been reported, the challenge of design and preparation of stable blue TADF emitters still persists. Furthermore, new TADF emitters require new suitable host compounds.

There is some degree of confusion among researchers concerning the estimation of certain parameters of TADF materials. Globally, scientists use different techniques/equipment when estimating the same parameters (e.g., ΔE_{ST}, IP/EA values, etc.). It is important to establish the proper structure-property relationship of compounds synthesized and investigated by different scientific groups. However, in our opinion, some problems remain unsolved:

- Even though the fundamental phenomena have already been identified, so far, the exact mechanisms of delayed fluorescence have been studied only for specific molecules (e.g., for compounds synthesized and investigated by Monkman and his team [46–48,53]). Therefore, there is urgent need to design a new type of materials and to investigate them thoroughly in order to check the viability of the currently suggested theories.
- The previously reported compounds may possess great potential. We presented only a few examples of previously reported compounds which were used as hosts for PhOLEDs (**XVIII**, **XXIX**, **XXXIV**), but later it became apparent that these compounds can be used as TADF emitters. In other words, a challenge for materials scientists is not only to focus on the development of novel molecular structures, but also to perform a detailed study of properties in order to reveal the true potential of new emissive layer materials.

We highlighted the remaining issues and challenges in the field of OLED materials. Therefore, in this work, we developed and characterized new bipolar multifunctional materials, especially focusing on the electron donor and acceptor connection pattern, which allowed us to establish the appropriate structure-property relationships among these materials.

3. EXPERIMENTAL PART

3.1. Instrumentation and Methods

3.1.1. Instrumentation

^{1}H and ^{13}C NMR spectra were recorded by using a *Bruker Avance III 400* spectrometer (400 MHz (^{1}H), 100 MHz (^{13}C)) as well as *Bruker DRX-500 P* (500 MHz (^{1}H) and 125 MHz (^{13}C)) spectrometers. Chemical shifts (δ) are reported in ppm referenced to tetramethylsilane or to the internal solvent signal.

IR spectra were recorded in KBr pellets on a *Perkin Elmer Spectrum GX II FT-IR System*. ATR-FT-IR spectra of neat samples were recorded on *Bruker Vertex 70*.

Mass spectra (MS) were obtained on *Waters ZQ 2000*, *Bruker Maxis 4G* and *Shimadzu Biotech Axima* mass spectrometers by using APCI, EI and MALDI-TOF ionization methods, respectively.

Elemental analysis data was obtained on a *EuroEA Elemental Analyser*.

UV/Vis spectra of 10^{-4} M solutions of the compounds were recorded in quartz cells by using a *Perkin Elmer Lambda 35* spectrometer.

PL spectra as well as fluorescence lifetimes (τ) of 10^{-5} M solutions of the compounds were recorded by using a *FLS980 Fluorescence Spectrometer* manufactured by *Edinburgh Instruments*. τ values were calculated by fitting single or multiexponential functions until achieving χ^{2} values of 1 ($\pm$0.1). The phosphorescence spectra were recorded at 77 K for the solid solutions of the materials in the *Zeonex* matrix by using nanosecond gated luminescence measurements (from 400 ps to 1 s) while employing a high energy pulsed *Nd:YAG* laser emitting at 355 nm (EKSPLA). Emission was focused onto a spectrograph and detected on a sensitive gated *iCCD* camera (Stanford Computer Optics) featuring sub-nanosecond resolution. A model liquid nitrogen cryostat (Janis Research) was used for the experiment.

TGA was performed on a *Metter TGA/SDTA851e/LF/1100* apparatus at a heating rate of 20 °C/min under nitrogen atmosphere. Compound decomposition temperatures were determined at the point when the sample loses 5% of its mass ($T_{dec-5\%}$).

DSC measurements were performed on a *DSC Q 100 TA* Instrument at a heating rate of 10 °C/min under nitrogen atmosphere. The melting points (T_{M}) and crystallization temperatures (T_{cr}) were taken from the appropriate endo- and exothermic peaks, respectively. The glass transition temperatures (T_{G}) were estimated from the point when the sample heat capacity changed.

The melting points of the prepared compounds were estimated by using an *Electrothermal Melt-Temp* apparatus (error value $\pm$1 °C).

3.1.2. Methods

3.1.2.1. Sample Preparation

Thin solid films for recording of UV/Vis and PL spectra were prepared by drop-casting 2 mg/ml solutions of the compounds in toluene on pre-cleaned

quartz substrates. Solid solutions of the compounds in *Zeonex* polymer matrices were obtained with the concentration of 1 wt% by mixing the dissolved compounds and polymer in toluene solutions at the appropriate ratio and casting the solutions on quartz substrates in the ambient air. Photoluminescence quantum yields (PL QY) of the solutions and of the solid films were estimated by using the integrated sphere (calibrated with two standards: quinine sulphate in 0.1 H_2SO_4 and rhodamine 6G in ethanol) method [126]. Each experiment was repeated three times, and the error value was estimated to be ±0.02.

3.1.2.2. Electrochemical Measurements

CV measurements were carried out with a glassy carbon working electrode in a three-electrode cell. The measurements were performed by using *Eco Chemie* Company's AUTOLAB potentiostat *PGSTAT20* in a dry solvent solution containing 0.1 M tetrabutylammonium hexafluorophosphate (TBAPF$_6$) as the electrolyte at room temperature under nitrogen atmosphere. The results were collected by using *GPES* (*General Purpose Electrochemical System*) software. The electrochemical cell comprised a platinum wire with a 1 mm diameter of the working area as the working electrode, Ag wire calibrated versus ferrocene/ferrocenium redox couple as a quasi-reference electrode and platinum coil as an auxiliary electrode. Cyclovoltamperometric measurements were conducted at a potential rate of 50 mV/s. IP^{CV} was estimated from the onset oxidation potential by using the relationship $IP_{CV}=|e|(4.8+E_{ox}{}^{onset})$. EA^{CV} was estimated from the onset reduction potential by using the relationship $EA_{CV}=|e|(4.8+E_{red}{}^{onset})$. Each experiment was repeated three times, and the error value was estimated to be ±0.05 eV.

3.1.2.3. Solvatochromic Behavior

Solvatochromic behavior is defined by the Lippert-Mataga equation [169,170]:

$$\Delta\bar{\upsilon} = \frac{2\Delta f}{hca^3}(\mu_E - \mu_G)^2 + const.; \qquad (4)$$

Here, $\Delta\bar{\upsilon}$ stands for the Stokes shift, h is the Planck constant, c is the speed of light, a is the radius of the Onsager cavity, μ_E and μ_G are the dipole moments of the excited and ground states, respectively.

$$\Delta f = \frac{\varepsilon-1}{2\varepsilon+1} - \frac{n^2-1}{2n^2+1}; \qquad (5)$$

Here, Δf stands for the solvent orientation polarizability, ε is the solvent dielectric constant, and n is the solvent refractive index.

3.1.2.4. Charge Mobility Measurements

Charge drift mobility measurements were performed by employing the xerographic time-of-flight (XTOF) [128,129], time-of-flight (TOF) and charge carrier extraction by linearly increasing voltage (CELIV) methods. Samples for the XTOF measurements were prepared as described above [130]. Samples for the measurements were prepared by drop-casting 10 mg/ml solutions of the

compounds in chloroform onto cleaned ITO coated glass substrate. After casting, the cells were heated at 70 °C for 5 minutes. Charge carriers were generated at the layer surface by illumination with pulses of a nitrogen laser (the pulse duration was 1 ns, the wavelength was set at 337 nm). After the photo excitation of the sample with a short light impulse, the rate of the potential discharge in XTOF measurements features a plateau region. The transit time was determined from the kink point in the transient photocurrent curves. Transit time t_{tr} with surface potential U_0 at the moment of illumination indicates the passage of holes through the entire thickness of the films (d) and enables the determination of the hole mobility as $\mu=d^2/U_0 \cdot t_{tr}$. The experimental setup consists of a delay generator *Stanford Research DG 535* and a digital storage oscilloscope *Tektronix TDS754C*.

Samples for the TOF measurements were prepared by spin-coating the solutions of the synthesized compounds in toluene on pre-cleaned ITO coated glass plates [131]. The samples were heated at 70 °C for 20 min in a hot air oven. As the next step, 60 nm of aluminum was deposited by using a mask by thermal evaporation under vacuum below $5 \cdot 10^{-5}$ mbar. Light pulse was used to photo generate the charge carriers by exciting layers of compounds through the ITO. For hole/electron mobility measurements, positive/negative voltage was applied to the ITO electrode. A delay generator *Tektronix AFG3011* was used to generate the square pulse voltage with a pulsed third-harmonic Nd:YAG laser *EKSPLA PL2140* working at a pulse duration of 25 ps and the wavelength of 355 nm. A digital storage oscilloscope *Tektronix DPO4032* was used to record the TOF transients of the layers of the synthesized materials. Transit time t_{tr} for the samples with the charge transporting material was determined by the kink on the curve of the transient in the log-log scale. The charge drift mobility was estimated by using the formula $\mu=d^2/Ut_{tr}$, where d is the layer thickness, and U is the surface potential at the moment of illumination.

For CELIV measurements, sandwich-like structures ITO/Compound/Al were prepared. The thickness of the layers was measured by employing the CELIV technique [132]. The layers of 10 mg/ml THF solution of the compounds were formed by employing the casting method onto clean ITO coated glass substrate within a glove box. Al was evaporated at 15 Å/s at a pressure below $5 \cdot 10^{-5}$ mbar. The experimental setup consisted of a delay generator *Tektronix AFG 3011* and a digital storage oscilloscope *Tektronix DPO 4032*. The mobility measurements were conducted in the dark box by applying a triangular voltage pulse to the samples. The charge carrier mobility was calculated by using formula $\mu=2d^2/At_{max}^2$, where $A=U(t)/t$ is the voltage rise rate, t_{max} is the time for the current to reach its extraction maximum peak, and d is the sample thickness.

3.1.2.5. Computational Details

The theoretical calculations were carried out by using the Gaussian 09 quantum chemical package [133]. Full geometry optimizations of the compounds in their electronic ground state were performed by employing the density functional theory method (DFT) [134] while using the B3LYP functional consisting of the Becke's three-parameter hybrid exchange functional [135]

combined with the Lee-Yang-Parr correlation functional [136] with the 6-31G(d) basis set in vacuum. The spectroscopic properties of the molecules were calculated by the means of time-dependent DFT (TD-DFT) [137–139] calculations employing the 6-31G(d) basis set. In the TD-DFT calculations, various DFT functionals containing different percentages of the exact Hartree-Fock exchange energy (%HF) were employed. These were TPSSh (10%HF) [140], B3LYP (20%HF), PBE1KCIS (22%HF) [141] M06 (27%HF) [142], MPW1B95 (31%HF) [143], BMK (42%HF) [144], M06-2X (56%HF) [142], M06-HF (100%HF) [145] along with the long range corrected functional ωB97X-D [146]. In order to properly analyze the nature of the excited states, natural transition orbital (NTO) [147] analysis was performed with NTOs calculated at the appropriately chosen functional for every tested molecule/6-31G(d) level in the gas phase. Graphical visualizations of the theoretical absorption spectra were accessed with the help of *GaussSum* software [148]. Multiwfn software [149] was used in order to evaluate molecular fragment contribution to the occupied and virtual orbits. The amount of charge (q) transferred from the donor to the acceptor was analyzed by using *Multiwfn* software based on the B3LYP optimized S_0 geometry and calculated by using the following equations:

$$q_+ = e \sum_i |a_i - b_i| \quad a_i - b_i > 0; \tag{6}$$

$$q_+ = e \sum_i |a_i - b_i| \quad a_i - b_i < 0; \tag{7}$$

$$OHF = 42 \cdot q; \tag{8}$$

where $\sum_i a_i = 1, \sum_i b_i = 1$ and $q = q_+ = q_-$. Index i denotes the number of fragments (atoms, phenyl groups, or carbazole groups); a_i and b_i are the contribution percentages of different molecular fragments in the highest occupied and the lowest unoccupied molecular orbitals (HOMO and LUMO), respectively. OHF refers to the Optimal Hartree-Fock exchange energy amount in percentage.

3.1.2.6. Preparation of Solar Cells

Organic solar cells were prepared by thermal deposition in a vacuum chamber (Kurt J. Lesker, UK) with a base pressure of 10^{-8} mbar. Glass substrates with prestructured indium tin oxide (ITO) were purchased from *TFD* (USA). C_{60} (CreaPhys, Germany) doped with tetrakis(1,3,4,6,7,8-hexahydro-2H-pyrimido [1,2-a]pyrimidinate)ditungsten (II) (W2(hpp)4, Novaled, Germany) was used as the electron transport layer. The hole transport layer consisted of 9,9-bis[4-(N,N-bis-biphenyl-4-yl-amino)phenyl]-9H-fluorene (BPAPF, LumTec, Taiwan) doped with NDP9[2] (Novaled, Germany). Aluminum (Kurt J. Lesker) was used as the top electrode. The area of the solar cells was 6.44 mm². In order to determine the layer thickness by using QCMs, the following densities were used: r(C_{60})=1.63 g cm⁻³, r(W2(hpp)4)=1.63 g cm⁻³, r(BPAPF)=1.2 g cm⁻³, r(NDP9)=1.2 g cm⁻³, r(Al)=2.7 g cm⁻³. The density of 1.3 g cm⁻³ was used for **DTA-BTN**. Elevated substrate temperatures were achieved by heating the backside of the substrates with halogen lamps. The substrate temperatures are known by calibration and are

---

[2] The chemical structure of NDP9 is a commercial secret protected by Novaled, Germany.

not measured during the deposition. Deviations in the substrate temperature are expected to be less than DT=5 K. The absorber layers were deposited with the deposition rates around 0.2–0.4 Å s^{-1}, BPAPF at 0.6 Å s^{-1}, n-doped C$_{60}$ at 0.3 Å s^{-1}, and the aluminum layer at 2 Å s^{-1}.

3.1.2.7. Preparation of Solution-Processed OLEDs

Electroluminescent devices with the following configuration were fabricated: ITO/poly 3,4-ethylenedioxythiophene:polystyrenesulfonate (PEDOT:PSS)/PVK:PBD (40 wt%): **TR2** (3 wt%)/LiF/Al (device I), ITO/PEDOT:PSS/PVK:PBD (40 wt%):**TR3**(3 wt%)/LiF/Al (device II). PEDOT:PSS was used for hole transport layer (HTL). The ITO-coated glass substrates were cleaned by ultrasonic treatment in deionized water, acetone and isopropanol step by step during 15 min for each solution. The layer of PEDOT:PSS was obtained on the glass substrate with the ITO sublayer by spin coating the 1:2 solution with methanol at a speed of substrate rotation of ca. 2000 rpm. The fabricated layer of PEDOT:PSS was dried at 200 °C for 10 min. The active light emitting layers PVK:PBD (60/40 wt%) doped by 3% of **TR2** or **TR3** with the thickness of 70 nm were spin coated from chlorobenzene solution on the top of PEDOT:PSS. The speed of the substrate rotation was 2000 rpm, and after 10 s it was increased to 3000 for 10 s. After drying the active layers at 90 °C for 30 min, the top electrode LiF/Al was deposited through the shadow mask by means of thermal vacuum evaporation at the pressure of ca. 10^{-5} Torr. The thickness of the layers was measured with a profilometer (Dektak XT, Bruker). The current density-voltage characteristics of the fabricated OLEDs were recorded with a *Keithley 2400 Source Meter*. The luminance and the color of the light emission of the fabricated devices were measured with a *Minolta CS−200* camera. The electroluminescence spectra were recorded with a *MicroHR* spectrometer and a CCD camera *3500* (Horriba Jobin Yvon). The photoluminescence spectra (PL) of the active layers containing **TR2** and **TR3** and without them were recovered by a *FLS980* fluorescence spectrometer with *TMS300* monochromators and a red cooled detector (Hamamatsu R928P). The standard light source for measuring the PL spectra was a 450 W xenon arc lamp. The absorption (UV) spectra of the films PVK:PBD, PVK:PBD:**TR2**, PVK:PBD:**TR3** were recorded with a *Cary 5000* UV−Vis−NIR spectrophotometer. All the measurements were carried out at room temperature.

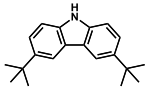### 3.1.2.8. Preparation of Vacuum Deposited OLEDs

Pre-cleaned 22x22 mm ITO-coated glass substrates were treated with O$_2$ plasma for 5 min. The substrates were then inserted into inert gas atmosphere and subsequently into a high vacuum (8·10^{-5} Pa) chamber. The organic layers were deposited by thermal evaporation onto the substrates with the evaporation rates of 0.06–0.1 nm/s. Next, a cathode was fabricated by thermally evaporating LiF (0.8 nm) and Al (100 nm) with the rates of 0.01 nm/s and 1.5–2 nm/s, respectively. The pixel size of each OLED was 1 mm^2 with a total of 6 pixels per substrate. After evaporation, the OLEDs were encapsulated with a clear glass cover in order
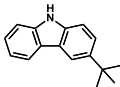
to prevent the detrimental effects of O_2 and H_2O. The voltage, current and luminance characteristics of the OLEDs were measured in the ambient air atmosphere with a *Keithley 2601A Source Meter*, an *Orb Optronics ETO TEC 100* characterization system and a *RadOMA GS-1290* spectroradiometer.
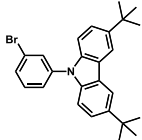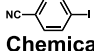
3.2. Materials

The starting compounds, i.e., 9*H*-carbazole (97%), 2-chloro-2-methylpropane (99%), aluminum trichloride (98%), 1-bromo-3-iodobenzene (97%), Cu (99%), 18-crown-6 (98%), K_2CO_3 (99%), 2-aminobenzonitrile (98%), 3-aminobenzonitrile (98%), 4-aminobenzonitrile (98%), KI (99%), $NaNO_2$ (97%), conc. HCl, CF_3SO_3H (98%), CH_3COOH (99.9%), KIO_3 (99%), NaOH (99%), 1-bromohexane (98%), tetrabutylammonium hydrogen sulfate (99%), ethynyltrimethylsilane (99%), $Pd(PPh_3)_2Cl_2$ (98%), $Pd(OAc)_2$ (98%), DPPF (99%), CuI (99%), CuCN (99%), *n*-Bu_4NF 1M solution in THF, PPh_3 (98%), triethylamine (99%), *t*-BuOK (98%), *t*-BuONa (98%), Aliquat 336 (99%), $Pd(PPh_3)_4$ (99%), TMHD (98%), Na_2SO_4 (99%), KOH (99%), 1,3,5-tribromobenzene (97%), 4-fluorophenylboronic acid (98%), 4-cyanophenyl boronic acid pinacol ester (98%), 2,7-di-tert-butyl-9,9-dimethyl-9,10-dihydroacridine (97%) and polystyrene were purchased from *Sigma-Aldrich* and used as received. *Zeonex* cyclo-olefin polymer was purchased from *ZEON Corporation*.

The solvents, i.e., toluene, chloroform, ethyl acetate, *n*-hexane, diethyl ether, methanol, acetone, acetonitrile, THF (Penta), DCM (Poch), DCB, diisopropylamine, pyridine, DMF, DMSO (Sigma-Aldrich) were dried and distilled according the conventional procedures [150].

Chemical Formula:
$C_{20}H_{25}N$

3,6-di-tert-butyl-9H-carbazole (**1a**, FW=279.43 g/mol, m.p.=226–228 °C, lit. 228–230 °C [151]) was synthesized as described in literature source [151]. An off-white solid was obtained (the yield equaled 74%).

Chemical Formula:
$C_{16}H_{17}N$

3-(tert-butyl)-9H-carbazole (**1b**, FW=223.32 g/mol, m.p.=151–153 °C, lit. 151–152 °C [152]) was synthesized as described in literature source [151]. An off-white solid was obtained (the yield was 42%).

9-(3-bromophenyl)-3,6-di-tert-butyl-9H-carbazole (**1c**, FW=434.41 g/mol) was synthesized as described in literature source [153]. A colorless oil was produced (the yield measured 85%).

Chemical Formula:
$C_{26}H_{28}BrN$

Chemical
Formula: C_7H_4IN

4-iodobenzonitrile (**2a**, FW=229.02 g/mol, m.p.=121–123 °C, lit. 122–124 °C [154]) was synthesized as described in literature source [155]. A yellowish solid was obtained (the yield equaled 85%).
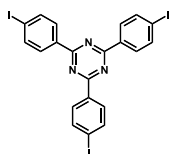
Chemical Formula: C_7H_4IN

3-iodobenzonitrile (**2b**, FW=229.02 g/mol, m.p.=40–42 °C, lit. 39–40 °C [154]) was synthesized as described in literature source [155]. An off-white solid was produced (the yield was 72%).
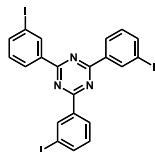
Chemical Formula: C_7H_4IN

2-iodobenzonitrile (**2c**, FW=229.02 g/mol, m.p.=53–55 °C, lit. 54–55 °C [156]) was synthesized as described in literature source [155]. An off-white solid was obtained (the yield measured 82%).

**Chemical Formula: $C_{21}H_{12}I_3N_3$**

2,4,6-tris(4-iodophenyl)-1,3,5-triazine (**3a**, FW=687.05 g/mol, m.p.=384–386 °C, lit. 386–387 °C [157]) was prepared by employing acid-catalyzed electrophilic cyclization according to the procedure reported in literature source [157]. A yellowish solid was produced (the yield equaled 85%).
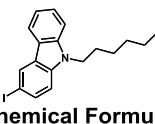
Chemical Formula: $C_{21}H_{12}I_3N_3$

2,4,6-tris(3-iodophenyl)-1,3,5-triazine (**3b**, FW=687.05 g/mol, m.p.=243–245 °C, lit. 244–245 °C [157]) was prepared by performing acid-catalyzed electrophilic cyclization according to the procedure reported in literature source [157]. An off-white solid was obtained (the yield was 88%).
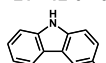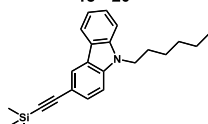
Chemical Formula: $C_{12}H_8IN$

3-iodo-9H-carbazole (**4a**, FW=293.1 g/mol, m.p.=192–194 °C, lit. 192–194 °C [158]) was synthesized as described in literature source [158]. An off-white solid was produced (the yield measured 67%).
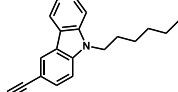
Chemical Formula: $C_{18}H_{20}IN$

9-hexyl-3-iodo-9H-carbazole (**4b**, FW=377.27 g/mol, m.p.=56–58 °C, lit. 58–60 °C [159]) was synthesized as described in literature source [159]. An off-white solid was obtained (the yield equaled 96%).

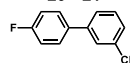**Chemical Formula: $C_{23}H_{29}NSi$**

3-(trimethylsilyl)ethynyl-9-hexylcarbazole (**4c**, FW=347.57 g/mol) was synthesized as described in literature source [159]. A yellow liquid was produced (the yield was 85%).

Chemical Formula: $C_{20}H_{21}N$

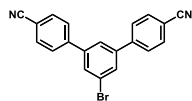**3-ethynyl-N-hexyl-carbazole** (**4d**, FW=275.39 g/mol) was synthesized as described in literature source [159]. A dark yellow liquid was obtained (the yield measured 80%).

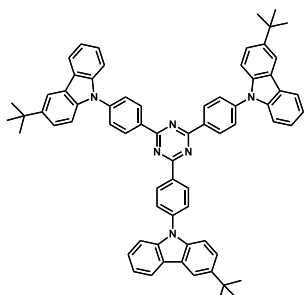**Chemical Formula: $C_{13}H_8FN$**

4'-fluoro-[1,1'-biphenyl]-3-carbonitrile (**5a**, FW=197.21 g/mol, m.p.=64–66 °C, lit. 66–68 °C [160]) was synthesized as described in literature source [160]. An off-white solid was produced (the yield was 78%).

Chemical Formula:
**C$_{20}$H$_{11}$BrN$_2$**

4-[3-bromanyl-5-(4-cyanophenyl)phenyl]benzenecarbonitrile (**5b**, FW=359.23 g/mol) was obtained by employing the standard Suzuki coupling reaction. An aqueous 2M K$_2$CO$_3$ solution (4.36 mL) containing toluene (10 mL) was added to a mixture of 1,3,5-tribromobenzene (1.00 g, 3.17 mmol), 4-cyanophenylboronic acid pinacol ester (1.45 g, 6.35 mmol), Aliquat 336 (0.1 g, 0.25 mmol) and Pd(PPh$_3$)$_4$ (0.367 g, 0.31 mmol) under argon atmosphere. The resulting solution was kept at reflux temperature for 48 hours and then cooled down to room temperature. The reaction mixture was treated with water, extracted with ethyl acetate and washed with brine twice. The organic phase was dried over anhydrous Na$_2$SO$_4$. After the evaporation of the solvents under reduced pressure, the residue was purified by performing column chromatography on silica gel by using the eluent mixture of hexane and ethyl acetate at a volume ratio of 6:1 and recrystallized from the mixture of DCM and methanol (the volume ratio was 1:4) to afford white crystals (0.82 g, the yield of 72%, m.p.=230 °C). ^{1}H NMR (300 MHz, CDCl$_3$, δ ppm): 7.81 (t, 2H, J=1.95 Hz, Ar), 7.79 (dd, 4H, J=1.60 Hz, J=1.98 Hz, Ar), 7.73 (dt, 4H, J=8.64 Hz, J=2.09 Hz, Ar), 7.70 (t, 1H, J=1.63 Hz, Ar). ^{13}C NMR (75.5 MHz, CDCl$_3$, δ ppm): 143.7, 142.1, 132.8, 130.3, 127.9, 124.9, 123.9, 118.5.

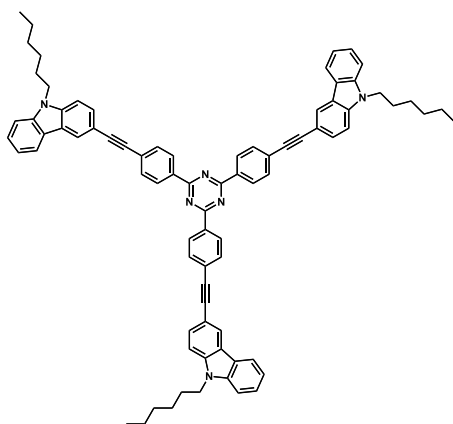**Chemical Formula: C$_{69}$H$_{60}$N$_6$**

2,4,6-Tris(4-(3-*tert*-butyl-carbazol-9-yl)phenyl)-1,3,5-triazine (**TR1**, FW=973.29 g/mol). The mixture of compounds **3a** (0.20 g, 0.29 mmol), **1b** (0.39 g, 1.75 mmol) and 18-crown-6 (0.02 g, 0.03 mmol) was dissolved in DCB (10 mL), and the resulting solution was heated to reflux under nitrogen atmosphere. Then, K$_2$CO$_3$ (0.41 g, 0.99 mmol) and Cu (0.11 g, 0.58 mmol) were added. After stirring for 24 h (TLC control), the reaction mixture was cooled down to room temperature and subsequently filtered. The residue was carefully washed with chloroform, and the solvent was evaporated under vacuum. The product was purified by employing silica gel column chromatography while using a mixture of hexane and dichloromethane in the volume ratio of 4:1 as an eluent, and recrystallized from the eluent mixture of solvents to afford yellowish crystals (0.24 g, 43% yield). m.p.=346−348 °C (DSC 344 °C). IR (KBr), v/cm^{-1}: 3042, 2955, 2901, 2864, 1604, 1588, 1572, 1508, 1487, 1455, 1412, 1367, 1327, 1294, 1256, 1229, 1172, 1150, 1015, 813, 767, 744, 730, 636, 517. ^{1}H NMR (300 MHz, CDCl$_3$, δ ppm): 9.13 (d, 6H, J=8.63 Hz, Ar); 8.25 (d, 3H, J=4.17 Hz, Ar); 8.24 (d, 3H, J=1.37 Hz, Ar); 7.92 (d, 6H, J=8.64 Hz, Ar); 7.66 (d, 3H, J=8.13 Hz, Ar); 7.60 (d, 6H, J=1.04 Hz, Ar); 7.50 (td, 3H, J=7.17 Hz, J=1.17 Hz, Ar); 7.38 (td, 3H, J=7.95 Hz, J=0.86 Hz, Ar); 1.54 (s, 27H, CH$_3$–). ^{13}C NMR (75.5 MHz, CDCl$_3$, δ ppm): 171.4, 143.9, 142.4, 140.8, 138.7, 134.6, 130.9, 126.7, 126.3, 124.4, 123.8, 120.6, 116.8, 110.2, 109.7, 35.1, 32.2. Elemental analysis yielded the following results: C 85.18%; H 6.20%; N 8.62%; molecular formula C$_{69}$H$_{60}$N$_6$ requires: C 85.15%; H 6.21%; C 8.63%. MS (APCI$^+$,

20 V) found: [M+H]$^+$ *m/z*: 974; molecular formula $C_{69}H_{60}N_6$ requires M=973.29 g/mol.
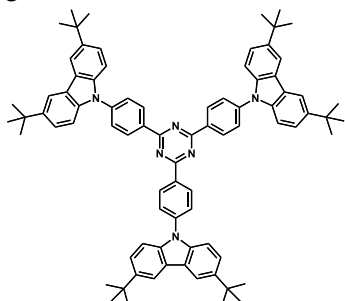
Chemical Formula: $C_{81}H_{84}N_6$

2,4,6-Tris(4-(3,6-di-*tert*-butyl-carbazol-9-yl)phenyl)-1,3,5-triazine (**TR2**, FW=1141.61 g/mol). **TR2** was prepared by conducting the Ullmann coupling reaction from **3a** (0.38 g, 0.55 mmol) and **1a** (0.93 g, 3.32 mmol) while using the same procedure as the one for the synthesis of **TR1**. The product was purified by performing silica gel column chromatography while using a mixture of hexane and dichloromethane in the volume ratio of 6:1 as an eluent, and recrystallized from the eluent mixture of solvents to afford yellowish crystals (0.31 g, 49% yield). m.p.=451−452 °C (DSC 448 °C). IR (KBr), *v*/cm^{-1}: 3048, 2960, 2903, 2866, 1604, 1590, 1570, 1509, 1489, 1471, 1410, 1367, 1324, 1297, 1261, 1232, 1175, 1150, 1035, 1016, 878, 841, 810, 612. ^{1}H NMR (300 MHz, CDCl$_3$, δ ppm): 9.11 (d, 6H, *J*=8.71 Hz, Ar); 8.21 (dd, 6H, *J*=1.64 Hz, *J*=0.85 Hz, Ar); 7.89 (d, 6H, *J*=8.72 Hz, Ar); 7.60 (d, 1H, *J*=0.74 Hz, Ar); 7.57 (dd, 10H, *J*=1.86 Hz, *J*=1.09 Hz, Ar); 7.53 (d, 1H, *J*=1.75 Hz, Ar); 1.52 (s, 54H, CH$_3$–). ^{13}C NMR (75.5 MHz, CDCl$_3$, δ ppm): 171.4, 143.7, 142.6, 140.7, 138.9, 134.38, 130.9, 126.5, 124.1, 124.0, 120.6, 116.6, 109.7, 35.1, 32.3. Elemental analysis yielded the following results: C 85.21%; H 7.44%; N 7.35%; molecular formula $C_{81}H_{84}N_6$ requires: C 85.22%; H 7.42%; N 7.36%. MS (APCI$^+$, 20 V), found: [M+H]$^+$ *m/z*: 1142; molecular formula $C_{81}H_{84}N_6$ requires M=1141.61 g/mol.
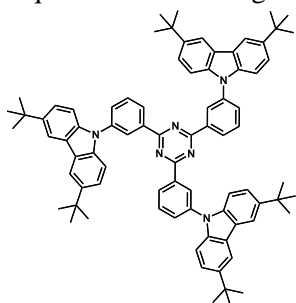

Chemical Formula: $C_{81}H_{72}N_6$

2,4,6-Tris(4-((9-hexyl-carbazol-3-yl)ethynyl)phenyl)-1,3,5-triazine (**TR3**, FW=1129.52 g/mol). Compound **3a** (0.80 g, 1.16 mmol) was suspended in triethylamine (20 mL) in a dry 100 mL two-necked flask, and the resulting mixture was heated to reflux under nitrogen atmosphere. Then, Pd(PPh$_3$)$_2$Cl$_2$ (0.05 g, 0.07 mmol), CuI (8.00 mg, 0.04 mmol) and **4d** (1.44 g, 5.24 mmol) were added. The reaction mixture was stirred for 24 hours at 90 ^{o}C. Then the solvent was evaporated under vacuum, and the residue was extracted with chloroform.

The organic phase was dried over anhydrous Na$_2$SO$_4$. After the evaporation of the solvents under reduced pressure, the product was purified by conducting silica gel column chromatography while using a mixture of hexane and chloroform in the volume ratio of 9:1 as an eluent, and precipitated into methanol to afford a yellowish solid (0.44 g, 34% yield). IR (KBr, cm^{-1}): *v*=3048, 2924, 2853, 2203, 1595, 1568, 1505, 1477, 1369, 1352, 1175, 1124, 813, 744, 726. ^{1}H NMR (300 MHz, CDCl$_3$, δ ppm): 8.77 (d, 6H, *J*=8.53 Hz, Ar); 8.38 (d, 3H, *J*=1.35 Hz, Ar);

8.14 (d, 3H, J=7.55 Hz, Ar); 7.79 (d, 6H, J=8.55 Hz, Ar); 7.73 (dd, 3H, J=8.48 Hz, J=1.56 Hz, Ar); 7.53 (t, 3H, J=7.04 Hz, Ar); 7.44 (d, 3H, J=8.20 Hz, Ar); 7.39 (d, 3H, J=8.62 Hz, Ar) 7.30 (t, 3H, J=7.02 Hz, Ar); 4.29 (t, 6H, J=7.08 Hz, –N–CH$_2$–); 1.89 (quin, 6H, J=6.23 Hz, –CH$_2$–); 1.29–1.45 (m, 18H, –CH$_2$–); 0.92 (t, 9H, J=6.86 Hz, –CH$_3$). ^{13}C NMR (75.5 MHz, CDCl$_3$, δ ppm): 171.2, 141.1, 140.5, 135.4, 131.8, 129.7, 129.1, 128.5, 126.4, 124.5, 123.1, 122.7, 120.8, 119.6, 113.1, 109.2, 109.0, 94.4 (–C≡C–), 88.1 (–C≡C–), 43.4 (–N–C–), 31.8, 29.2, 27.2, 22.8, 14.3. Elemental analysis yielded the following results: C 86.14%; H 6.41%; N 7.45%; molecular formula C$_{81}$H$_{72}$N$_6$ requires: C 86.13%; H 6.43%; N 7.44%. MS (APCI$^+$, 20 V) found: [M+H]$^+$ m/z: 1130; molecular formula C$_{81}$H$_{72}$N$_6$ requires M=1129.52 g/mol.

Chemical Formula: C$_{81}$H$_{84}$N$_6$

2,4,6-Tris(3-(3,6-di-tert-butyl-9H-carbazol-9-yl)phenyl)-1,3,5-triazine (**mTR2**, FW=1141.61 g/mol) was prepared by performing the Ullmann coupling reaction [161]. **3b** (0.80 g, 1.16 mmol), **1a** (1.56 g, 7.00 mmol) and 18-crown-6 (0.08 g, 0.12 mmol) were dissolved in DCB (20 mL), and the resulting solution was heated to reflux under nitrogen atmosphere. Then, K$_2$CO$_3$ (1.64 g, 3.96 mmol) and Cu (0.44 g, 2.32 mmol) were added. After stirring for 24 h (TLC control), the reaction mixture was cooled down to room temperature and filtered. The residue was carefully washed with chloroform, and the solvent was evaporated under vacuum. The product was purified by employing silica gel column chromatography while using a mixture of hexane and dichloromethane in the volume ratio of 4:1 as an eluent, and recrystallized from the eluent mixture of solvents to afford off-white crystals (0.95 g, 72% yield). m.p.=385–387 °C (DSC 388 °C at a heating rate of 10 °C/min). ^{1}H NMR (400 MHz, CDCl$_3$, δ ppm): 8.89 (d, J=8.7 Hz, 3H), 8.72 (d, J=8.0 Hz, 3H), 8.24 (d, J=7.3 Hz, 6H), 7.78 (d, J=7.7 Hz, 3H), 7.70 (t, J=8.0 Hz, 3H), 7.40 (d, J=8.0 Hz, 6H), 7.33 (t, J=7.0 Hz, 6H), 1.50 (s, 54H, CH$_3$–). ^{13}C NMR (75.5 MHz, CDCl$_3$, δ ppm): 171.4, 140.8, 138.3, 137.8, 131.3, 130.3, 128.1, 127.6, 126.1, 123.4, 120.3, 120.1, 109.6, 35.1, 32.3. Elemental analysis detectedd: C 85.23%; H 7.41%; N 7.36%; molecular formula C$_{81}$H$_{84}$N$_6$ requires C 85.22%; H 7.42%; N 7.36%. MALDI-TOF MS (m/z) calculated for C$_{81}$H$_{84}$N$_6$ 1141.61 (M$^+$ + H), found: 1140.
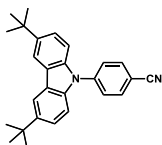
Chemical Formula: C$_{27}$H$_{28}$N$_2$

4-(3,6-Di-tert-butyl-9H-carbazol-9-yl)benzonitrile (**pBNC**, FW=380.54 g/mol, m.p.=214−216 °C, lit. 212–214 °C [162]) was prepared by employing Ullmann condensation similarly to the synthesis of compound **TR1**. A mixture of **1a** (1.00 g, 3.57 mmol), **2a** (0.98 g, 4.29 mmol) and 18-crown-6 (0.09 g, 0.35 mmol) was dissolved in DCB (10 mL), and the resulting solution was heated to reflux under nitrogen atmosphere. Then, K$_2$CO$_3$ (1.68 g, 100.00 mmol) and Cu (0.45 g, 7.00 mmol) were added. After stirring for 24 h (TLC control), the reaction mixture was cooled down to room temperature and filtered. The residue

was carefully washed with chloroform. After evaporation of the solvents under reduced pressure, the product was purified by performing silica gel column chromatography while using a mixture of hexane and ethyl acetate in the volume ratio of 9:1 as an eluent, and crystallized from hexane to afford white crystals (1.01 g, 74% yield). ^{1}H NMR (300 MHz, CDCl$_3$, δ ppm): 7.79 (d, 2H, J=1.40 Hz, Ar), 7.76 (q, 4H, J=8.68 Hz, Ar), 7.52 (d, 2H, J=7.51 Hz, Ar), 7.19 (dd, 2H, J=7.50 Hz, J=1.39 Hz, Ar), 1.44 (s, 18H, –CH$_3$). ^{13}C NMR (75.5 MHz, CDCl$_3$, δ ppm): 144.1, 142.6, 138.2, 133.8, 126.5, 124.1, 124.0, 118.5, 116.5, 109.8, 109.1, 34.8 (–C–CH$_3$), 31.9 (–CH$_3$). Elemental analysis found: C 85.18%; H 6.20%; N 8.62%; molecular formula C$_{27}$H$_{28}$N$_2$ requires: C 85.15%; H 6.21%; N 8.63%. MS (APCI$^+$, 20 V), found: [M+H]$^+$ m/z: 380.1; molecular formula C$_{27}$H$_{28}$N$_2$ requires: M=380.23 g/mol.
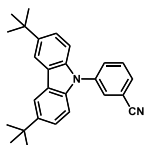
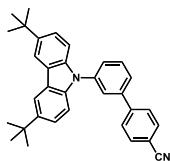Chemical Formula: C$_{27}$H$_{28}$N$_2$

3-(3,6-Di-tert-butyl-9H-carbazol-9-yl)benzonitrile (*m*BNC) was prepared by employing the Rosenmund Von Braun reaction [163]. In a dry Schlenk reactor, **1c** (1.00 g, 2.30 mmol) and CuCN (0.31 g, 3.45 mmol) were degassed, and 10 ml of dry DMF was added under argon. After being heated under reflux for 24 h (TLC control), the reaction mixture was cooled down to room temperature and filtered. The residue was carefully washed with chloroform, diluted with 30% aq ammonia (10 ml) as well as water, and extracted. The organic phase was dried over anhydrous Na$_2$SO$_4$, and the solvent was evaporated under vacuum. The product was purified by performing silica gel column chromatography while using a mixture of hexane and ethyl acetate in the volume ratio of 9:1 as an eluent and recrystallized from hexane to afford white crystals (0.72 g, 82% yield). m.p.=146−148 °C (DSC 150 °C at a heating rate of 10 °C/min). ^{1}H NMR (300 MHz, CDCl$_3$, δ ppm): 7.95 (t, 1H, J=1.42 Hz, Ar), 7.80 (dt, 1H, J=5.64 Hz, J=1.58 Hz), 7.78 (d, 2H, J=1.40 Hz, Ar), 7.56–7.61 (m, 2H, Ar), 7.51 (d, 2H, J=7.50 Hz, Ar), 7.18 (dd, 2H, J=7.51 Hz, J=1.38 Hz, Ar), 1.44 (s, 18H, –CH$_3$). ^{13}C NMR (75.5 MHz, CDCl$_3$, δ ppm): 143.8, 139.4, 138.6, 131.0, 130.9, 130.2, 124.0, 123.8, 118.1, 116.5, 114.1, 108.8, 34.8 (–C–CH$_3$), 31.9 (–CH$_3$). Elemental analysis found: C 85.18%; H 6.20%; N 8.62%; molecular formula C$_{27}$H$_{28}$N$_2$ requires: C 85.15%; H 6.21%; C 8.63%. MS (APCI$^+$, 20 V), found: [M+H]$^+$ m/z: 380.2; molecular formula C$_{27}$H$_{28}$N$_2$ requires: M=380.23 g/mol.
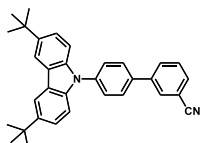
Chemical Formula: C$_{33}$H$_{32}$N$_2$

4'-(3,6-Di-tert-butyl-9H-carbazol-9-yl)-[1,1'-biphenyl]-3-carbonitrile (*m*BNPC) was synthesized by employing the electrophilic substitution reaction. A mixture of **1a** (1.00 g, 3.57 mmol) and K$_2$CO$_3$ (0.74 g, 5.36 mmol) in DMSO (10 ml) was stirred at room temperature for 1 h. Then, **5a** (0.70 g, 3.57 mmol) was added, and the reaction mixture was heated up to 150 °C. After being heated at the same temperature for 24 h (TLC control), the reaction mixture was cooled down to room temperature, diluted with ethyl acetate as well as water, and extracted. The organic phase was dried over anhydrous Na$_2$SO$_4$, and the solvent

was evaporated under vacuum. The product was purified by performing silica gel column chromatography while using a mixture of hexane and ethyl acetate in the volume ratio of 9:1 as an eluent, and recrystallized from the mixture of DCM and isopropanol (the volume ratio of 1:4 was used) to afford white crystals (1.27 g, 78% yield). m.p.=189−191 °C (DSC 192 °C at a heating rate of 10 °C/min). ^{1}H NMR (300 MHz, CDCl$_3$, δ ppm): 8.20 (d, 2H, J=1.57 Hz, Ar), 8.00 (t, 1H, J=1.48 Hz, Ar), 7.94 (dt, 1H, J=7.89 Hz, J=1.28 Hz, Ar), 7.80 (d, 2H, J=1.28 Hz, Ar), 7.72 (d, 3H, J=8.17 Hz, Ar), 7.63 (t, 1H, J=7.79 Hz, Ar), 7.52 (dd, 2H, J=8.66 Hz, J=1.91 Hz, Ar), 7.45 (d, 2H, J=8.59 Hz, Ar), 1.51 (s, 18H, –CH$_3$). ^{13}C NMR (75.5 MHz, CDCl$_3$, δ ppm): 143.2, 141.6, 139.0, 138.6, 137.2, 131.4, 130.9, 130.7, 129.8, 128.4, 127.1, 123.7, 123.6, 118.8, 116.4, 113.2, 109.2, 34.8 (–C–CH$_3$), 32.0 (–CH$_3$). Elemental analysis found: C 86.85%; H 7.07%; N 6.08%; molecular formula C$_{33}$H$_{32}$N$_2$ requires: C 86.80%; H 7.06%; N 6.13%. MS (APCI$^+$, 20 V), found: [M+H]$^+$ m/z: 455.9; molecular formula C$_{33}$H$_{32}$N$_2$ requires: M=456.26 g/mol.

Chemical Formula: C$_{33}$H$_{32}$N$_2$

3'-(3,6-Di-tert-butyl-9H-carbazol-9-yl)-[1,1'-biphenyl]-4-carbonitrile (*p*BNPC) was obtained by performing the standard Suzuki procedure from **1c** (1.00 g, 2.30 mmol) and 4-cyanophenylboronic acid pinacol ester (0.55 g, 2.41 mmol) while using the same procedure as for the synthesis of **5b**. The product was purified by performing silica gel column chromatography while using a mixture of hexane and ethyl acetate in the volume ratio of 9:1 as an eluent, and recrystallized from the mixture of DCM and isopropanol (the volume ratio of 1:4 was used) to afford white crystals (0.89 g, 85% yield). m.p.=208−210 °C (DSC 212 °C at a heating rate of 10 °C/min). ^{1}H NMR (300 MHz, CDCl$_3$, δ ppm): 8.08 (d, 2H, J=1.83 Hz, Ar), 7.71 (t, 1H, J=1.77 Hz, Ar), 7.64−7.67 (m, 4H, Ar), 7.61 (t, 1H, J=7.75 Hz, Ar), 7.53−7.56 (m, 2H, Ar), 7.39 (dd, 2H, J=8.60 Hz, J=1.89 Hz, Ar), 7.30 (d, 2H, J=8.59 Hz, Ar), 1.39 (s, 18H, –CH$_3$). ^{13}C NMR (75.5 MHz, CDCl$_3$, δ ppm): 144.6, 143.2, 140.9, 139.2, 132.8, 130.6, 127.8, 126.8, 125.7, 125.4, 123.7, 123.5, 118.8, 116.4, 111.5, 109.1, 34.8 (–C–CH$_3$), 32.0 (–CH$_3$). Elemental analysis found: C 86.82%; H 7.09%; N 6.09%; molecular formula C$_{33}$H$_{32}$N$_2$ requires: C 86.80%; H 7.06%; N 6.13%. MS (APCI$^+$, 20 V), found: [M+H]$^+$ m/z: 456.4; molecular formula C$_{33}$H$_{32}$N$_2$ requires: M=456.26 g/mol.
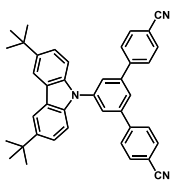
Chemical Formula: C$_{40}$H$_{35}$N$_3$

5'-(3,6-Di-tert-butyl-9H-carbazol-9-yl)-[1,1':3',1''-terphenyl]-4,4''-dicarbonitrile (2BNPC) was prepared by performing the Ullmann coupling reaction from **1a** (0.50 g, 1.78 mmol) and **5b** (0.93 g, 3.32 mmol) while using the same procedure as for the synthesis of *p*BNC. The product was purified by conducting silica gel column chromatography while using a mixture of hexane and ethyl acetate in the volume ratio of 9:1 as an eluent, and recrystallized from a mixture of DCM and isopropanol (the volume ratio of 1:4 was used) to afford white crystals (0.68 g, 69% yield). m.p.=322−324

°C (DSC 327 °C at a heating rate of 10 °C/min). ^{1}H NMR (300 MHz, CDCl$_3$, δ ppm): 8.10 (d, 2H, J=1.58 Hz, Ar), 7.78 (d, 2H, J=1.60 Hz, Ar), 7.75 (t, 1H, J=1.55 Hz, Ar), 7.72 (d, 8H, J=1.52 Hz, Ar), 7.43 (dd, 2H, J=8.60 Hz, J=1.85 Hz, Ar), 7.36 (d, 2H, J=8.59 Hz, Ar), 1.40 (s, 18H, –CH$_3$). ^{13}C NMR (75.5 MHz, CDCl$_3$, δ ppm): 143.2, 142.5, 140.9, 139.0, 137.9, 131.9, 126.9, 124.3, 123.4, 122.9, 122.7, 117.5, 115.5, 110.9, 107.9, 33.8 (–C–CH$_3$), 30.9 (–CH$_3$). Elemental analysis found: C 86.19%; H 6.35%; N 7.46%; molecular formula C$_{40}$H$_{35}$N$_3$ requires: C 86.14%; H 6.33%; N 7.53%. MS (APCI$^+$, 20 V), found: [M+H]$^+$ *m/z*: 557.2; molecular formula C$_{40}$H$_{35}$N$_3$ requires: M=557.74 g/mol.
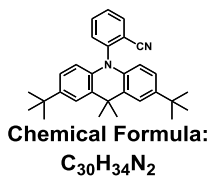

Chemical Formula:
C$_{30}$H$_{34}$N$_2$
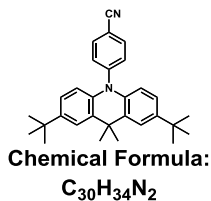
4-(2,7-Di-tert-butyl-9,9-dimethylacridin-10(9H)-yl)benzonitrile (*p*BNA) was prepared by performing the Buchwald-Hartwig amination reaction [164]. In a dry Schlenk reactor, 2,7-di-tert-butyl-9,9-dimethyl-9,10-dihydroacridine (1.00 g, 3.11 mmol) and **2a** (0.78 g, 3.42 mmol) were degassed, and 10 ml of dry toluene was added under argon. Then, *t*-BuONa (0.89 g, 9.33 mmol) was added, and the reaction mixture was degassed. Finally, DPPF (0.17 g, 0.31 mmol) and Pd(OAc)$_2$ (0.07 g, 0.31 mmol) were added. The reaction mixture was degassed and heated under reflux. After being heated at the same temperature for 24 h (TLC control), the reaction mixture was cooled down to room temperature, diluted with ethyl acetate as well as water, and extracted. The organic phase was dried over anhydrous Na$_2$SO$_4$, and the solvent was evaporated under vacuum. The obtained product was purified by employing silica gel column chromatography while using a mixture of hexane and toluene in the volume ratio of 5:1 as an eluent, and recrystallized from a mixture of DCM and isopropanol (the volume ratio of 1:4 was used) to afford white crystals (0.98 g, 75% yield). m.p.=286−288 °C (DSC 290 °C at a heating rate of 10 °C/min). ^{1}H NMR (400 MHz, DMSO-d$_6$, δ ppm): 8.06 (d, 2H, J=8.49 Hz, Ar), 7.55 (d, 2H, J=8.56 Hz, Ar), 7.48 (d, 1H, J=2.22 Hz, Ar), 7.25 (d, 1H, J=7.30 Hz, Ar), 7.18 (d, 1H, J=7.28 Hz, Ar), 7.06 (dd, 1H, J=8.60 Hz, J=2.16 Hz, Ar), 6.27 (d, 2H, J=8.53 Hz, Ar), 1.62 (s, 6H, –CH$_3$), 1.26 (s, 18H, –CH$_3$). ^{13}C NMR (100 MHz, DMSO-d$_6$, δ ppm): 143.3, 142.1, 138.5, 137.2, 135.7, 133.0, 132.7, 129.6, 123.4, 122.9, 118.7, 114.3, 113.5, 34.6, 32.2, 31.6, 31.5. Elemental analysis found: C 85.31%; H 8.12%; N 6.57%; molecular formula C$_{30}$H$_{34}$N$_2$ requires: C 85.26%; H 8.11%; N 6.63%. MS (APCI$^+$, 20 V), found: [M+H]$^+$ *m/z*: 422.7; molecular formula C$_{30}$H$_{34}$N$_2$ requires: M=422.62 g/mol.

Chemical Formula:
C$_{30}$H$_{34}$N$_2$
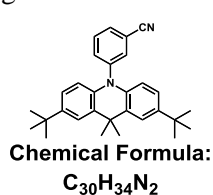
3-(2,7-Di-tert-butyl-9,9-dimethylacridin-10(9H)-yl)benzonitrile (*m*BNA) was obtained by conducting the Buchwald-Hartwig amination reaction from 2,7-di-tert-butyl-9,9-dimethyl-9,10-dihydroacridine (1.00 g, 3.11 mmol) and **2b** (0.78 g, 3.42 mmol) while using the same procedure as for the synthesis of *p*BNA. The product was purified by performing silica gel column chromatography while using a mixture of hexane and toluene in the volume ratio of 5:1 as an eluent, and recrystallized from a mixture of DCM and isopropanol (the volume ratio of 1:4 was used) to afford

white crystals (1.06 g, 81% yield). m.p.=183−195 °C (DSC 198 °C at a heating rate of 10 °C/min). ^{1}H NMR (400 MHz, DMSO-d$_6$, δ ppm): 8.03 (d, 1H, J=7.55 Hz, Ar), 7.95 (t, 1H, J=0.52 Hz, Ar), 7.88 (t, 1H, J=7.84 Hz, Ar), 7.74 (t, 1H, J=7.31 HZ, Ar), 7.47 (d, 2H, J=1.85 Hz, Ar), 7.00 (dd, 2H, J=8.49 Hz, J=2.04 Hz, Ar), 6.00 (d, 2H, J=8.54 Hz, Ar), 1.66 (s, 6H, –CH$_3$), 1.26 (s, 18H, –CH$_3$). ^{13}C NMR (100 MHz, DMSO-d$_6$, δ ppm): 143.2, 142.4, 138.1, 137.2, 135.5, 132.9, 132.7, 129.7, 123.8, 122.7, 118.5, 114.6, 113.6, 34.3, 32.3, 31.7, 31.1. Elemental analysis found: C 85.29%; H 8.09%; N 6.62%; molecular formula C$_{30}$H$_{34}$N$_2$ requires: C 85.26%; H 8.11%; N 6.63%. MS (APCI$^+$, 20 V) found: [M+H]$^+$ m/z: 422.5; molecular formula C$_{30}$H$_{34}$N$_2$ requires: M=422.62 g/mol.

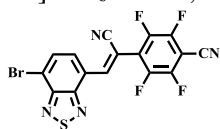Chemical Formula: C$_{30}$H$_{34}$N$_2$

2-(2,7-Di-tert-butyl-9,9-dimethylacridin-10(9H)-yl)benzonitrile (oBNA) was obtained by performing the Buchwald-Hartwig amination reaction from 2,7-di-tert-butyl-9,9-dimethyl-9,10-dihydroacridine (1.00 g, 3.11 mmol) and **2c** (0.78 g, 3.42 mmol) while using the same procedure as for the synthesis of **pBNA**. The product was purified by conducting silica gel column chromatography while using a mixture of hexane and toluene in the volume ratio of 5:1 as an eluent, and recrystallized from a mixture of DCM and isopropanol (the volume ratio of 1:4 was used) to afford white crystals (0.87 g, 66% yield). m.p.=238−240 °C (DSC 242 °C at a heating rate of 10 °C/min). ^{1}H NMR (400 MHz, DMSO-d$_6$, δ ppm): 8.20 (dd, 1H, J=7.76 Hz, J=1.36 Hz, Ar), 8.03 (td, 1H, J=7.77 Hz, J=1.48 Hz, Ar), 7.89 (td, 1H, J=7.68 Hz, J=0.84 Hz, Ar), 7.64 (d, 1H, J=7.86 Hz, Ar), 7.51 (d, 2H, J=2.19 Hz, Ar), 7.02 (dd, 2H, J=8.59 Hz, J=2.21 Hz, Ar), 5.92 (d, 2H, J=8.56 Hz, Ar), 1.69 (s, 6H, –CH$_3$), 1.27 (s, 18H, –CH$_3$). ^{13}C NMR (100 MHz, DMSO-d$_6$, δ ppm): 143.9, 143.5, 137.6, 136.6, 136.0, 133.6, 130.1, 129.6, 123.9, 122.9, 117.0, 115.2, 112.9, 36.4, 34.4, 31.8. Elemental analysis found: C 85.28%; H 8.13%; N 6.59%; molecular formula C$_{30}$H$_{34}$N$_2$ requires: C 85.26%; H 8.11%; N 6.63%. MS (APCI$^+$, 20 V) found: [M+H]$^+$ m/z: 422.7; molecular formula C$_{30}$H$_{34}$N$_2$ requires: M=422.62 g/mol.

Chemical Formula: C$_{16}$H$_3$BrF$_4$N$_4$S

(Z)-4-(2-(7-bromobenzo[c][1,2,5]thiadiazol-4-yl)-1-cyanovinyl)-2,3,5,6-tetrafluorobenzonitrile (6a). 7-bromo-2,1,3-benzothiadiazol-4-carbaldehyde (3.04 g, 12.5 mmol) and 4-(cyanomethyl)-2,3,5,6-tetrafluorobenzonitrile (4.82 g, 18.75 mmol) were dissolved in anhydrous toluene (250 ml) under a nitrogen atmosphere. Anhydrous pyridine (25 ml) was added slowly, and the mixture was heated at 80 °C. An aliquot of anhydrous pyridine (12.5 ml) and 2-(2,3,5,6-tetrafluoro-4-(trifluoromethyl)phenyl)acetonitrile (0.64 g, 2.5 mmol) were added to the reaction mixture each hour during the first 3 h of the reaction. The reaction mixture was then further heated for 2 h at 80 °C (thus constituting the 5 h total reaction time). After the reaction, the mixture was cooled down to room temperature, and the solvent was evaporated under reduced pressure. The crude product was purified by conducting column chromatography on silica gel with dichloro-methane/n-pentane (v/v, 1:4) as an eluent, followed by recrystallization in ethanol to afford **6a** as a light yellow solid (5.19 g, 10.76

mmol, yield: 86%). ^{1}H NMR (500.13 MHz, CDCl$_3$, δ ppm): 8.64 (d, J_1=7.9 Hz, J_2=0.6 Hz, 1 H; Ar H), 8.40 (s, 1H, C=CH), 8.08 (d, J=7.9 Hz, 1H; Ar H); ^{13}C NMR (125.77 MHz, CDCl$_3$, δ ppm): 153.2, 153.2, 147.4 (m, incl. app. d, JC–F=270.4 Hz), 146.1, 144.0 (m, incl. app. d, J_{C-F}=259.0 Hz), 132.2, 129.2, 124.2, 119.6, 114.9, 106.8, 98.0; ^{19}F NMR (282.40 MHz, CDCl$_3$, δ ppm): -130.82 ~ -130.97 (m, J_{C-F}=258.2 Hz, 2F; Ar–F), -136.98 ~ -137.13 (m, J_{C-F}=270.8 Hz, 2F; Ar–F); IR (KBr): ν=3045, 2246, 2225, 1647, 1522, 1484, 1303, 1276, 1116, 1045, 982, 878, 834 cm^{-1}; HRMS (EI) m/z: [M]$^+$ calculated for C$_{16}$H$_3$BrF$_4$N$_4$S, 437.9198; found: 437.9204.

Chemical Formula: C$_{34}$H$_{19}$F$_4$N$_5$S$_2$
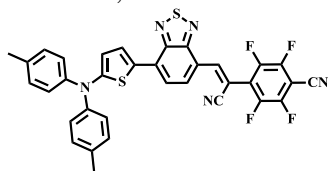
(Z)-4-(1-cyano-2-(7-(5-(di-p-tolylamino)thiophen-2-yl)benzo[c][1,2,5]thiadiazol-4-yl)vinyl)-2,3,5,6-tetrafluorobenzonitrile (DTA-BTN). 6a (1.15 g, 2.38 mmol), freshly made N,N-di-p-tolyl-5-(tributylstannyl)thiophen-2-amine (2.86 mmol) and bis(triphenylphosphine) palladium(II) dichloride (0.05 g, 0.07 mmol) were dissolved in anhydrous toluene (150 ml) under a nitrogen atmosphere. The mixture was then heated at 80 ~ 90 °C for 2 h. After the mixture was cooled to room temperature, 5 g potassium fluoride was added and stirred for 1 h. The reaction mixture was filtered over a silica gel cake and washed with toluene. After the removal of the solvent, the crude product was washed several times with ethanol, methanol, n-pentane and n-hexane till the solvent was almost colorless and then was dried under high vacuum overnight to afford **DTA–BTN** as a black-blue crystalline solid (1.52 g, 2.23 mmol, yield: 94%). mp 228 °C (DSC); ^{1}H NMR (500.13 MHz, CDCl$_3$, δ ppm): 8.78 (d, J_1=7.9 Hz, J_2=0.6 Hz, 1H; Ar−H), 8.44 (s, 1H, C=CH), 8.18 (d, J=4.1 Hz, 1H; thiophene-H), 7.71 (d, J=8.2 Hz, 1H; Ar−H), 7.21 ~ 7.16 (m, 8H, Ar H), 6.55 (d, J=4.4 Hz, 1H; thiophene-H), 2.38 (s, 6H, CH$_3$); ^{13}C NMR (125.77 MHz, CDCl$_3$, δ ppm): 159.1, 155.0, 151.7, 146.4 (m, incl. app. d, J_{C-F}=260.6 Hz), 146.2, 144.4, 143.0 (m, incl. app. d, J_{C-F}=254.9 Hz), 134.9, 132.3, 131.5, 130.2, 129.8, 127.0, 124.7, 121.9, 120.5, 116.0, 115.2, 107.1, 93.4, 21.0; ^{19}F NMR (282.40 MHz, CDCl3, δ ppm): -131.58 ~ -131.73 (m, 2F, Ar−F), -137.37 ~ -137.52 (m, 2F, Ar F); IR (KBr): ν=3028, 2916, 2213, 1648, 1530, 1457, 1425, 1346, 1266, 1150, 1060, 982, 941, 818 cm^{-1}; HRMS (EI) m/z: [M]$^+$ calculated for C$_{34}$H$_{19}$F$_4$N$_5$S$_2$, 637.1018, found 637.1004. Elemental analysis found: C 64.57%, H 2.96%, N 10.98%, S 10.33%; molecular formula C$_{34}$H$_{19}$F$_4$N$_5$S$_2$ requires: C 64.04%, H 3.00%, N 10.98%, S 10.05%.

4. RESULTS AND DISCUSSION

4.1. Fluorescent Star-Shaped Triazine Derivatives

Utilization of bipolar materials offers the possibility to achieve efficient and stable single-layer OLEDs which are highly desirable because of the simplification of the manufacturing process and the reduction of the production costs. Therefore, we selected stable electron donor (D) carbazole and acceptor (A) triazine for the design of three bipolar star-shaped triazine derivatives and

investigated their properties [165]. The newly synthesized compounds were tested in OLEDs of a simple structure.

4.1.1. Synthesis
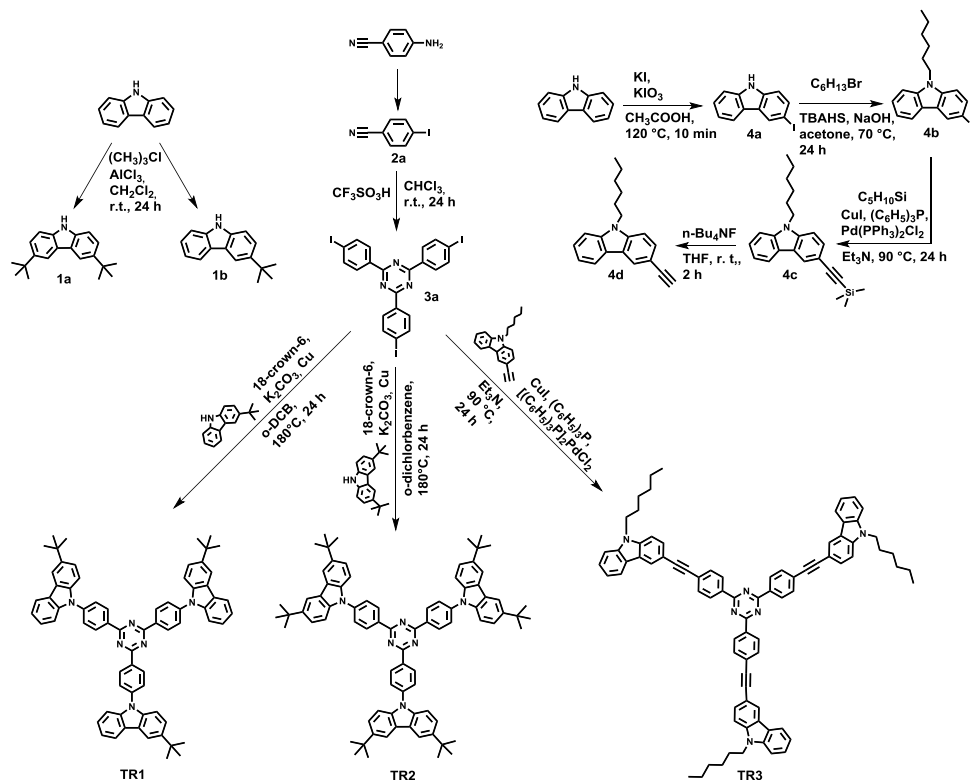
Scheme 4.1.1 Synthetic routes towards star-shaped TRZ derivatives

Star-shaped derivatives of 2,4,6-triphenyl-1,3,5-triazine and carbazole were synthesized by following the synthetic routes shown in **Scheme 4.1.1**. **TR1** and **TR2** were obtained by conducting the above outlined four-step synthesis. At the first step, 4-iodobenzonitrile (**2a**) was obtained from 4-aminobenzonitrile via the diazotization-iodination reaction. Then, **2a** was subjected to cyclization with the help of trifluoromethansulfonic acid to furnish 2,4,6-tris(*p*-iodophenyl-)1,3,5-triazine (**3a**). At the third step, the alkylation of carbazole in presence of 2-chloro-2-methylpropane and AlCl$_3$ was carried out. The alkylation products, specifically, 3,6-di-*tert*-butylcarbazole (**1a**) and 3-*tert*-butylcarbazole (**1b**), were isolated. At the final step, compound **3a** and carbazole derivatives **1a** and **1b** were subjected to the Ullmann coupling [161] in order to obtain target compounds **TR1** and **TR2**. The synthetic route to compound **TR3** included seven stages. Compound **4d** was synthesized following the established routes [159] and finally was coupled with **3a** by performing the Hagihara−Sonogashira cross-coupling reaction [166] to afford the target product.

The chemical structures of the target compounds were identified by mass spectrometry as well as IR and NMR spectroscopies and elemental analysis. The

data was found to be in good agreement with the proposed structures. All the compounds exhibited characteristic signals at 171.2–171.4 ppm in ^{13}C NMR spectra, which can be attributed to the carbon atoms of the triazine heterocycle. For compounds **TR1** and **TR2**, the characteristic singlet signal corresponding to the protons of the methyl group of the *tert*-butyl moiety was found at 1.54–1.55 ppm in ^{1}H NMR spectra. Meanwhile, the carbon atoms of the ethynyl bridge linking the chromophores of **TR3** were characterized by the signals at 94.38 and 88.04 ppm in the ^{13}C NMR spectrum and by an absorption band at 2203 cm^{-1} in the IR spectrum. Compounds **TR2** and **TR3** were found to be well soluble in common organic solvents, such as chloroform, THF, methylene chloride, whereas **TR1** was moderately soluble in the above mentioned solvents.

4.1.2. Geometries and Electronic Properties
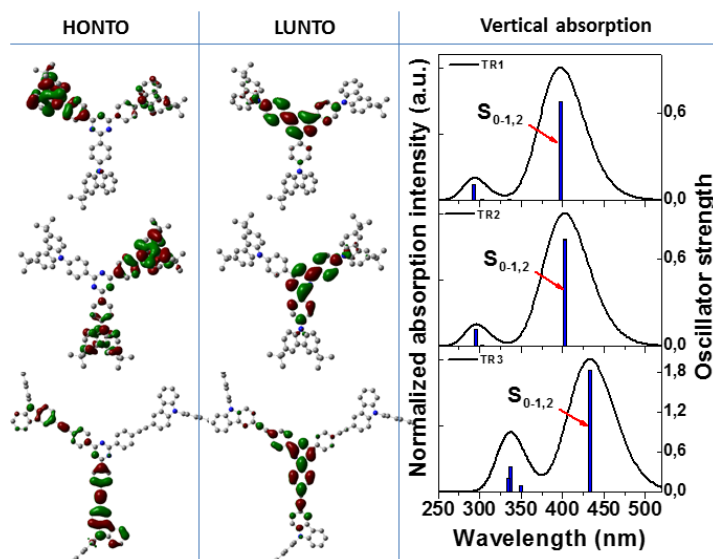
Figure 4.1.1. View on the natural transition orbitals of S_{0-1} transition and theoretical absorption spectra of **TR1–TR3** (MPW1B95/6-31G(d) in vacuum)

The DFT approach was applied for the interpretation of the structure − properties relationship of **TR1−TR3**. DFT calculations were performed by using the Gaussian suite of programs (Gaussian 09W). The geometries were optimized in the ground state by using the restricted B3LYP/6-31G(d) basis set in vacuum. Calculations show that the optimal neutral electronic ground state geometries are not planar for the molecules of **TR1** and **TR2**. The B3LYP ground state geometry shows a torsional angle of ca. 48° between the carbazole and phenylene fragments. The presence of an ethynyl linker in the molecule of **TR3** forbids rotations around it. Therefore, the mutual orientation of lateral fragments with respect to the ethynyl linker is of ca. 0.23°. Analysis of the optimized bond lengths in the electronic ground state obtained at the B3LYP theoretical level for all the three molecules revealed similar bond lengths, with the smallest values observed for **TR3**. In order to estimate the role of the D−A−D star-shaped structure on the optical transitions, the absorption spectra as well as the natural

transition orbitals (NTOs) [147] were simulated from the oscillator strengths of singlet transitions calculated by the so-called OHF method which is described in detail in literature source [42] and Chapter 4.2.2.

All the compounds under consideration can be characterized by highly allowed $S_{0-1,2}$ transitions (the oscillator strength varies in the range of 0.6−1.8), as it can be perceived from **Fig. 4.1.1**. More enhanced electron donating ability of **TR2**, as compared to **TR1**, is observed in the theoretical absorption spectra of the former (see the small bathochromic shift of **TR2** vertical transitions) due to the presence of three additional *tert*-butyl groups. However, the introduction of a rigid π-bridge between D and A moieties leads to the increased molar extinction coefficient and a three times higher oscillator strength of **TR3** compared to the parameters of C−N bonds bearing **TR1** and **TR2**. The assessment of NTOs corresponding to the S_{0-1} transition revealed that the hole is localized on phenyl carbazole moieties in **TR1** and **TR2**, whereas in the case of **TR3**, delocalization of the hole spreads through carbazole-acetylene-phenylene fragments. In the meantime, the strong electron affinity of triazine results in the localization of the negative charge within the molecular core among all the molecules. It is noteworthy that $S_{0-1,2}$ transitions are degenerate, and that NTOs of S_{0-2} transitions are of the same CT origin in all the molecules. The analysis of NTOs points that these compounds are prone to undergo ICT upon excitation, and subsequent CT state formation is expected.

4.1.3. Thermal Properties

The temperature of 5% loss of mass upon thermal degradation ($T_{dec-5\%}$) and the glass transition temperature (T_g) are important parameters of organic semiconductors since these parameters provide information on the thermal and morphological stabilities of the active layers formed from these materials. The thermal properties of the synthesized star-shaped derivatives were investigated by using a combination of DSC and TGA. All the target compounds exhibited very high thermal stability with 5% weight loss temperatures exceeding 460 °C. Compounds **TR1** and **TR2**, in which the carbazole moiety contains branched *tert*-butyl groups, exhibited superior thermal stability ($T_{dec-5\%TR1}$=528 °C and $T_{dec-5\%TR2}$=514 °C) with respect to compound **TR3** in which the carbazole moiety contains a long linear hexyl group at N-9 position ($T_{dec-5\%TR3}$=467 °C). The values of glass transition temperatures (T_g), melting temperatures (T_m), crystallization temperatures (T_{cr}) and the temperatures, at which the initial loss of mass (5%) was observed ($T_{dec-5\%}$) are summarized in **Table 4.1.4.1.**

Both **TR1** and **TR2** having one and two *tert*-butyl groups per carbazole moiety, respectively, can be transformed into the glassy state by cooling down from the melting state. They showed melting in the first heating scans but did not crystallize upon cooling. Compounds **TR1** and **TR2** exhibited glass transitions in the second DSC heating scans at 190 and 226 °C, respectively. Compound **TR3** was isolated after the synthesis as an amorphous substance. It did not show any melting or crystallization during the DSC experiment, and only exhibited glass transition at 97 °C.

4.1.4. Optical and Photophysical Properties

The UV/Vis absorption, fluorescence and phosphorescence spectra of compounds **TR1–TR3** dispersed in *Zeonex* polymer are presented in **Fig. 4.1.2.a**. the photophysical characteristics of TRZ derivatives are summarized in **Table 4.1.1**. The shape of the absorption spectra of compounds **TR1** and **TR2** are similar, and they indicate minor impact of additional *tert*-butyl groups on the optical properties of the solutions of **TR1** and **TR2**. Apparently, the carbazole linkage to triazine via a rigid ethynyl-bridge through the C-3 position of carbazole results in the effective conjugation. This was clearly observed in the absorption spectrum of **TR3**. More effective conjugation results in a broader absorption spectrum (covering the spectral area of <3.0 eV) compared to those of **TR1** and **TR2**. The absorption bands located in the range of 280–350 nm (3.54–4.42 eV) in the UV spectra of the investigated compounds can be attributed to a local excitation of carbazole moiety [167].

The phosphorescence spectra of the solid solutions of compounds **TR1– TR3** in *Zeonex* polymer matrices were recorded at 77 K (**Fig. 4.1.1.a**). All the phosphorescence spectra possess well-defined vibronic structures. Since the *tert*-butyl moiety is a relatively weak donor, no significant differences were observed in the shape and position of the phosphorescence spectra of **TR1** and **TR2**. The linkage of the donor to the acceptor through the C–N bond in **TR1** and **TR2** resulted in a higher triplet energy compared to that of the C–C bond between D and A in **TR3**. The estimated values of the triplet energy were found to be comparable for **TR1** and **TR2** (2.66–2.68 eV) and lower for **TR3** (2.38 eV).
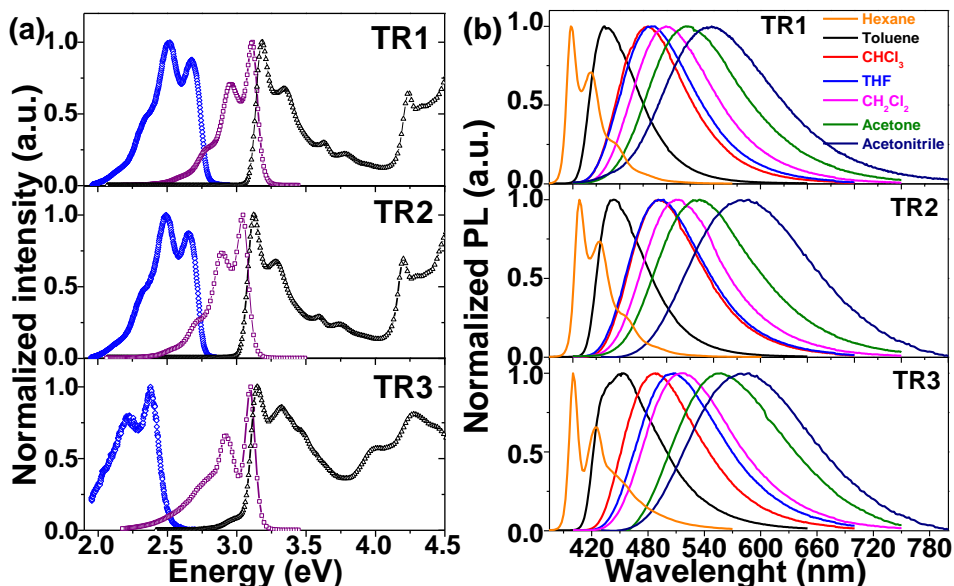

Figure 4.1.2. (a) UV/Vis (black triangles), fluorescence (violet squares) and phosphorescence (blue rhombus) spectra of **TR1–TR3** dispersed in *Zeonex* (1 wt.%) and (b) Fluorescence spectra of the solutions of **TR1–TR3** in the solvents of different polarity

The UV and PL spectra of the dilute solutions of the studied compounds at the room temperature revealed their solvent-dependent absorption and emission properties. In order to investigate the solvatochromic effect, the UV and PL spectra of the dilute solutions of the compounds in the solvents of different polarity, i.e. hexane (ε=1.88), toluene (ε=2.3), chloroform (ε=4.81), tetrahydrofuran (ε=7.6), dichloromethane (ε=8.93), acetone (ε=20.7) and acetonitrile (ε=37.5), were recorded. While the absorption of **TR1–TR3** showed only minor differences with the change of environment polarity, the PL of compounds under investigation revealed a remarkable change (see **Fig. 4.1.2.b.**). The PL spectra of the solutions of all the compounds in hexane exhibited vibronic structures consisting of two well-expressed maxima which disappeared when the spectra of the solutions were recorded by using more polar solvents. This solvatochromism is caused by the differential solvation of the ground state and the first excited state of the radiation-absorbing molecules [168]. With the increase of the solvent polarity, the PL emission spectra of all the studied compounds became broader and exhibited bathochromic shifts up to 180 nm (in the most polar acetonitrile). This observation indicates that the dipole moments of all the investigated compounds are larger in the excited state than in the ground state (i.e., $\mu_e > \mu_g$). The solvent relaxation processes can be described more precisely by employing the Lippert-Mataga equations (**4**, **5**).
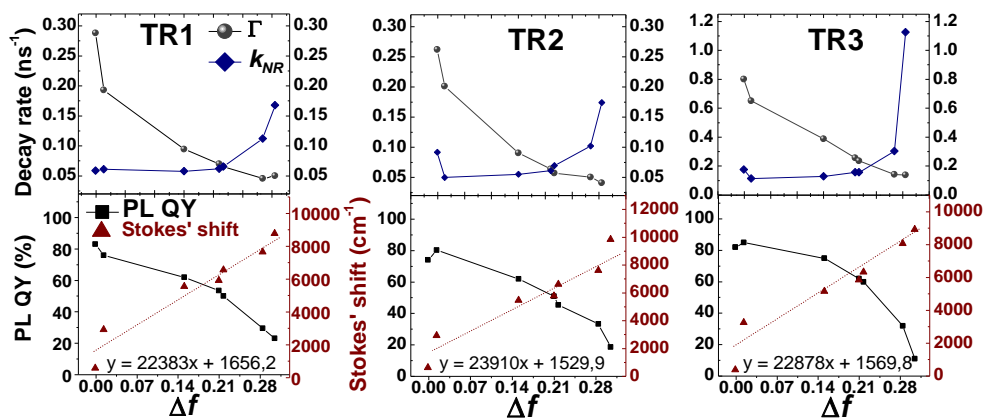
Figure 4.1.3. Dependencies of radiative (circles) and nonradiative (rhombus) decay rates, PL quantum yield (squares) and Stokes shift (triangles) on the orientation polarizability (Δf) of **TR1–TR3**. The dashed lines stand for the linear fit

Fig. 4.1.3. shows the linear relationship of the Stokes shift of the compounds under investigation on the orientation polarizability, Δf. This linearity indicates that the general solvent effects are dominant in the spectral shifts for all the compounds and suggests that all of them are strong ICT fluorophores with highly localized excited state charge separation, which was also confirmed by the simulation of NTOs (**Fig. 4.1.1.**). In the case of **TR1** and **TR3**, the Stokes shift increased from 578 cm^{-1} and 377 cm^{-1} for the solutions in hexane to 8776 cm^{-1} and 8925 cm^{-1} for the solutions in acetonitrile, respectively. The largest Stokes shift was exhibited by **TR2**; it varied from 616 cm^{-1} for the solution in hexane to

9843 cm^{-1} for the solution in acetonitrile. This observation provides further evidence of the larger excited state dipole moment of **TR2** compared to those of **TR1** and **TR3**. These results are in agreement with those reported for the other bipolar triazine-based compounds [171–173].

PL quantum yield (PL QY) provides information on the efficiency of the emission process. It is defined as the ratio of the number of emitted photons and the number of the absorbed photons [174]. The PL QYs of the solutions of the investigated compounds in the solvents of different polarity were estimated by using the integrating sphere. **Fig. 4.1.3.** presents PL QY versus Δf plot for the compounds under investigation. With the increase of the solvent orientation polarizability (Δf), more time for a typical ICT fluorophore is required to reach its relaxed excited state, which enhances the nonradiative processes and leads to higher energy losses. Therefore, the PL QY is expected to decrease. Indeed, the PL QY of the solutions of triazine derivatives **TR1−TR3** decreased with the increase of the solvent polarity. A PL QY of 83% was observed for **TR1** solution in nonpolar hexane, whereas the lowest value of 23% was recorded for the solution in acetonitrile. Compounds **TR2** and **TR3** demonstrated similar tendencies. The PL efficiency of the solid films of **TR1** and **TR2** were found to be 33% and 29%, respectively, whereas that of the film of **TR3** was 20%.

Table 4.1.1. Thermal, photophysical, electrochemical and photoelectrical characteristics of **TR1–TR3**

Compound	T_g, •C^a	T_M, •C^a	$T_{dec-5\%}$, •C^b	E_g^{opt}, eV^c	E_T, eV^d	IP^{CV}, eV^e	EA^{CV}, eV^e	μ, $cm^2/(V \cdot s)^f$
TR1	190	344	528	3.09	2.68	5.49	2.86	$2 \cdot 10^{-3}$
TR2	226	448	514	3.03	2.66	5.68	2.83	$7.5 \cdot 10^{-3}$
TR3	97	−	467	2.86	2.38	5.37	−	$3 \cdot 10^{-3}$

[a]Determined by DSC; [b]Determined by TGA; [c]Determined from UV/Vis spectra; [d]Determined from phosphorescence spectra; [e]Determined by CV in CH_2Cl_2 solutions. IP^{CV} estimated from the onset oxidation potential by using the relationship $IP_{CV}=|e|(4.8+E_{ox}^{onset})$. EA^{CV} was estimated from the onset reduction potential by using relationship $EA_{CV}=|e|(4.8+E_{red}^{onset})$. [f]Mobility value at $6.4 \cdot 10^5$ V/cm field strength.

For additional information on the dynamics of the $S_1 \rightarrow S_o$ emission, the PL lifetimes of the dilute solutions of compounds **TR1−TR3** in the solvents of different polarity were estimated. With the increase of the solvent polarity from that of hexane to that of dichloromethane, the solutions of all the compounds showed increasing values of fluorescence lifetime (τ), while τ of the solutions in acetone and acetonitrile was found to be by 1−3 ns shorter if compared to those observed for the solutions in dichloromethane. In general, τ of the solutions of **TR3** was found to be 2.7−3.5 times shorter than those of **TR1** and **TR2**. The shorter fluorescence lifetimes and the higher PL QYs of the solutions of **TR3** compared to those of solutions of **TR1** and **TR2** are in agreement with the significantly higher (to be more specific, 2.7−3.0 times higher) oscillator strength of the transition $S_0 \rightarrow S_1$ observed in the theoretical UV spectra of the compounds under investigation.

In order to evaluate the contributions of radiative and nonradiative decay processes in the solutions of the researched compounds, radiative and nonradiative decay rates, Γ and k_{NR}, respectively, were estimated [58]. Γ decreased exponentially with the increase of the solvent polarity for the solutions of all the compounds (see **Fig. 4.1.3**). For the solutions of **TR3**, the values of Γ were found to be ca. 3 times higher than those of solutions **TR1** and **TR2**. This observation is consistent with the larger oscillator strength of the $S_0{\rightarrow}S_1$ transition of **TR3**. The rate of k_{NR} increased with the increase of the solvent polarity thus indicating the enhancement of the nonradiative processes. This observation is consistent with the decrease of PL QY.

4.1.5. Electrochemical Properties

The electrochemical properties of **TR1−TR3** were studied by employing CV in order to elucidate the electronic energy levels determining the energy and electron transfer processes, as well as the reversibility of the redox processes. **Fig. 4.1.4.** illustrates the CV graphs of compounds **TR1−TR3**. Only **TR2** showed reversible oxidation at 1.10 V during the CV experiment. Since compounds **TR1** and **TR3** contain unsubstituted C−6 positions of carbazole moieties, they showed irreversible oxidation processes at 0.89 V and 0.77 V for **TR1** and **TR3**, respectively. Similar observations were reported earlier [175,176]. For such compounds, the growing peak of current during the CV experiment and the resulting formation as well as the growth of thin films on the working electrode demonstrate the occurrence of oxidation-induced electropolymerization [177,178]. Compounds **TR1** and **TR2**, in which the carbazole moiety is linked to the triazine core through N−9 position of carbazole moiety, demonstrated reversible reduction at −1.74 V and −1.77 V, respectively. This observation shows that in these conditions a stable radical anion is formed on the triphenyltriazine moiety [179]. **TR3** did not exhibit any notable reduction peak during the CV experiments.

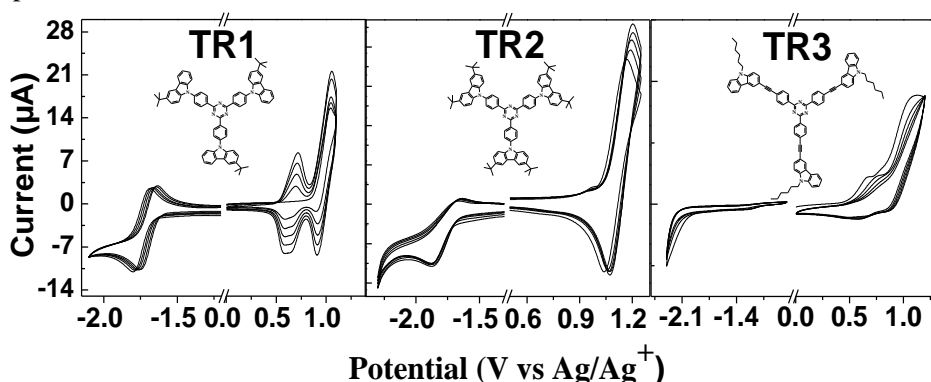**Figure 4.1.4**. Cyclic voltammetry scans of dilute 1 µg/ml solutions of compounds **TR1–TR3**

The ionization potential (IP^{CV}) and electron affinity (EA^{CV}) values of the synthesized compounds were estimated by using ferrocene/ferrocenium as the

standard redox system. The values of IP^{CV} and EA^{CV} are summarized in **Table 4.1.1.** Compound **TR2** was found to possess the highest IP^{CV} value of 5.68 eV, while compound **TR3** demonstrated the highest electron donating ability showing the value of IP^{CV} of 5.37 eV.

4.1.6. Charge-Transporting Properties

Xerographic time-of-flight (XTOF) measurements were used with the intention to characterize the charge-transporting properties of the synthesized compounds. The investigations were carried out for the layers of **TR1−TR3** coated on aluminum-plated glasses by employing the solution processing technique. Dispersive hole-transport was observed in the layers of **TR1−TR3** (**Fig 4.1.5.a.**). The hole-transit times (t_t) needed for the estimation of hole mobilities were established from the intersection points of two asymptotes of the double-logarithmic plots. The representative hole-drift mobility dependency on the electric field for the neat film of **TR2** is shown in **Fig. 4.1.5.b**. Such dependence is commonly observed in organic charge transporting materials in amorphous state due to the disorder. The data of the hole mobility of the neat films of compounds **TR1−TR3** is presented in **Table 4.1.1**. The highest hole mobility value is observed for compound **TR2**. It approached the magnitude of 10^{-2} cm^2 V^{-1} s^{-1} at high electric fields.
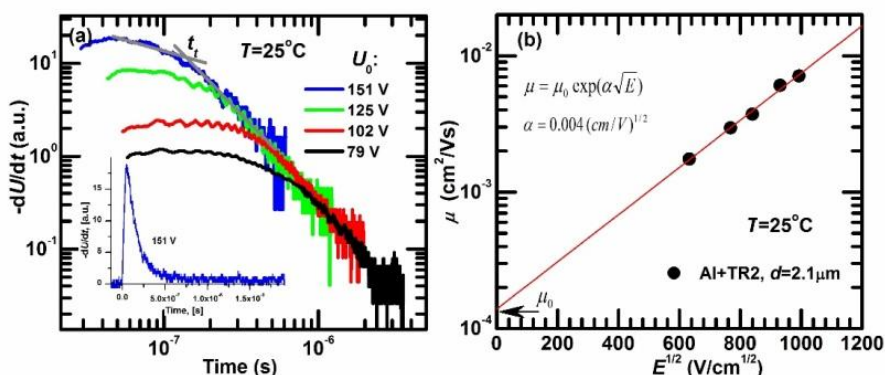
Figure 4.1.5. (a) XTOF transients for the neat film of **TR2**. Arrow marks indicate the transit time of holes at the respective surface voltage; (b) Electric field dependencies of hole-drift mobilities of the amorphous layer of **TR2**

4.1.7. Electroluminescent Properties

Compounds **TR2** and **TR3** were tested as light emitting materials in the two-layer solution-processed OLED structures based on the host-guest system. The blend of poly N-vinyl carbazole (PVK) and 2-(4-tert-butylphenyl)-5-(4-biphenylyl)-1,3,4-oxadiazole (PBD) was used as the host, whereas **TR2** and **TR3** were employed as emitting guest materials. PVK is widely known as a hole transporting material [180]. In addition, it possesses a large exciton lifetime [181,182]. In order to enable the host system to transport both types of charge carriers, i.e., electrons and holes, PBD was mixed with PVK [183,184]. The

energy levels of PVK and PBD are suitable for efficient energy transfer to light emitting dopants **TR2** and **TR3** in it (**Fig.4.1.6.**).
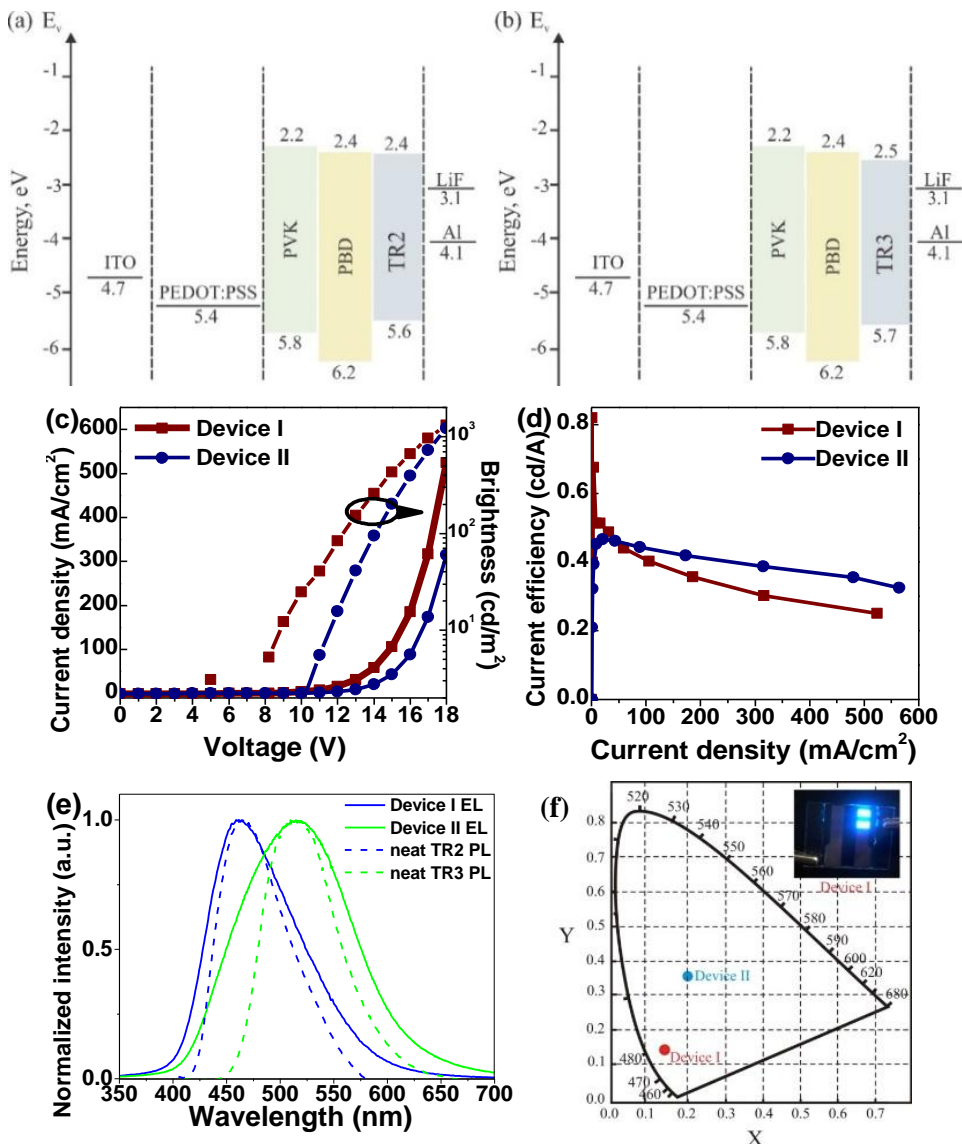
Figure 4.1.6. Energy diagrams of devices I (a) and II (b) and the current density-voltage and luminance-voltage characteristics (c), current efficiency – current density characteristics (d), EL and PL spectra of devices I and II, and neat films of **TR2** and **TR3** (e) as well as the CIE color diagram (f) and the image of operating device II (inset)

Electroluminescence (EL) spectra and other characteristics of fabricated devices I and II are presented in **Fig. 4.1.6**. The characteristics of OLEDs are summarized in **Table 4.1.2**. The EL intensity maxima of devices I and II were observed at 463 nm and 515 nm, respectively. Since pure PVK:PBD based devices showed their emission maxima at 433 nm [185], and the EL emission

maxima of devices I and II were observed at the same wavelengths as the PL emission maxima of the neat films of **TR2** or **TR3** (**Fig. 4.1.6.e**), we can conclude that effective excitation energy transfer from the host matrices to the guests takes place in the devices. The turn-on voltage (V_{on}) of device I was observed at 8 V for the electroluminescence of 5.24 cd/m^2. In case of device II, the V_{on} was observed at 9.5 V for EL of 1.5 cd/m^2. The brightness maxima of 1342 and 1221 cd/m^2 were observed at 18 V for devices I and II, respectively, with the maxima of the current efficiency being detected in the range of 0.1–0.55 cd/A. The CIE chromaticity coordinates of devices I and II were found to correspond to the blue (0.15; 0.13) and the green emission color (0.21; 0.33), respectively (**Fig. 4.1.6.f.**). The increase of the bias led to the reduction of the device brightness followed by its structural degradation. It is known that V_{on}, brightness and the current efficiency of OLEDs are determined by the thickness of the active layer, the injection barriers, and the balance of the charge carriers in the device [186–189]. The thickness of the active layer in our OLEDs was 70 nm, which is typical for this kind of devices. OLEDs fabricated in this work do not contain additional hole-transporting or electron transporting layers in addition to PEDOT:PSS. Such additional layers could improve the characteristics of the devices and reduce V_{on}. In addition, the charge carrier balance in the polymer host-guest matrix devices depends on the amount of the light emitting dopant in the matrix blend [75,190,191]. The optimization of the concentration of **TR2** and **TR3** in the polymer matrix and the application of the additional hole- and/or electron-transporting layers would hopefully provide the possibility of improving the device performance.

Table 4.1.2. EL performances of multi-layered devices with synthesized emitters. Device: ITO/PEDOT:PSS/PVK:PBD (40 wt%):guest(3 wt%)/LiF/Al.

Device	V_{on}, V[a]	EL_{max}, nm[b]	Brightness, cd/m2[c]	C.E., cd/A[d]	CIE, (x,y)[e]
I (guest TR2)	8	463	1342	0.51	(0.15; 0.13)
II (guest TR3)	9.5	515	1221	0.46	(0.21; 0.33)

[a]Turn on voltage; [b]Electroluminescence maxima; [c]Brightness maxima at 18 V; [d]Current efficiency; [e]CIE color coordinates.

To conclude, we synthesized and characterized three new star-shaped triazine and carbazole hybrid derivatives and applied two of them as emitters in fluorescent OLEDs. A combination of thermally stable chromophores into final molecules led to the achievement of superior thermal stability possessing compounds. By comparing the linking pattern between the donor and the acceptor, we found that the connection of carbazole to triazine via the N–9 position of carbazole leads to a higher triplet energy of the resulting compound, while the D–A connection via a rigid ethynyl bridge and the C–3 bond of carbazole leads to significantly enhanced oscillator strength, thus leading to a highly radiative S_1 state of the resulting compound.

4.2. *Meta*-Conjugated Derivative of 1,3,5-Triazine and Carbazole as Effective Delayed Fluorescence Emitter

The longest lifetime of blue-emitting TADF OLEDs was registered when triazine-carbazole based TADF emitters were used [83,84,192]. Following the advantages provided by the connection of D and A units via the C–N bond, and in the meantime maintaining the solubility, glass-forming ability, as well as the thermal and electrochemical stability of the resulting compound, we decided to synthesize a *meta*-conjugated isomer of **TR2**, *2,4,6-tris(3-(3,6-di-tert-butyl-9H-carbazol-9-yl)phenyl)-1,3,5-triazine* (***m*TR2**) and investigate the delayed emission properties in these two isomeric derivatives [193].

4.2.1. Synthesis
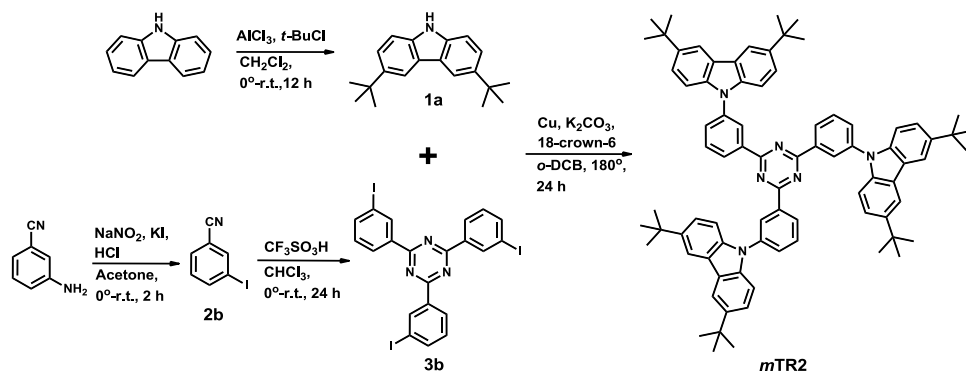
Scheme 4.2.1. Synthetic pathways of ***m*TR2**

Compound ***m*TR2** was synthesized by employing the Ullmann's coupling reaction by adhering to the same methodology as we used for **TR2**. Similarly to the previously described **TR1**, all the characteristic signals of certain molecular fragments of ***m*TR2** were found in both ^{1}H and ^{13}C NMR spectra. The characteristic signals of the carbon atoms of the triazine heterocycle were found at 171.4 ppm in ^{13}C NMR spectra, while the characteristic singlet signal corresponding to the protons of the methyl group of the *tert*-butyl moiety was found at 1.50 ppm in ^{1}H NMR spectra.

4.2.2. Geometries and Electronic Properties

The molecular geometries of the compounds in the ground state were optimized by using DFT calculations with B3LYP/6-31G (vacuum) level of theory. The strong electron affinity of 1,3,5-triazine affects the adjacent phenyl rings in C–2, C–4 and C–6 positions of the triazine unit. This effect predetermines the planar conformation of 2,4,6-triphenyl-1,3,5-triazine moiety. The carbazole units linked to phenyl rings via C–N bonds are twisted by ca. 48° in **TR2** and by 51° in ***m*TR2**.

For the CT compounds, it is necessary to understand the origin of the first excited states since the origin of these states determines the overall photophysical behavior of the compound. The interpretation of only HOMO and LUMO distribution is not informative enough, since it represents the one-electron wave

function. Moreover, in the case of CT compounds, the frequently used B3LYP functional usually underestimates the energy of electronic states [194,195]. In order to assess these issues and correctly interpret the experimental results, we employed the Optimal Hartree-Fock (OHF) method developed by Huang et al. [42]. In this work, its authors revealed the importance and strength of the relationship between the amount of charge transferred in the excitation process and the optimal HF% in the exchange-correlation (XC) functional. The amount of charge (q) transferred from the donor to the acceptor is calculated by using equations (**6,7**). Since it was shown [42,80] that q calculated from the weighted averages of each transition is close to that calculated from the HOMO→LUMO transition, for convenience, the CT amount in the HOMO→LUMO transition is used to approximate that in S_{0-1} transition. Finally, the optimal HF% is calculated by using relation (**8**).
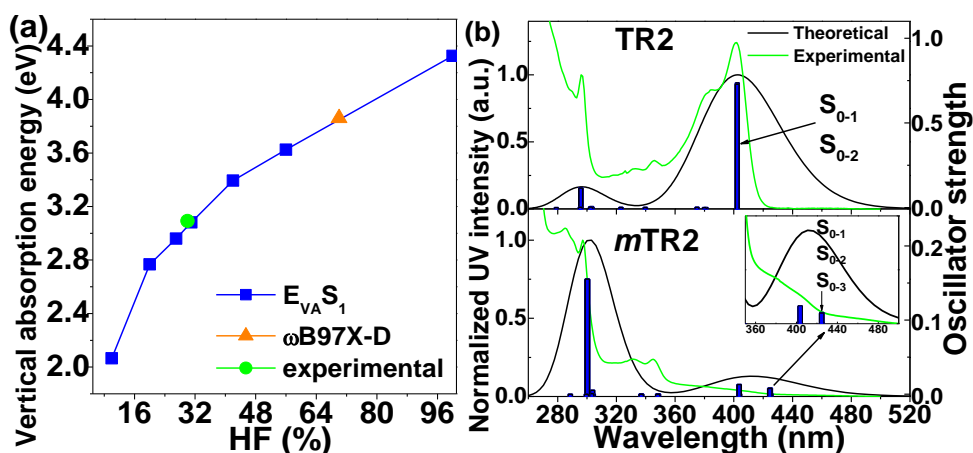
Figure 4.2.1. (a) Vertical absorption energy dependence on the amount of HF% of **TR2** and (b) theoretical (black curves, MPW1B95 6–31G in vacuum) and experimental absorption spectra (green curves, solid solution in *Zeonex*) of **TR2** and **mTR2**. The inset represents the zoomed LEB of **mTR2**. The primary transitions are depicted

On the grounds of the sensitivity of S_{0-1} transition energy on the HF amount being obvious, as it was demonstrated in **Fig. 4.2.1.a.**, here we show the importance of choosing the pertinent functional in order to match the experimental results with the theoretically obtained ones. It should be noted that range-separated functionals (in our case, it was ωB97X-D) tend to overestimate the excitation energy of TADF compounds [42,80], which was also detected in our case (**Fig. 4.2.1.a.**, the orange triangle). Apparently, the CT excitations in **TR2** and **mTR2** are of a shorter range. According to equation (3), the optimal Hartree-Fock exchange energy percentage (% HF) for **TR2** was found to be 31%, and that for **mTR2** was estimated to be 35%. Consequently, the vertical transitions, as well as the natural transition orbitals (NTOs) [147] were simulated with MPW1B95 [143] (31% HF) functional. **Fig. 4.2.1.b** presents the theoretical and experimental (1 wt.% solid solutions in cyclo-olefin polymer *Zeonex*) absorption spectra of the compounds under investigation.

Evidently, careful selection of the most appropriate functional provided the desired results. The first transitions of both compounds coincide with the maxima of the lowest energy bands (LEBs) of the experimental spectra of the solid solutions in *Zeonex*. *Para*-conjugation in **TR2** is responsible for the considerably higher oscillator strength (0.73) of the first electronic transition compared to that of ***m*TR2** with *meta*-conjugation (0.008). A similar trend can be observed in the experimentally obtained spectra: LEB of **TR2** (360–440 nm) is of higher intensity than that of ***m*TR2** (**Fig. 4.2.1.b**).
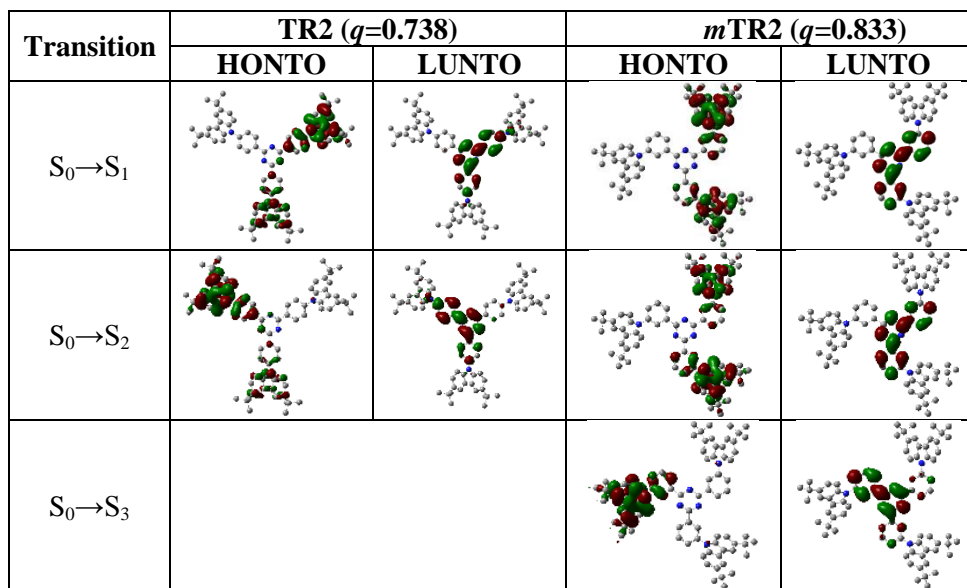
Transition	TR2 (q=0.738)		*m*TR2 (q=0.833)	
	HONTO	LUNTO	HONTO	LUNTO
$S_0{\rightarrow}S_1$				
$S_0{\rightarrow}S_2$				
$S_0{\rightarrow}S_3$				

Figure 4.2.2. Natural transition orbitals of **TR2** and ***m*TR2**

In order to identify the origin of the initial electronic transitions ($S_0{\rightarrow}S_{1,2}$ for **TR2** and $S_0{\rightarrow}S_{1\text{-}3}$ for ***m*TR2**), one may find it difficult to analyze the overall impact of major excitations, especially when a singular transition consists from multiple excitations [194], which was found in our case as well. Due to this discovery, we accessed the NTOs (**Fig. 4.2.2.**) of the transitions $S_0{\rightarrow}S_{1\text{-}3}$ of the compounds under investigation. From the analysis of NTOs, we can conclude that the origin of all of these transitions is of CT character since the hole is localized on the phenylcarbazole moiety, whereas electron injection mainly affects the diphenyltriazine moiety. It is worth mentioning that *meta*-linkage is responsible for the larger excited state charge separation (q) in ***m*TR2**. The CT nature of $S_0{\rightarrow}S_{1\text{-}3}$ transitions in these compounds is consistent with similar observations for other triazine-carbazole hybrid materials [83,89,192,196].

4.2.3. Thermal and Electrochemical Properties

Bulky *tert*-butyl groups were introduced with the objective to block the active 3rd and 6th positions of the carbazole moiety as it is known that *tert*-butyl groups prevent π-π stacking, ensure electrochemical stability and desirable thermal properties as well as increased solubility. Indeed, the investigation of

thermal characteristics by a combination of DSC and TGA revealed high thermal stability of both compounds. The 5% weight loss temperature of **mTR2** ($T_{dec-5\%}$) is as high as 447 °C. The glass transition temperatures of both isomers are similar (226 °C and 222 °C for **TR2** and **mTR2**, respectively), whereas **mTR2** was found to possess a 60 °C lower melting point (388 °C).

Table 4.2.1. Thermal, photophysical and electrochemical characteristics of **TR2** and **mTR2**

Compound	T_g, °C[a]	T_M, °C[a]	$T_{dec-5\%}$, °C[b]	E_g^{opt}, eV^c	E_T, eV^d	IP^{CV}, eV^e	EA^{CV}, eV^e
mTR2	222	388	447	2.53	2.77	5.65	2.78
TR2	226	448	514	3.03	2.66	5.68	2.83

[a]Determined by DSC; [b]Determined by TGA; [c]Determined from UV/Vis spectra; [d]Determined from phosphorescence spectra; [e]Determined by CV in CH_2Cl_2 solutions. IP^{CV} estimated from the onset oxidation potential by using relationship $IP_{CV}=|e|(4.8+E_{ox}^{onset})$. EA^{CV} estimated from the onset reduction potential by using relationship $EA_{CV}=|e|(4.8+E_{red}^{onset})$.
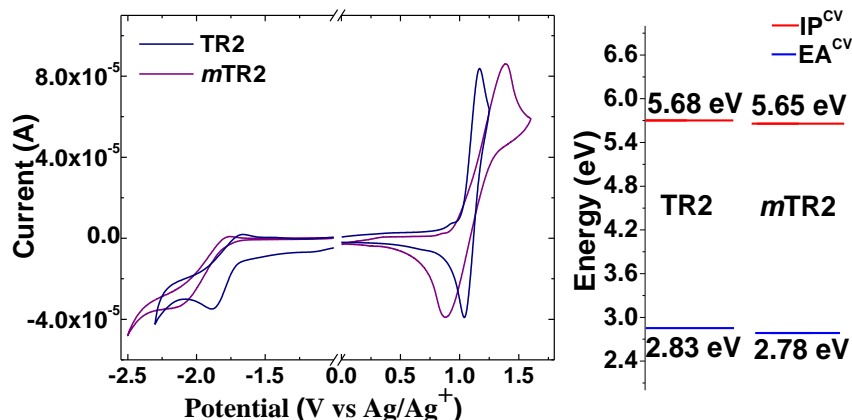
Figure 4.2.3. Cyclic voltammetry scans of dilute 1 µg/ml solutions of compounds **TR2** and **mTR2** and the energetic diagram of energetic levels

For successful production of an OLED, it is required to estimate the energy levels of the emitters in order to fit them well in the stack along with the host. For this reason, the CV method was employed. During CV experiments, both compounds showed bipolar behavior. By applying positive or negative voltage, it was possible to oxidize or reduce the compounds reversibly (**Fig. 4.2.3.**). The ionization potential and the electron affinity values are presented in **Fig. 4.2.3**.

4.2.4. Steady-State Photophysics

One of the most important parameters of TADF compounds is the energy difference between the first singlet and triplet excited states (ΔE_{ST}). Negligible ΔE_{ST} facilitates the rate of reverse intersystem crossing (rISC) thus enhancing the efficiency of TADF [43,48,53,197,198]. Estimation of ΔE_{ST} is complicated, and the obtained results must be taken with caution. In D–A systems, there are two singlet states (local excitation ^1LE and charge-transfer ^1CT) and at least two triplet

states (^{3}LE and ^{3}CT) [58] involved in the emission mechanisms. Since ΔE_{ST} is a numerical value, it is necessary to emphasize between which of the above mentioned states this energy difference was estimated. There are numerous articles including reviews [199] where only the values of ΔE_{ST} are reported but there is no clear indication in which conditions they were obtained and what energy difference between which states ΔE_{ST} reflects. In addition, the ^{1}CT state undergoes dynamic relaxation in time thus making it challenging to define the exact energy level of this state [53]. Being aware of these issues, we found it appropriate to report the values of ΔE_{ST} only when we can clearly define at which conditions they were estimated.
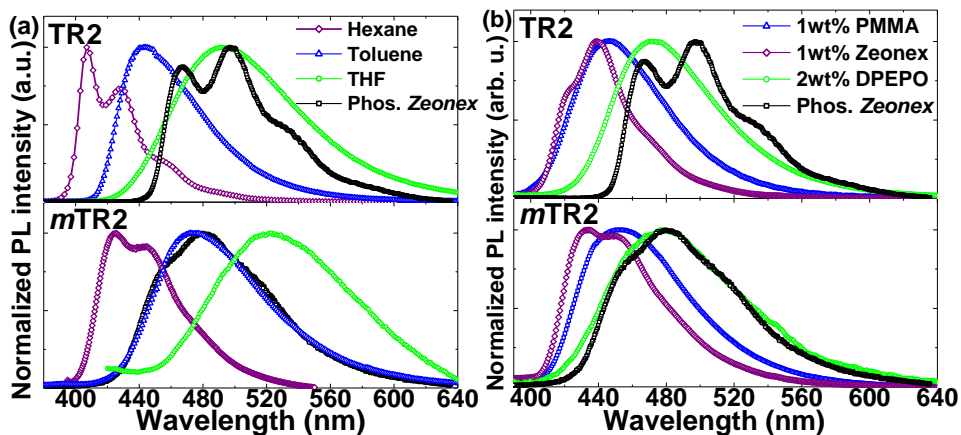

Figure 4.2.4. Steady-state photoluminescence spectra of **TR2** and **mTR2**: (a) of the solutions in solvents of different polarity and (b) of the compounds dispersed in two different polymer hosts and of evaporated emission layer with the host DPEPO along with PLQY values in ambient and degassed atmosphere. Phosphorescence spectra assessed from solid solutions (1 wt.%) in *Zeonex* at 77 K are also depicted

The ^{1}CT singlet state is known to be sensitive to the polarity of the surrounding media [58], however, it is the state through which TADF may occur. One simple way of determining to what extent it is possible to tune the energy of the ^{1}CT state is to record the steady-state photoluminescence (PL) spectra in several solvents of different polarity. This experiment gives insight into the ways how a TADF emitter may act when doped into a host of certain polarity. The most appropriate way to estimate ΔE_{ST} is to measure the levels of S_1 and T_1 in the blend of the guest and the host [53]. The emissive triplet state is usually ^{3}LE which is not sensitive to the polarity of the surrounding media and the temperature. Therefore it is easier to compare the T_1 level estimated in one type of media at a low temperature with the results of steady-state photoluminescence measurements performed in the media of different polarity. In such a way, one can find out which medium would lead to the minimization of ΔE_{ST}. This is illustrated in **Fig. 4.2.4.a**.

For solutions in the most non-polar media (hexane), the PL spectra of both compounds possess a well-resolved vibronic structure indicating that their ^{1}LE state is of the origin of emission. A small increase of solvent polarity (toluene)

facilitates the formation of the [1]CT state since a broad and structureless red-shifted PL band appears. A further increase in polarity (THF) results in even more considerable red-shifting of the PL spectra. It should be noted that the PL spectra of the solutions of *m*TR2 were found to be bathochromically shifted if compared to those of the solutions of **TR2**. This observation, although being unexpected (as, generally, the PL spectra of *meta*-isomers appear to be blue-shifted in comparison to those of their *para*-analogues [58,200]), indicates that, in our case, *m*TR2 appears to possess a stronger CT character than its *para*-analogue **TR2**.

Fig. 4.2.4.b presents the fluorescence spectra of **TR2** and *m*TR2 dispersed in polymers of different polarity. It should be noted that **TR2** demonstrated higher values of PLQY, which is consistent with the higher oscillator strength of the degenerate excitations constituting the lowest energy band of **TR2** compared to that of *m*TR2. Furthermore, the PL spectra of the evaporated layers of the emitters doped into the host DPEPO, which corresponds to the more polar medium (DPEPO polarity is somewhere between that of toluene and THF), were accessed. Interestingly, the steady-state PL spectrum of the dispersion of *m*TR2 in DPEPO almost entirely overlaps with the phosphorescence spectrum (**Fig. 4.2.4.b.**), whereas in the case of **TR2**, due to its weaker CT character and lower E_T, DPEPO polarity seems to be insufficient to achieve a complete overlap of singlet and triplet emissions – thus reduced TADF efficiency is expected. In order to evaluate the minimization of ΔE_{ST}, the PLQYs of the evaporated layers were measured in ambient and degassed atmospheres. The increase of PLQY for *m*TR2 (from 0.05 to 0.25) was found to be 4-fold higher than that of **TR2** (from 0.33 to 0.35). The above outlined results indicate that the contribution of the delayed component to the total emission is more prominent in *m*TR2, which points out that DPEPO may be a suitable matrix to host *m*TR2.
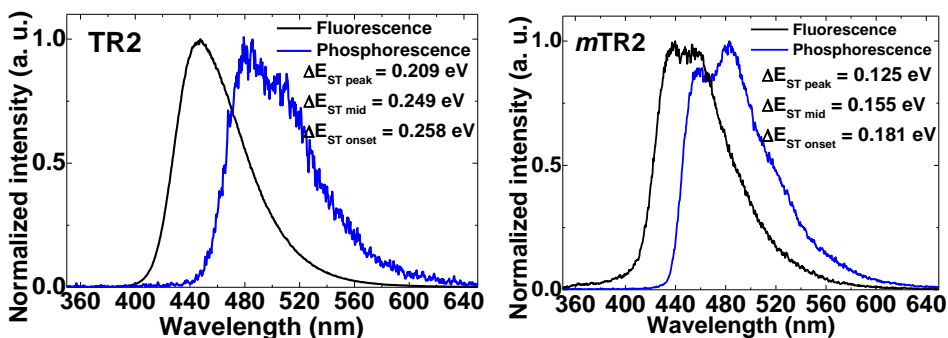
Figure 4.2.5. Fluorescence (black) and phosphorescence (blue) spectra. The singlet-triplet energy gap calculated from the position of 0-0 vibronic peak ($\Delta E_{ST\ peak}$), from mid ($\Delta E_{ST\ mid}$) and from the onsets of the spectra ($\Delta E_{ST\ onset}$)

In order to minimize ΔE_{ST} in solid solutions and to perform temperature-resolved measurements, we chose poly(methyl methacrylate) (PMMA) as a host due to its slightly polar nature, which in principle should influence only the position of the [1]CT energy level of both compounds. At lower temperatures, phosphorescence is observed for both compounds, which is evident by a shifted emission spectrum (**Fig. 4.2.5**). The recorded phosphorescence spectra at 11 °K

offers some insight into the energy gap ΔE_{ST} which can be evaluated from PL spectra peaks. The ΔE_{ST} values calculated this way were 0.125 eV and 0.209 eV for *m*TR2 and TR2, respectively.

4.2.5. Time-Resolved Measurements

Figure 4.2.6. (a) Decay kinetics of prompt and delayed fluorescence and (b) prompt and delayed fluorescence intensity versus excitation fluency for the solid solutions of **TR2** and *m*TR2 in PMMA. The samples were excited in a degassed chamber. The data was fitted with the power law function

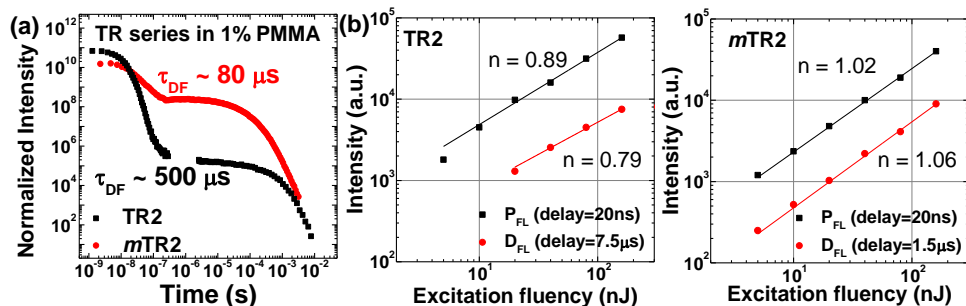The decay kinetics for both compounds molecularly dispersed in PMMA exhibits a fast prompt and a slower delayed fluorescence (DF) component with the lifetime values of 500 µs and 80 µs for **TR2** and *m*TR2, respectively. In order to confirm that the delayed fluorescence is due to rISC, the luminescence intensities of prompt and delayed fluorescence were measured at room temperature in deoxygenated environment as a function of excitation power (**Fig. 4.2.6.b.**). The same power law statistics at low energy excitations for prompt and delayed fluorescence (linear singular dependence) suggests that delayed fluorescence is not a result of triplet-triplet annihilation, but instead is a thermally activated process [59]. The emission decay kinetics of both samples shows that DF is 3 orders of magnitude more intense for *m*TR2 (**Fig. 4.2.6.a.**).
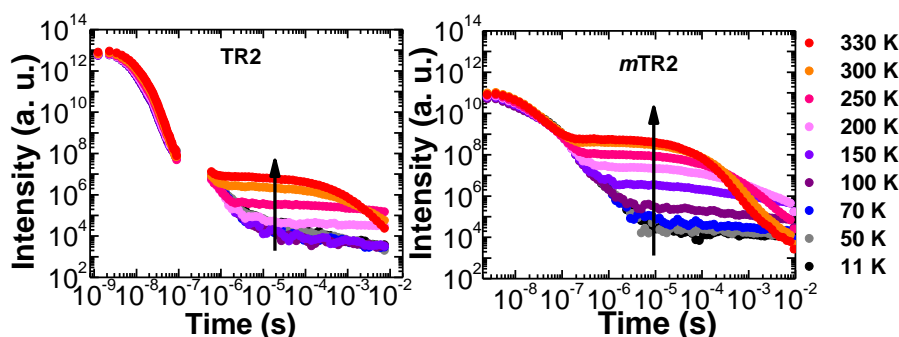
Figure 4.2.7. (a) Photoluminescence decay dynamics recorded at different temperatures and (b) delayed fluorescence spectra taken at 10 µs delay time of the solid solutions of **TR2** and *m*TR2 in PMMA at different temperatures

In order to evaluate the efficiency of the thermally activated process and the activation energy, the decay kinetics of the studied compounds was investigated for solid PMMA solutions in deoxygenated environment at different

temperatures. **Fig. 4.2.7.** shows photoluminescence decay dynamics of the solid solutions of **TR2** and **mTR2** in PMMA recorded at different temperatures. A significant shortening of the DF lifetime with the increasing temperature is observed, which is due to the increasing rate of rISC, a thermally activated process. The phosphorescence decay transient appears as a straight line due to its lifetime being much longer than the maximum available delay time, which is 10 ms. Whereas the prompt fluorescence is more intense for **TR2**, TADF is more prominent and observed at lower temperatures for **mTR2**. In order to illustrate this phenomenon, the ratio of the integrated DF/PF versus temperature is plotted for both compounds. At 330 °K, this ratio reaches the values of 0.06 and 27 for **TR2** and **mTR2**, respectively, which indicates that TADF is the dominating PL decay process for the *meta*-linked **mTR2** (**Fig. 4.2.8.a.**).
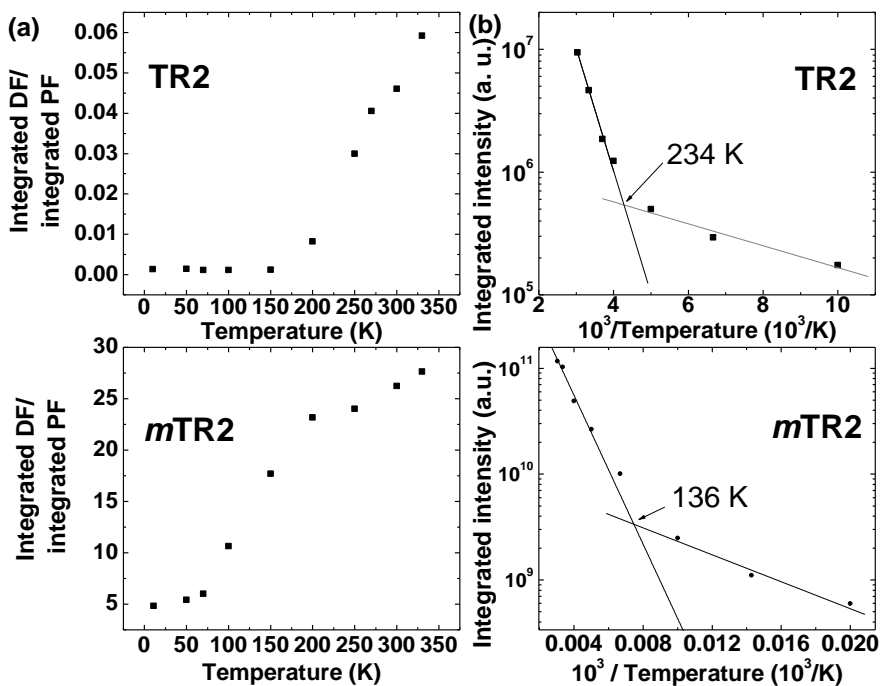
Figure 4.2.8. (a) The ratio of integrated intensities of delayed and prompt fluorescence and (b) Arrhenius type plot of temperature dependence of the integrated intensity of delayed fluorescence for the solid solutions of **TR2** and **mTR2** in PMMA. Activation energy EA was calculated from the exponential fit of the first 4 data points

The activation energies were calculated by fitting the Arrhenius plot with the exponential function as shown in **Fig. 4.2.8.b**. The resulting activation energies of 0.199 eV and 0.070 eV for **TR2** and **mTR2**, respectively, are in good agreement with ΔE_{ST} values estimated from low-temperature fluorescence and phosphorescence spectra.

4.2.6. OLED Characteristics

Since **mTR2** showed much more efficient rISC and more prominent delayed fluorescence, it was chosen as a viable emitter for the fabrication of TADF OLED. The device structure was [ITO/m-MTDATA (10 nm)/NPB (15 nm)/mCP (10 nm)/5wt%-*m*TR2:DPEPO (20 nm)/TPBi (45 nm)/LiF (0.8 nm)/Al (100 nm)], where m-MTDATA (4,4′,4″-tris[phenyl(m-tolyl)amino]triphenylamine), NPB (N,N′-di(1-naphthyl)-N,N′-diphenyl-(1,1′-biphenyl)-4,4′-diamine), mCP (1,3-di(9H-carbazol-9-yl)benzene) were used as the hole injection and transport, hole transport, hole transport and exciton blocking layers, respectively. TPBi (2,2',2"-(1,3,5-benzinetriyl)-tris(1-phenyl-1-H-benzimidazole)) and LiF were used as the electron transport and injection layers, respectively. The energy level diagram is shown in **Fig. 4.2.9.a**. Due to the electron transporting properties of the host DPEPO (bis(2-(diphenylphosphino)phenyl)ether oxide), the recombination zone is held to be at and near the interface of mCP and DPEPO. Thus mCP plays the role of exciton blocking as its triplet energy (E_T=2.9 eV) is higher than that of **mTR2** (E_T=2.7 eV). The current density, the luminance versus voltage as well as EQE and luminous efficacy versus current density characteristics are shown in **Fig. 4.2.9.b**, **c**.
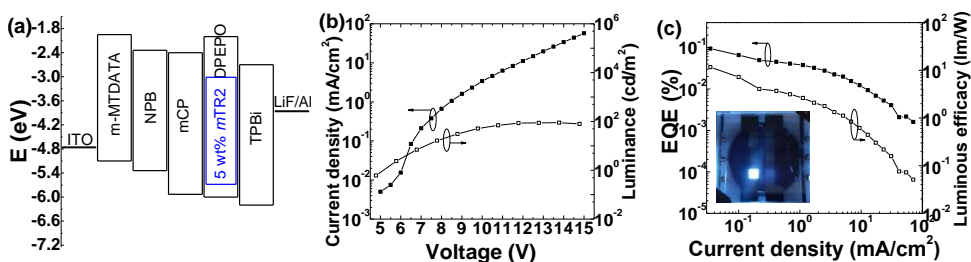
Figure 4.2.9. Energy level diagram (a) and characteristics (b,c) of OLED

The device displayed EL spectra similar to the corresponding PL spectra of **mTR2**, which confirms that EL emission was generated from **mTR2** via the same radiative decay process as in PL. The EL emission spectrum peak was found to be at 475 nm, and *Commission Internationale de l'Éclairage* (CIE) color coordinates were calculated to be (0.16; 0.23), which corresponds to a sky-blue emission color. The turn-on voltage of the OLED was found to be in the range of 5–6 V. The maximal obtained EQE for the device was 9.5%. However, the device showed severe roll-off, which is likely due to the annihilation processes in the emitter. The **mTR2** PL efficiency in DPEPO was found to be 25%, which implies a prominent nonradiative exciton relaxation path. This severely impacts the device performance at higher current densities.

To conclude, in this chapter we showed that the widely used B3LYP functional is inappropriate to correctly interpret the nature and energy of the lowest energy bands of D–A compounds. The calculation of the CT amount (q) and the subsequent optimal Hartree-Fock exchange energy percentage represent a quick and low-computational-cost methodology suitable for the selection of an appropriate functional for the TD–DFT calculations. The strategy of maintaining

the star-shaped molecular architecture and the usage of shielded carbazole units yielded a thermally and electrochemically stable blue emitter. A comparative study of *m*TR2 and TR2 revealed the potential of a *meta*-linking pattern to be a successful strategy when seeking to achieve efficient TADF in the resulting compound.

4.3. Influence of Chromophores Connection Pattern on the Properties of Bipolar Carbazole-Benzonitrile Derivatives

By following the results described in the former chapters, we retain the C–N linkage between D–A units as the major pattern. Hence, the influence of *para*- and *meta*-linkage, as well as an additional phenyl spacer, on the properties is studied. In this way, we designed, synthesized and characterized 5 new bipolar carbazole-benzonitrile materials, in which the donor and acceptor units are separated by using the required distance (presence/absence of a spacer) and by employing a different mode of the conjugation path (para- or meta-linkage).

4.3.1. Synthesis
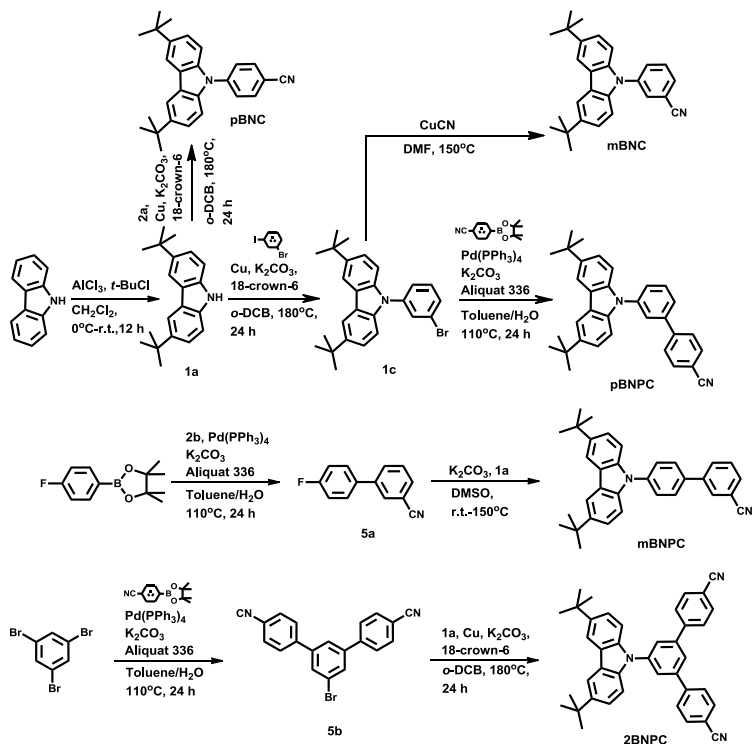
Scheme 4.3.1. Synthetic routes towards bipolar carbazole-benzonitrile derivatives

The synthesis of *p*BNC, 2BNPC and intermediate 1c was conducted under the Ullmann coupling reaction conditions between 1a and 4-iodobenzonitrile, 5b and 1-bromo-3-iodobenzene, respectively. *p*BNPC, as well as intermediates 5a and 5b, were synthesized by employing Suzuki cross-coupling from 1c, 4-fluorophenylboronic acid pinacol ester and 1,3,5-tribromobenzene, respectively.

*m*BNPC was obtained by the nucleophilic addition reaction between intermediates **1a** and **5a**. Finally, the Rosenmund Von Braun reaction was employed to furnish *m*BNC.

The chemical structures of the target compounds were identified by mass spectrometry, as well as by using IR and NMR spectroscopies and elemental analysis. The data was found to be in good agreement with the proposed structures. All the compounds exhibited characteristic singlet signals at 1.39–1.51 ppm in the ^{1}H NMR spectra which can be attributed to the protons of methyl groups of *tert*-butyl moieties. The characteristic carbon signal of the nitrile moiety was found in the ^{13}C NMR spectra at 117.5–118.8 ppm. All the compounds under investigation are well soluble in common organic solvents, such as chloroform, THF, dichloromethane, toluene or ethyl acetate.

4.3.2. Geometries and Electronic Properties
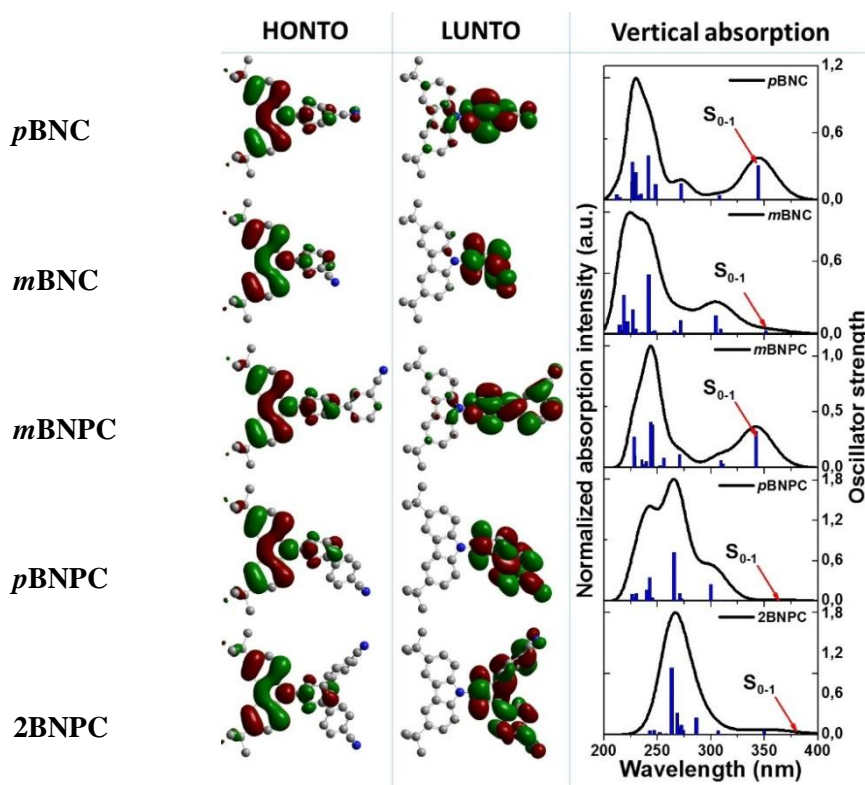
Figure 4.3.1. Views on the natural transition orbitals of S_{0-1} transitions and the vertical absorption spectra of carbazole-benzonitrile derivatives (functionals used: BMK for **2BNPC**, MPW1B95 for others /6–31G(d) in vacuum)

Molecular geometries of the compounds in the ground state were optimized by using DFT calculations with B3LYP/6-31G (vacuum) level of theory (**Fig. 4.3.1.**). TD–DFT calculations were performed by using the MPW1B95 functional.

Benzonitrile is by far the weaker electron acceptor compared to triazine; thus molecular geometry is expected to be partially twisted. Indeed, ca. 50° dihedral angle regarding the C–N bond was found for all the molecules. Analysis of the bond lengths revealed no significant differences. However, the introduction of an extra phenylene spacer and the consequent usage of *para-* or *meta-* linkage results in quite different overall geometry of molecules: the *para*-phenylene spacer bearing *m*BNPC is relatively planar, whereas the molecular skeletons of *meta*-phenylene containing *p*BNPC and 2BNPC are highly twisted.

Electronic transitions, as well as NTOs corresponding to the S_{0-1} excitation, were simulated by means of TD–DFT by using functionals selected according to the OHF method. In terms of the differences in the molecular structure, the D and A linking pattern has an obvious impact on the resulting vertical transitions across the series. The usage of the *para*-phenylene linkage results in more effective conjugation, which is confirmed by the higher oscillator strength of S_{0-1} transition of *p*BNC and *m*BNPC compared to the rest of the series. This is also reflected by the NTOs: higher overlapping of NTOs appears in *p*BNC and *m*BNPC, whereas *meta*-phenylene reduces conjugation, which results in more pronounced molecular orbital localization within the molecules. The ability of the *meta*-linkage to localize charges in the excited state was confirmed. The calculated values of *q* are ca. 0.05–0.1 larger for the *meta*-phenylene linkage bearing compounds compared to their *para*-phenylene-linked analogues.

4.3.3. Thermal, Electrochemical and Photoelectrical Properties

In general, thermal characteristics directly depend on the molecular weight of a compound [201]. The higher is the molecular weight, the higher are the melting point, the glass transition, as well as the thermal decomposition temperatures. Since all the compounds possess the same number of *tert*-butyl groups, similar general thermal trends were observed by DSC and TGA. During TGA experiments, all the compounds (except for 2BNPC), sublimed, which indicates too low molecular weight for high precision vacuum deposition (**Table 4.3.1**). The DSC experiment revealed that all the compounds except for 2BNPC can be converted into the glassy state by cooling the melt. A comparison of the characteristics of *p*BNC and *m*BNC revealed that *para*-linkage was responsible for a 22 °C higher glass transition temperature. It should be noted that *m*BNC demonstrated the lowest glass transition temperature of 58 °C, which is too low for practical applications since such devices as OLEDs, OFETs and OSCs can heat up to more than 60 °C in real-life conditions [202]. All the compounds described in this chapter are well-soluble in the majority of common organic solvents, which enables their use in solution-processing applications.

The electrochemical and charge-transporting properties were investigated by employing the CV and CELIV techniques, respectively (**Fig. 4.3.2.**). All the researched carbazole-benzonitrile derivatives showed bipolar behavior in the above mentioned experiments. The blocked C–3 and C–6 positions of carbazole moieties allowed the compounds to undergo reversible oxidation during the CV experiment. The molecular structure was found to exert influence on the

electrochemical behavior. The appearance of an extra phenyl spacer lowers the IP by ca. 0.1 eV, independently from the used linkage. Among the extra phenylene spacer bearing compounds, the *meta*-phenyl linkage enhances EA. Thus the EA values of *p*BNPC and 2BNPC were found to be 0.2–0.3 eV higher than that of *m*BNPC. This data is consistent with that of other *para*- and *meta*-linked carbazole-benzonitrile derivatives [119].
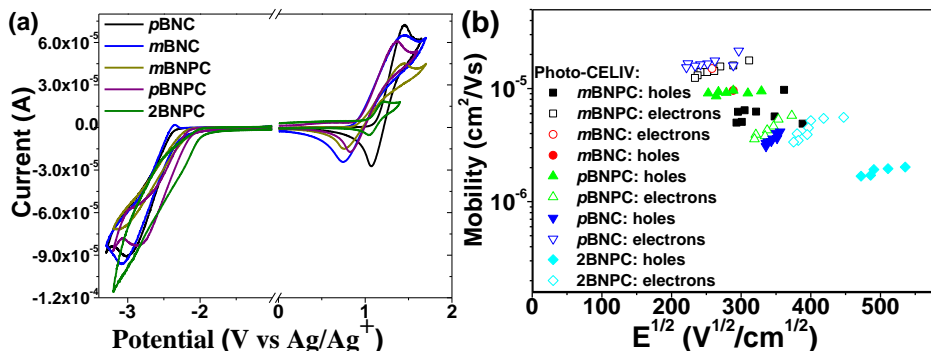

Figure 4.3.2. (a) Cyclic voltammetry scans of dilute 1 μg/ml solutions and (b) electric field dependencies of the hole-drift mobilities of the layers of carbazole-benzonitrile derivatives

Table 4.3.1. Thermal, photophysical, electrochemical and photoelectrical characteristics of carbazole-benzonitrile derivatives

Compound	T_g, °C[a]	T_M, °C[a]	T_{cr}, °C[a]	$T_{dec-5\%}$, °C[b]	E_T, eV[d]	IP^{CV}, eV[e]	EA^{CV}, eV[e]	μ, cm²/(V·s)[f]
pBNC	80	218/220	120/131	277*	2.98	5.79	2.36	h: $3.42 \cdot 10^{-6}$ e: $1.66 \cdot 10^{-5}$
mBNC	58	150	-	281*	2.99	5.77	2.37	h: $9.6 \cdot 10^{-6}$ e: $1.5 \cdot 10^{-5}$
mBNPC	87	192	-	299*	2.75	5.66	2.44	h: $6.24 \cdot 10^{-6}$ e: $1.56 \cdot 10^{-5}$
pBNPC	94	212	-	319*	2.76	5.68	2.60	h: $7.71 \cdot 10^{-5}$ e: $1.26 \cdot 10^{-4}$
2BNPC	-	327/335	242	373	2.75	5.67	2.72	h: $1.91 \cdot 10^{-6}$ e: $4.49 \cdot 10^{-6}$

[a]Determined by DSC; [b]Determined by TGA; *Compounds sublimed during the TGA experiment; [c]Determined from UV/Vis spectra; [d]Determined from phosphorescence spectra; [e]Determined by CV in CH_2Cl_2 solutions. IP^{CV} estimated from the onset oxidation potential by using the relationship $IP_{CV}=|e|(4.8+E_{ox}^{onset})$. EA^{CV} estimated from the onset reduction potential by using the relationship $EA_{CV}=|e|(4.8+E_{red}^{onset})$. [f] Mobility value obtained by CELIV method.

A summary of the thermal, electrochemical, photoelectrical and main photophysical properties is presented in **Table 4.3.1**. Balanced bipolar charge mobility was detected for all the compounds under investigation. Interestingly, electron mobility was found to be of higher values than hole mobility. Since charge mobility is strongly morphology-dependent, no clear structure-property relationship could be estimated. However, compound *p*BNPC demonstrated one order of magnitude higher values of charge mobility compared to all the other

compounds of the series. This observation may be attributed to the beneficial molecular packing for the drift of charges in solid state.

4.3.4. Photophysical Properties

Our photophysical investigation involved a combination of UV/Vis, steady-state and time-resolved fluorescence spectroscopies as well as temperature-dependent measurements. **Fig. 4.3.3** presents the main results of the steady-state measurements. The UV/Vis spectra were normalized according to the local excitation band of carbazole (295–305 nm). Apparently, the conjugation length and strength exerts a significant effect on the absorption of the compounds under investigation. The usage of the *para*-phenylene linkage (***p*BNC** and ***m*BNPC**) results in relatively higher intensity LEBs (3.5–4.0 eV) compared to the *meta*-phenylene linkage bearing analogues. Two benzonitrile acceptors bearing **2BNPC** due to their increased electron accepting strength demonstrated stronger CT characteristics, which can be noticed from the lower energy of the optical bandgap (E_g^{opt}) (3.25 eV).
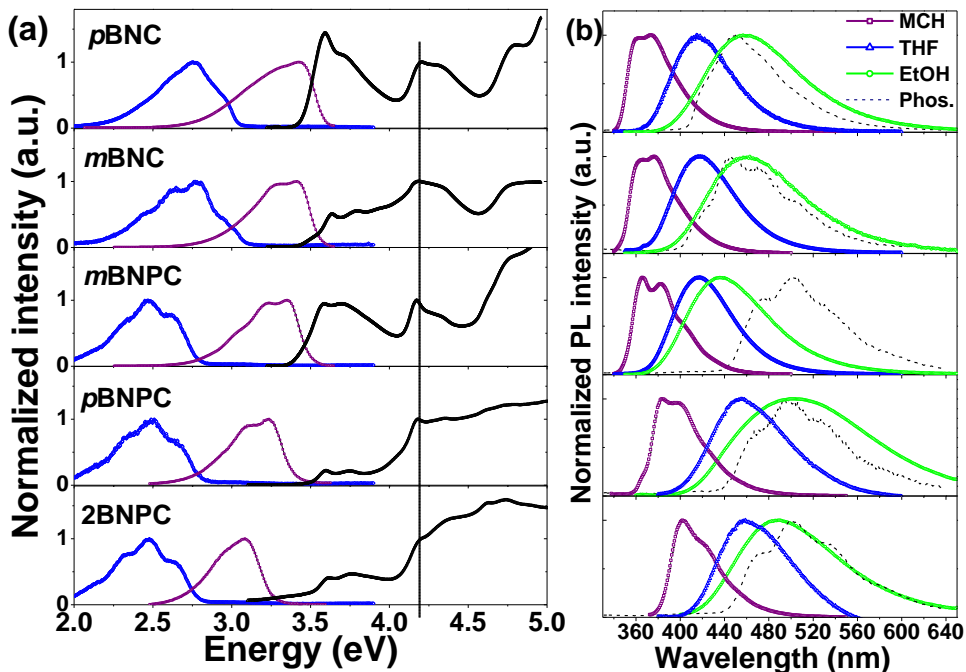
Figure 4.3.3. (a) UV/Vis (black triangles), fluorescence (violet squares) and phosphorescence (blue rhombus) spectra of carbazole-benzonitrile derivatives dispersed in *Zeonex* (1 wt.%). The dashed line depicts the normalization point of UV/Vis spectra and (b) Fluorescence spectra of the solutions in the solvents of different polarity. Phosphorescence spectra (the dashed lines) are also depicted

The existence of the ICT state was observed during steady-state PL measurements. The PL spectra of all the compounds became broad and structureless upon the increase of the environment polarity. In the case of compounds containing no extra phenylene spacer, i.e., ***p*BNC** and ***m*BNC**, the

conjugation pattern (*para-* or *meta-*) does not impact the CT strength. Almost identical bathochromic shifts and the broadening of PL spectra were observed upon the increase of the environment polarity. However, the insertion of an additional phenylene spacer which is independent from the linking pattern in use resulted in the shift of the singlet emission band towards the lower energy. Among the compounds, the energy of the emission band decreased in the order ***m*BNPC**>***p*BNPC**>**2BNPC**. In addition, the extra phenylene spacer was found to cause the decrease of the triplet energy by 0.24 eV (±0.01 eV). The usage of *meta*-benzonitrile linked to the donor via *para*-phenylene was found to be responsible for the weaker CT. In comparison, ***m*BNPC** possesses a weaker CT character than ***p*BNPC** and **2BNPC**.

As it can be perceived from **Fig. 4.3.3.b.**, a combination of a benzonitrile acceptor and a carbazole donor resulted in a relatively weak ICT. The energy of the ^{1}CT band decreased only by 0.55–0.76 eV with the increase of the solvent polarity going from methylcyclohexane to a highly polar ethanol (ε=24.5). The energy of the ^{1}CT band becomes comparable (in the case of all the compounds except for ***m*BNPC**) with the energy of ^{1}T only when a highly polar solvent ethanol is used. Since the majority of the host materials used in OLEDs are of a relatively low polarity (the polarity of DPEPO is in between those of toluene and THF [53]), the weak CT in these compounds encumbers their application as emitters. However, the high values of E_T, as well as the bipolar charge mobility of ***p*BNC** and ***m*BNC**, make them attractive candidates as hosts for blue OLEDs (both TADF-based and phosphorescent ones). The other compounds from the series (bearing an extra phenylene spacer) can apparently be applied as host materials for green OLEDs. They exhibit bipolar charge mobility and enhanced thermal stability compared to that of ***p*BNC** and ***m*BNC**, and also feature tunable IP and EA levels (see **Table 4.3.1.**).
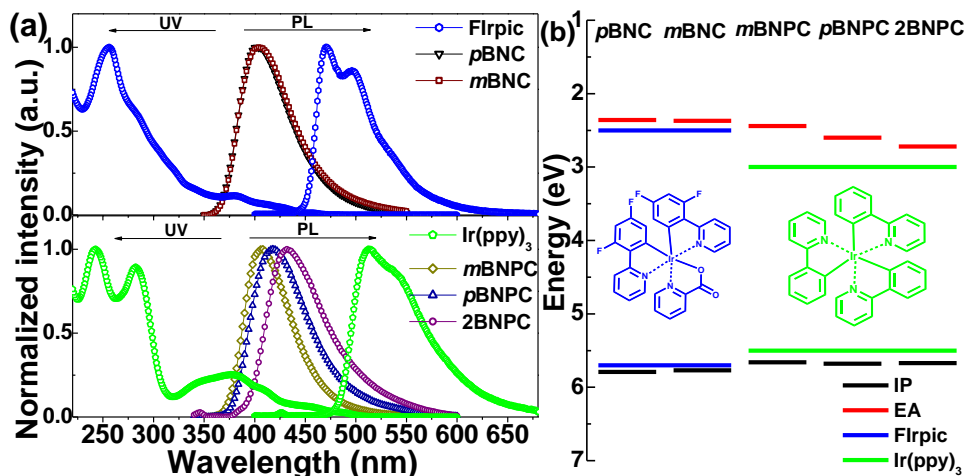

Figure 4.3.4. (a) UV/Vis absorption and emission spectra of blue- and green-emitting iridium complexes and the photoluminescence of neat films of carbazole-benzonitrile derivatives; (b) energy diagram of the ionization potentials and electron affinities of iridium complexes and compounds under investigation

In order to achieve a host-guest energy transfer, the host emission should overlap with the absorption of the emitter, and the host should energetically straddle the guest [56]. Apparently, all the compounds under investigation meet these criteria since the emission of their neat films lies within the absorption range of blue/green iridium complexes; also, the ionization potential and electron affinity values straddle those of the blue/green iridium complexes (**Fig. 4.3.4.**). Moreover, the neat films of the compounds are, apparently, of a moderately low polarity. The PL spectra of neat films are situated between those of the solutions in MCH and THF. This is essential for the potential application of these compounds in TADF OLEDs. A higher polarity of a host can shift the resulting emission to the red region of the spectrum.

To conclude, in this chapter we showed how by manipulation of the molecular structure it is possible to tune the properties of the resulting compounds. By varying the *para-* or/and *meta-* linkage together with the introduction of an extra phenylene spacer, we are able to prepare thermally and electrochemically stable bipolar charge transporting materials with tunable energy levels.

4.4. Isomeric Derivatives of 9,9-dimethyl-9,10-dihydroacridine and Benzonitrile

By combining the previously reported knowledge, we designed, synthesized and investigated a series of isomeric acridine-benzonitrile hybrid materials. Along with triazine, benzonitrile stands firmly on the peak of the most stable and reliable electron accepting moieties for the design and synthesis of blue emitters [28,34,79,83,92,96,97,100,197,203–205]. In the meantime, carbazole and acridine hold the lead among the donor species [87,92–94,96,103,197,206]. As it was observed in Chapter 4.3., when carbazole is used, due to its poorer electron donating ability compared with acridan, it is more difficult to push the singlet emission of the resulting compound from the UV region to the visible blue region. Due to this and by taking into account the recent progress in the synthesis of blue-emitting acridane-based TADF compounds [33,53,103,192,207], we decided to employ the stronger electron donor acridine in low-molar-mass emitting systems (**Scheme 4.4.1**) and to investigate them thoroughly in order to show how a combination of D and A units, as well as the linking pattern between them, can lead to the achievement of the desirable properties of the resulting compound.

4.4.1. Synthesis

Intermediates **2a**, **2b**, and **2c** were prepared by employing diazotization-iodination reactions from the appropriate starting materials, and target compounds were procured by using the Buchwald-Hartwig procedure. All the compounds were purified by employing column chromatography, which was followed by crystallization.
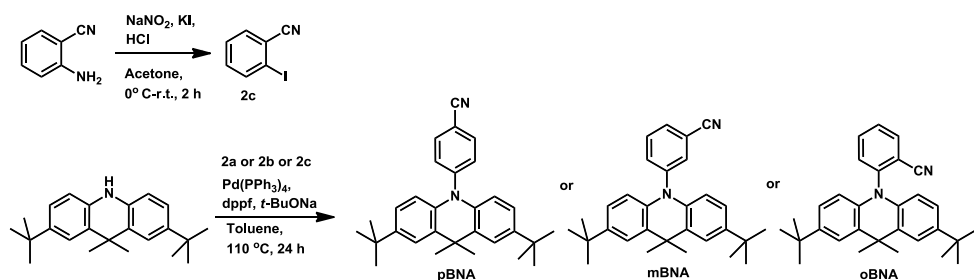
Scheme 4.4.1. Synthetic routes towards ACR-benzonitrile derivatives

The chemical structures of the target compounds were identified by mass spectrometry, as well as by IR and NMR spectroscopies and elemental analysis. The data was found to be in good agreement with the proposed structures. All the compounds exhibited characteristic singlet signals at 1.26–1.27 ppm in ^{1}H NMR spectra which can be attributed to the protons of the methyl groups of *tert*-butyl moieties. Other characteristic singlet signals corresponding to methyl groups at the C–9 position of the acridine moiety were found to be distributed in the range of 1.62–1.69 ppm in ^{1}H NMR spectra. The characteristic carbon signal of the nitrile moiety was found in all the ^{13}C NMR spectra at 117.0–118.5 ppm. All the compounds under investigation are well-soluble in common organic solvents, such as chloroform, THF, methylene chloride, toluene or ethyl acetate.

4.4.2. Geometries and Electronic Properties
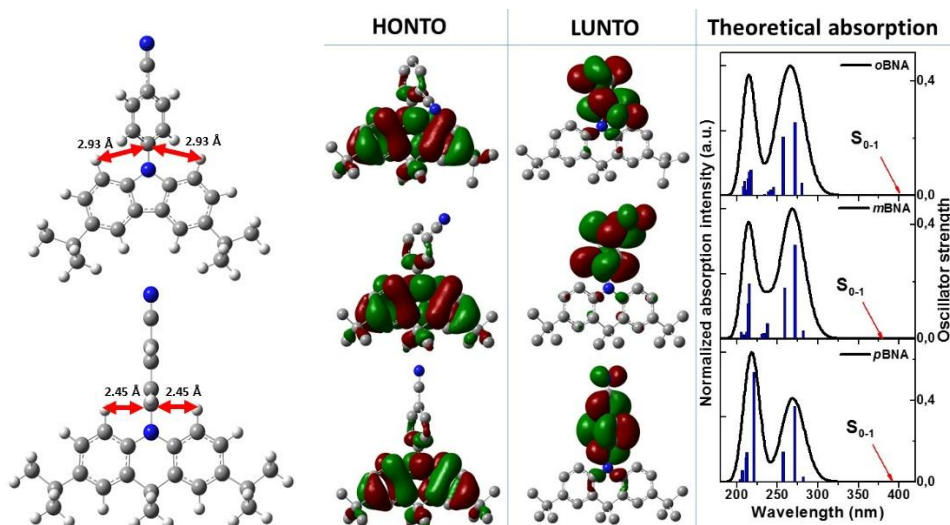
Figure 4.4.1. (a) Molecular geometries of *p*BNC and *p*BNA and (b) the view on the natural transition orbitals of S_{0-1} transition and vertical absorption spectra of acridine-benzonitrile derivatives (BMK/6-31G(d) in vacuum)

The molecular geometries of the compounds in the ground state were optimized by using DFT calculations with the B3LYP/6-31G (vacuum) level of theory. Acridine consists of a hexagonal inner ring, whereas the inner ring of carbazole is pentagonal (**Fig.4.4.1**). Due to the extension of the inner ring, each

82

ortho-hydrogen (related to the nitrogen atom) in an acridine unit is ca. 0.48 Å closer to the N–C carbon atom (the N–C bond of the aromatic substituent), which results in almost 1 Å shorter length of the rotational freedom for the substituent – this makes it possible to ensure the perpendicular orientation of the substituent. This fundamental advantage, along with the high triplet energy (3.05 eV) and the strong electron donating ability brought the fame to the acridine moiety as the ideal building block for blue-emitting TADF materials [33,53,92,103,192,197,208].

Molecular geometry optimizations of benzonitrile-substituted acridine derivatives confirmed the above described steric influence of the *ortho*-hydrogens to the torsion of the substituent: independently from the linking pattern in use, the benzonitrile unit was found to be perpendicular to the acridine plane in all the series of compounds under investigation. This perpendicular D–A structure ensures efficient excited state charge separation, which was confirmed by the simulation of the NTOs of S_{0-1} transition: the hole is mostly localized on the acridine, and the particle is situated on the benzonitrile unit (**Fig. 4.4.1.**). A calculation of the CT extent revealed high values of *q* of 0.89 for *p*BNA and of 0.91 for *o*BNA and *m*BNA. A slightly lower value of *q* for *p*BNA is apparently due to the relatively higher degree of LUNTO delocalization through the acridine part compared to the values of the other molecules.

4.4.3. Steady-State Photophysics
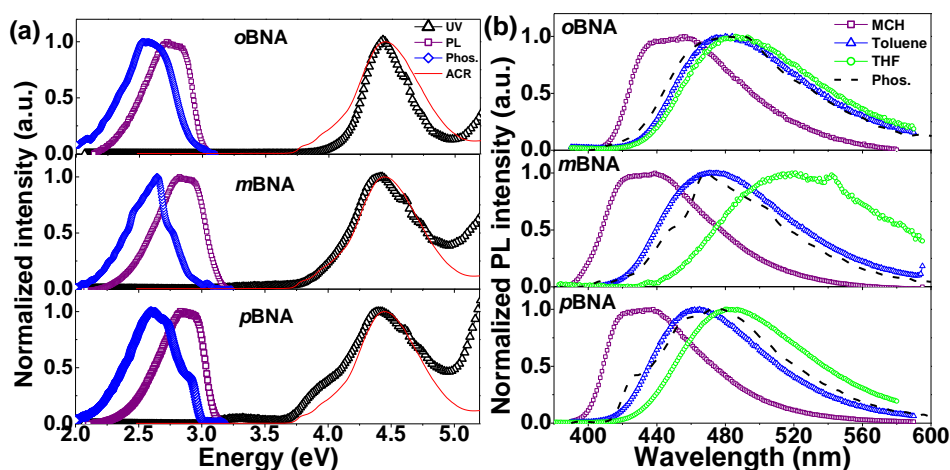
Figure 4.4.2. (a) UV/Vis (black triangles), fluorescence (violet squares) and phosphorescence (blue rhombus) spectra of acridine-benzonitrile derivatives dispersed in *Zeonex* (1 wt.%). The absorption spectrum of acridine (red curves) is included. (b) Fluorescence spectra in solvents of different polarity. Phosphorescence spectra (dashed lines) are also depicted

Steady-state PL measurements were performed for solid and liquid solutions of the compounds under investigation. As it can be perceived from **Fig. 4.4.2.a.**, all the compounds possess a dominant absorption band in the range of 3.75–5.00 eV, which can be attributed to the local excitation of the acridine moiety.

However, the linking pattern was found to exert influence on the optical absorption spectra: while the absorption of *ortho-* and *meta*-substituted compounds resembles that of acridine, the appearance of the lowest energy band (LEB) at the energies of 3.25–3.75 eV was observed for **pBNA**. The singlet emission of the solution in nonpolar media (methyl cyclohexane) was observed at similar energies for all the compounds, whereas the triplet emission (recorded for THF solutions at 77 K) spectra were found to possess different shapes (**Fig. 4.4.2.b.**). While the shapes of the phosphorescence spectra of **mBNA** and **pBNA** are similarly resolved, that of **oBNA** remains weakly resolved. This is an indication of competition between the emission from ^{3}LE and ^{3}CT states in the spectrum of **oBNA**, whereas more resolved spectra of the two other compounds indicate the origin of emission mostly from ^{3}LE states.

The PL spectra of the synthesized derivatives revealed the sensitivity of the ^{1}CT state to the solvent polarity. Apparently, **mBNA** possesses the most sensitive ^{1}CT state, since, for this compound, the largest bathochromic shift of the PL spectra was found upon the increase in the polarity of media. The ^{1}CT state of **pBNA** can be characterized as slightly less polarity-sensitive than that of **mBNA**, whereas the least polarity-sensitive is the PL of **oBNA**. It is noteworthy that the least polarity-sensitive ^{1}CT state of **oBNA** can prove to be advantageous when seeking to preserve the same emission color with the aim of fabricating OLEDs since the polarity effects in the solid state are more expressed and thus they usually lead to the red shift of the emission band.
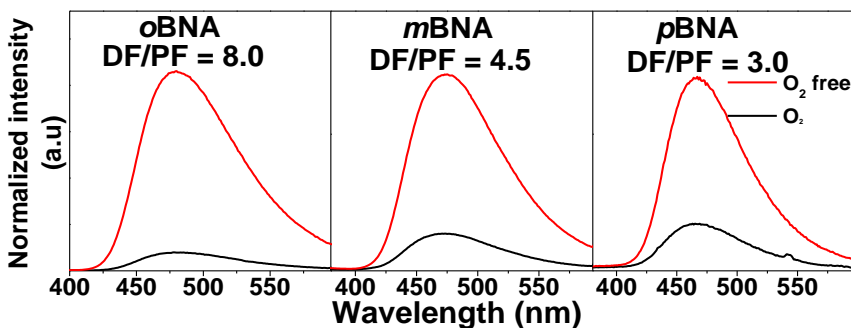
Figure 4.4.3. Steady-state PL spectra of dilute toluene solutions of acridine-benzonitrile derivatives recorded in ambient and oxygen-free atmospheres (λ_{ex}=300 nm)

In order for strong TADF to occur, it is necessary not only to achieve a small ΔE_{ST} gap but also to ensure that the triplet formation yield (Φ_{ISC}), as well as the yield of the singlet state, formed by a reverse intersystem crossing from the triplet state (Φ_{rISC}), would be as high as possible [56]. The triplet emission overlaps with the singlet emission in the spectra of the solutions in toluene of all the compounds under investigation; thus toluene was chosen for the deoxygenation experiment (**Fig. 4.4.3.**). Steady-state PL spectra were recorded in the ambient as well as in deoxygenated atmosphere while keeping the instrument parameters unchanged. Since oxygen quenches triplet emission, the emission spectra recorded in ambient conditions represent prompt fluorescence (PF) whereas the spectra recorded in the deoxygenated atmosphere represent the

emission consisting of prompt and delayed fluorescence (PF+DF). From the intensities ratio, it is possible to calculate the Φ_{ISC}. The values of Φ_{ISC} were found to be 0.67, 0.78 and 0.88 for compounds *p*BNA, *m*BNA and *o*BNA, respectively. The highest triplet formation yield, along with the smallest value of ΔE_{ST} and the highest value of the theoretically calculated *q* for *o*BNA, suggest that this compound may possess the most efficient TADF among the compounds of the series.

4.4.4. Time-Resolved Photoluminescence Measurements
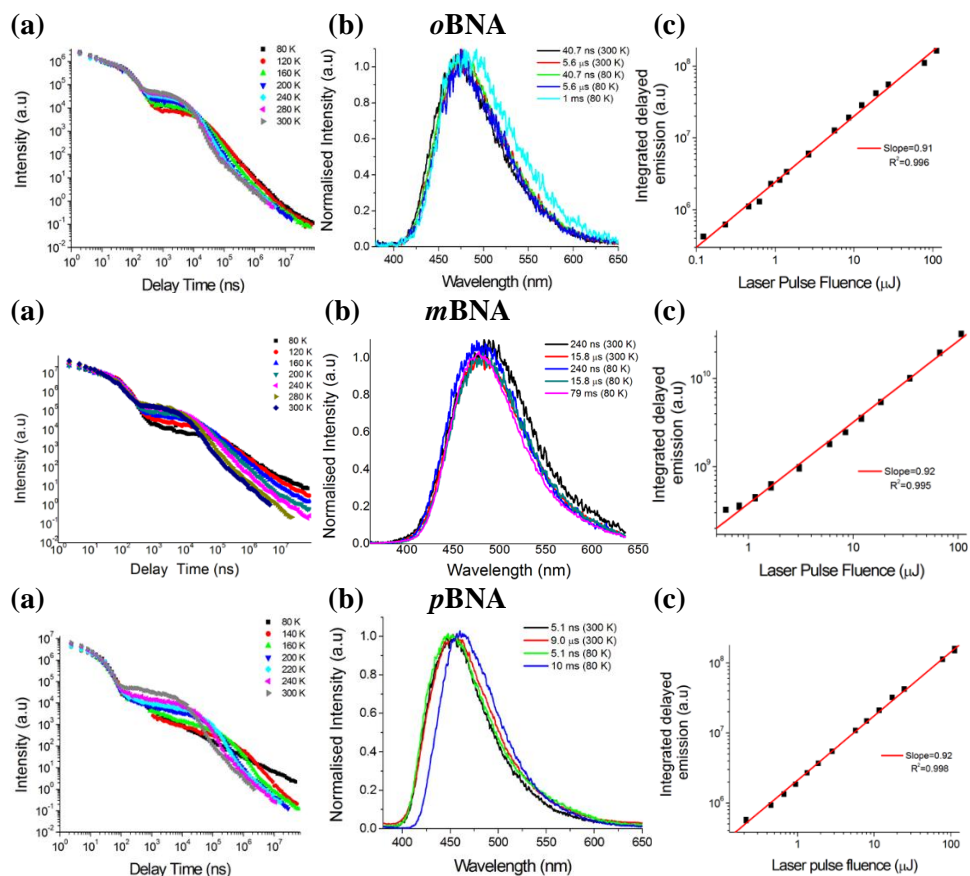
Figure 4.4.4. Plots of 10% w/w solid solutions of the compounds under investigation in DPEPO: (a) emission intensity against delay time measured at 80 K (black), 120 K (red), 160 K (green), 200 K (blue), 240 K (cyan), 280 K (pink), and 300 K (grey); (b) normalized emission spectra at varying delay times at 300 K and 80 K and (c) laser fluence versus delay emission intensity. Delay time=9 μs, integration time 100 μs

Time and temperature-resolved measurements were performed for solid solutions in polar host DPEPO (**Fig. 4.4.4.**). Emission spawning within the time range from 10^{-9} s up to 10^{-2} s was recorded at different temperatures in order to characterize the excited state kinetics (**Fig. 4.4.4.a.**). Apparently, all the compounds can be characterized as DF emitters. The curves of prompt emission

(10^{-9} s to 10^{-7} s) retain the same intensity at the selected temperature rage. Delayed emission (from 10^{-7} s to 10^{-5} s) revealed the temperature dependence for all the derivatives. Clear DF intensity increase with the increase of temperature was observed. At the longest delay times (10^{-4} s to 10^{-7} s) and the lowest temperatures, the evolution of DF to phosphorescence was observed. **Fig 4.4.4.b** presents normalized emission spectra recorded at varying delay times at 80 K and 300 K. It can be noticed that the shapes and the spectral position of PF, DF and phosphorescence curves remain at the same wavelengths for *o*BNA and *m*BNA, while in the case of *p*BNA, a low temperature phosphorescence spectrum was found to be red-shifted compared with the PF and DF spectra. Apparently, the values of ΔE_{ST} for the dispersions *o*BNA and *m*BNA in DPEPO are <20meV, whereas the value of the dispersion of *p*BNA is by 1 order of magnitude higher (>100meV). **Fig. 4.4.4.c** presents the DF intensity dependence on the laser fluence. The linear singular dependence of PF and DF reveals that the delayed fluorescence is of the thermally activated origin [59] for all the compounds of the series.

4.4.5. Thermal, Electrochemical and Photoelectrical Properties

Since all the compounds are of the same molecular weight, similar behavior during the thermal stability measurement (TGA) is also expected. Indeed, in the temperature range of 240–252 °C, all the compounds sublimed (**Fig. 4.4.5.**). Sublimation at this temperature range in the atmospheric pressure indicates slightly too low molecular weight of these isomeric derivatives for the high precision vacuum deposition approach. However, the compounds are readily soluble in most organic solvents, which makes them good candidates for solution-processing.
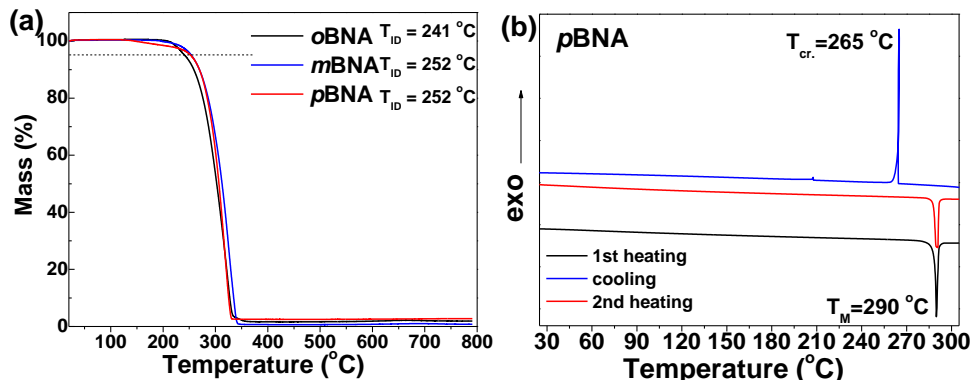
Figure 4.4.5. (a) TGA curves of acridine-benzonitrile hybrid compounds and (b) DSC curves of *p*BNA

All the compounds were isolated as crystalline materials, and it was also confirmed by DSC. As an example, the DSC curves of *p*BNA are shown in **Fig. 4.4.5**. An endothermic signal corresponding to melting was observed during the first heating scan, which was followed by an exothermic crystallization peak observed upon cooling. Heating the melted sample resulted in a single melting peak. The summary of thermal characteristics is presented in **Table 4.4.1**.

Table 4.4.1. Thermal, photophysical, electrochemical and photoelectrical characteristics of acridine-benzonitrile derivatives

Compound	T_g, °C[a]	T_M, °C[a]	T_{cr}, °C[a]	T_{sub}, °C[b]	E_T, eV[d]	IP^{CV}, eV[e]	EA^{CV}, eV[e]
*o*BNA	97	242	115	241*	3.03	5.39	2.30
*m*BNA	-	198	151	252*	3.10	5.34	2.30
*p*BNA	-	290	265	252*	2.92	5.30	2.31

[a]Determined by DSC; [b]Determined by TGA. *Compounds sublimed during the TGA experiment; [c]Determined from UV/Vis spectra; [d]Determined from phosphorescence spectra; [e]Determined by CV in CH_2Cl_2 solutions. IP^{CV} estimated from the onset oxidation potential by using the relationship $IP_{CV}=|e|(4.8+E_{ox}^{onset})$. EA^{CV} estimated from the onset reduction potential by using the relationship $EA_{CV}=|e|(4.8+E_{red}^{onset})$

Electrochemical properties were evaluated by employing CV. **Fig. 4.4.6** presents the CV experiment. All the compounds under investigation showed bipolar behavior, which indicates good charge separation among D and A parts within the molecules. This was also confirmed by the computation of frontier orbitals (**Fig. 4.4.1**). As we observed in the previous chapter, in such low-molar-mass D–A systems the linking pattern only exerts a minor effect on the electrochemical behavior. During the CV experiment, when negative potential was applied, the THF solutions of all the compounds underwent electrochemical reduction, which was followed by oxidation back to the neutral species upon the increase of the potential. Electron affinity values estimated from the reduction potential (relative to ferrocene) were found to be within the error range of the equipment (ca. 2.30 eV). The usage of the same strong electron donor, acridine, resulted in a minor difference in the oxidation potentials. The ionization potential values of the compounds of the series were estimated by employing CV. The values of IP^{CV} were found to be of 5.30, 5.34 and 5.39 eV for *p*BNA, *m*BNA and *o*BNA, respectively.
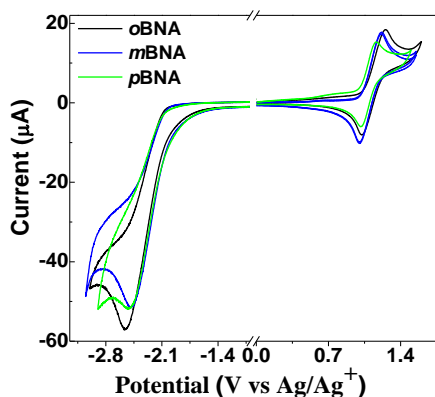
Figure 4.4.6. Cyclic voltammetry scans of dilute 1 µg/ml solutions of acridine-benzonitrile derivatives

To conclude, in this chapter we showed that the proper combination of an electron donor, an acceptor and the linkage between them leads to highly efficient blue TADF emitters. Moreover, the use of electrochemically stable compounds ensures their stability upon electrical excitation. The observed tendencies in the molecular structure-properties relationship can serve as reliable guidelines for the future design of new and efficient compounds possessing the desired properties.

4.5. Linear Donor-Acceptor Benzothiadiazole Derivative

In the final part of this thesis, we present an example of a linear compound containing a strong electron donor and electron acceptor [209]. The idea here was to avoid twisting around the D and A link and to use the strongest possible D and A moieties. Therefore, benzo[c][1,2,5]thiadiazole was selected as the primary A, and fluorinated benzonitrile was chosen as the secondary acceptor. Combining them should result in the enhanced electron accepting ability of the resulting A unit. In the meantime, a strong electron donor triphenylamine was modified by exchanging one phenylene unit to a thiophene moiety. As it was shown in Chapter 4.4.2., the use of a pentagonal connecting ring reduces the twisting around it; therefore, it is expected that such a strong push–pull (D–A) system will remain coplanar. If the experiment is successful, a dye is expected to be received instead of an emitter.

4.5.1. Synthesis

Compound **6a** was prepared by employing the Knoevenagel condensation reaction from active methylene compound **6c** [210] and aldehyde **6d** [211]. **DTA–BTN** was synthesized by performing the Stille coupling reaction from **6a** and **6b** (**Scheme 4.5.1.**). The chemical structure of the target compound was identified by mass spectrometry, as well as by IR and NMR spectroscopies and elemental analysis. The data was found to be in good agreement with the proposed structure. The characteristic singlet signal at 8.44 ppm in ^{1}H NMR spectra was attributed to the geminal proton of the substituted cyanovinylene moiety. Other characteristic multiplet signals corresponding to fluorine atoms at the benzonitrile moiety were found to be distributed in the range of −131.58–131.73 ppm and −137.37–137.52 ppm in ^{19}F NMR spectra. The target compound is well soluble in common organic solvents, such as chloroform, THF, methylene chloride, toluene and ethyl acetate.
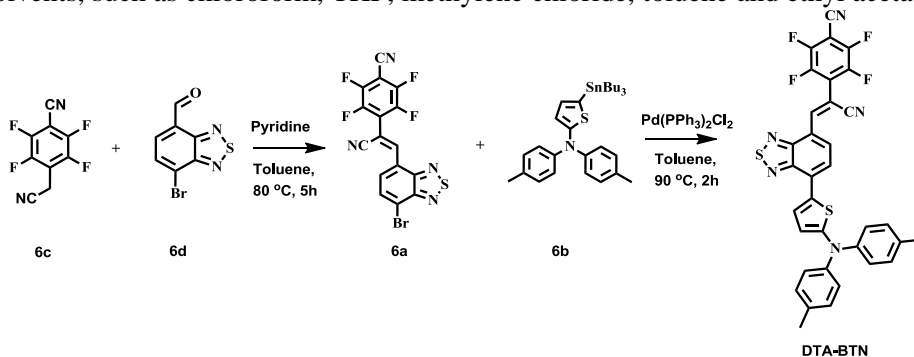
Scheme 4.5.1. Synthetic routes towards **DTA–BTN**

4.5.2. Geometries and Electronic Properties

As it can be perceived from **Fig. 4.5.1.**, the diphenylamine part is twisted; however, the use of the pentagonal electron donating thiophene resulted in its planar orientation together with the benzothiadiazole moiety. In the meantime, the conjugated cyanovinylene ensures the planarity of the upper part of the molecule:

tetrafluorobenzonitrile and cyanovinylene were found to be in one plane together with the benzothiadiazole moiety. Such planar conformation of the molecules ensures strong electronic coupling between the donor and acceptor units. The latter is confirmed by the simulation of frontier orbitals: HOMO and LUMO are delocalized through the entire molecule.

| Geometry | HOMO | LUMO |
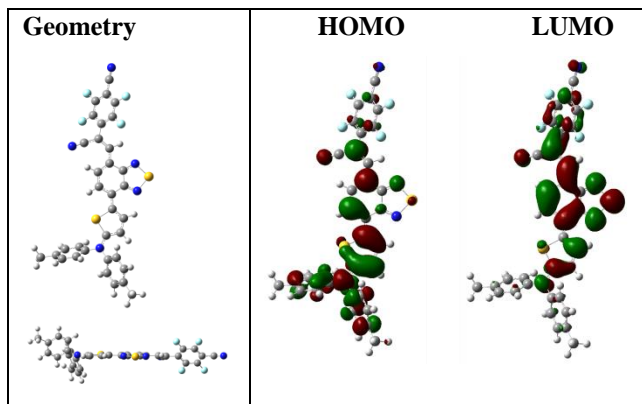
Figure 4.5.1. Molecular geometry, the view on the frontier orbitals (DFT B3LYP/6-31G(d) in vacuum) of **DTA–BTN**

4.5.3. Optical, Thermal and Electrochemical Properties

Fig. 4.5.2.a. presents UV/Vis absorption spectra of the neat films of compounds **6a** and **DTA–BTN**. Apparently, the UV/Vis spectrum of the target compound consists of absorption bands of the acceptor and a relatively highintensity lowest energy band distributed at ca. 500–700 nm region. Since the D and A fragments are in one plane, the mixing of n and π orbitals is efficient; thus it results in a highly allowed ICT band. The optical gap estimated from the onset of the absorption spectra of **DTA–BTN** appears to be as small as 1.57 eV, which is typical for similar types of absorbers [212,213].
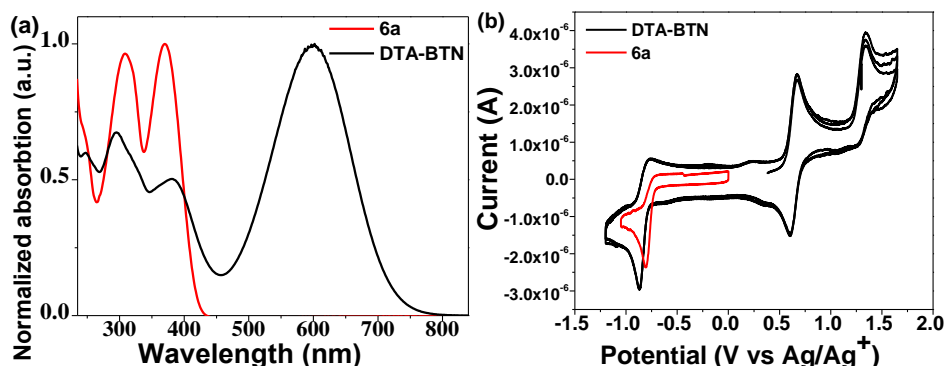
Figure 4.5.2. (a) UV/Vis absorption of neat films and (b) cyclic voltammetry scans of dichloromethane solutions of compounds **6a** and **CTA–BTN**

Cyclic voltammetry is used to determine the frontier energy levels as well as to check the reversibility of redox processes in the compounds under consideration. **Fig. 4.5.2.b.** presents the CV curves of acceptor **6a** and dye **DTA–**

BTN. The acceptor demonstrated reduction only, whereas **DTA–BTN** showed double oxidation and reduction as well. The ionization potential is estimated by using the onset of the first oxidation peak, whereas the value of electron affinity is estimated from the reduction potential onset. The values of IP^{CV} and EA^{CV} for **DTA–BTN** are 5.11 eV and 3.59 eV, respectively. A summary of the most important parameters of **DTA–BTN** is presented in **Table 4.5.1**. The thermal characteristics of **DTA–BTN** were measured by using a combination of differential scanning calorimetry and thermogravimetric analytical strategies. The thermal decomposition temperature was found to be as high as 349 °C, whereas the melting point was found at 228 °C. More than 100 °C difference between the melting temperature and the decomposition temperature ensures vacuum evaporation, as well as a possibility of sublimation for this compound. It is noteworthy that **DTA–BTN** demonstrated a 25% sublimation yield, which is higher than for other analogues [209,214], which makes this material relevant for practical application. The sublimation yield is a crucial condition for the application of a material in the industry, as it provides the opportunity to obtain a higher amount of extra pure material with minimum loss.

Table 4.5.1. Summary of the most important parameters of **DTA–BTN**

Compound	E_g^{opt}, eV^a	E_{OX}, V^b	E_{RED}, V^b	IP^{CV}, eV^c	EA^{CV}, eV^c	T_M, °C^d	$T_{dec\text{-}5\%}$ °C^d
DTA-BTN	1.57	0.31	-1.21	5.11	3.59	228	349

[a]Estimated from the onset of UV/Vis spectra; [b]Onsets of oxidation and reduction potentials; [c]Determined by CV in CH_2Cl_2 solutions. IP^{CV} was estimated from the onset oxidation potential by using the relationship $IP_{CV}=|e|(4.8+E_{ox}^{1/2})$. EA^{CV} was estimated from the onset reduction potential by using the relationship $EA_{CV}=|e|(4.8-E_{red}^{1/2})$; [d]Determined by DSC and TGA.

4.5.4. Photovoltaic Properties
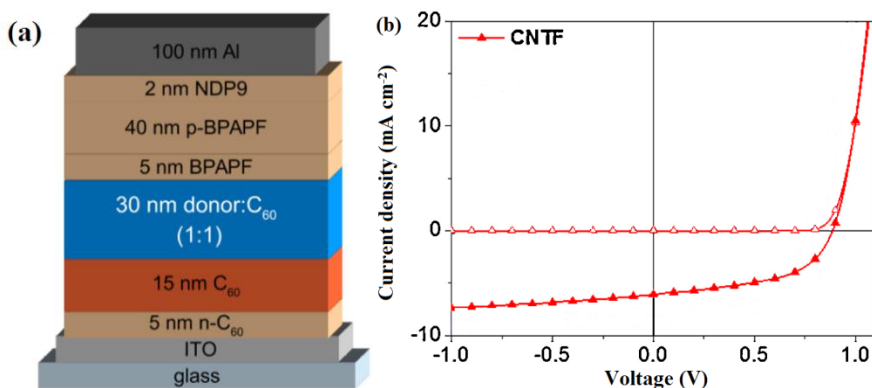
Figure 4.5.3. (a) Scheme of the solar cell stack. (b) *jV*-curves under solar illumination (red curve) and in the dark (black curve) of the solar cells

Compound **DTA–BTN** was tested as an absorber in a solar cell in a non-optimized device architecture presented in **Fig. 4.5.3.a**. An electron transport layer consisting of 5 nm n-doped C_{60} (3 wt% $W_2(hpp)_4$) is deposited on a semitransparent ITO electrode. Afterwards, 15 nm of intrinsic C_{60}, followed by a 30 nm thick blend layer consisting of **DTA–BTN** in a 1:1 volume mixing ratio

with C_{60} comprise the absorber layer. A 5 nm layer of intrinsic BPAPF serves as a buffer layer between the intrinsic absorber layers and the p-doped BPAPF (10 wt% NDP9, 40 nm). The subsequent 2 nm of p-dopant NDP9 are expected to ensure an ohmic contact with the aluminum electrode. **Fig. 4.5.3.b.** shows the *jV*-curves of the solar cells, and **Table 4.5.2.** presents a summary of the solar cell parameters. Power conversion efficiency of 2.4% was achieved. Open circuit voltage of 0.88 V and a fill factor of 53% were achieved.

Table 4.5.2. Solar cell parameters.

Compound	V_{OC}, V^a	$j_{SC}, mA \cdot cm^{-2b}$	$FF, \%^c$	$I, mW \cdot cm^{-2d}$	$PCE, \%^e$
DTA-BTN	0.88	5.4	53	103	2.4

[a]Open circuit voltage; [b]Current density; [c]Fill factor; [d]Irradiance of sun; [e]Power conversion efficiency.

The power conversion efficiency value of 2.4% is an average value for such a type of solar cells [215]; however, **DTA–BTN** proved to be a thermally stable absorber, which is greatly important for practical applications. To conclude, we designed and synthesized a linearly connected D–A compound which was successfully tested as an absorber in the solar cell.

5.   CONCLUSIONS

1. Three star-shaped derivatives of triazine and carbazole with a different linking topology of the chromophores and differently substituted pheripherical carbazolyl moieties were synthesized, and their properties were studied.

    1.1. The compounds demonstrated high thermal stability with 5% weight loss temperatures exceeding 460 °C; they exhibited ability to form glasses with glass transition temperatures exceeding 97 °C.

    1.2. A combination of three carbazole donor moieties and a strong electron accepting triphenyltriazine core resulted in a strong intramolecular charge transfer confirmed by solvatochromism study of emission.

    1.3. Linkage of chromophores via a rigid ethynyl bridge (as well as connection of the carbazole moiety through the C–3 position to the core) results in the extension of conjugation through the molecules, which is evidenced by the increased oscillator strength, photoluminescence quantum yield and short fluorescence lifetime. The introduction of a C–N bond to the molecules compared with a C–C bond results in 0.3 eV higher triplet energy.

    1.4. Compounds bearing C–C and C–N bonds between the chromophores were tested as emitters in OLEDs prepared by wet processing. The usage of the triazine derivative with a C–C bond as an emitter gave rise to green electroluminescence with the maximum brightness of 1342 cd/m^2, whereas the exploitation of the emitter with a C–N bond resulted in a blue emitting OLED with the maximum brightness of 1221 cd/m^2 observed at 18 V for both devices, with the maxima of the current efficiency in the range of 0.1–0.55 cd/A.

2. Two isomeric triazine and carbazole derivatives with a different linking pattern of the chromophores were synthesized, characterized and investigated as TADF emitters.

    2.1. The *para*-linkage pattern provides a higher oscillator strength, as well as fluorescence quantum yield, compared to the values of the compound featuring *meta*-linkage.

    2.2. The compound with *meta*-linkage exhibits stronger charge transfer behavior, a higher triplet energy and smaller singlet-triplet energy splitting compared to those of the compound with *para*-linkage.

    2.3. Both isomers show thermally activated delayed fluorescence; however, the *meta*-isomer is characterized by more intense delayed emission with a shorter lifetime and lower activation energy.

    2.4. The triazine derivative with *meta*-linkage shows good performance as a blue TADF emitter in OLED with the maximum external quantum efficiency of 9.5%.

3. Five bipolar derivatives of carbazole and benzonitrile with different linking patterns and conjugation lengths were prepared and characterized.

3.1. The introduction of an additional phenylene unit resulted in the increase of the 5% weight loss temperatures (299–373 °C) and glass transition temperatures (87–94 °C). The use of the *para*-linking pattern also resulted in the enhancement of these characteristics.

3.2. All the synthesized derivatives of carbazole and benzonitrile exhibited both reversible oxidation and reduction in cyclic voltammetry experiments. Compounds containing an extra phenyl ring exhibited lower values of the ionization potential (5.66–5.68 eV) compared to the compounds with the direct linkage of the donor and the acceptor (5.77–5.79 eV).

3.3. All the compounds exhibited bipolar charge transport with the highest charge mobilities characteristic of 3'-(3,6-di-*tert*-butyl-9H-carbazol-9-yl)-[1,1'-biphenyl]-4-carbonitrile (7.71×10^{-5} cm^2/Vs for holes and 1.26×10^{-4} cm^2/Vs for electrons at an electric field of $6.4 \cdot 10^5$ V/cm).

4. Three isomeric derivatives of acridine and benzonitrile differing in terms of the donor/acceptor linking pattern were prepared and studied.

4.1. The compound with the *ortho*-linkage between chromophores possesses glass-forming ability with a glass transition temperature of 97 °C. The sublimation temperatures of the compounds were discovered to be within the temperature range of 241–252 °C.

4.2. The compounds possess small singlet-triplet energy splitting gaps (<100 meV) and exhibit blue thermally activated delayed fluorescence. The compound with the *ortho*- linkage between the donor and the acceptor moieties exhibits the highest triplet formation yield of 0.88, which makes it the most efficient blue TADF emitter within the series.

5. A new linear donor-acceptor benzothiadiazole derivative was synthesized and characterized.

5.1. The compound demonstrated a wide range of UV/Vis absorption reaching 700 nm, and a narrow optical gap of 1.57 eV.

5.2. The usage of the perfluorinated benzonitrile moiety improved the thermal stability of the synthesized compound with the sublimation yield values exceeding 25%.

5.3. Estimated values of the ionization potential and the electron affinity are 5.11 eV and 3.59 eV, respectively.

5.4. The compound was tested as an absorber in an organic solar cell, which demonstrated its power conversion efficiency of 2.4%.

6. REFERENCES

1. *CURRENT World Population*. (2017). (seen on May 10, 2017). Available at: http://www.worldometers.info/world-population/

2. TRINKAUS, E. (2005). Early Modern Humans. In: *Annual Review of Anthropology*. 2005, vol. 34, 207–230. Available at: http://www.annualreviews.org/doi/10.1146/annurev.anthro.34.030905.154913

3. ANTÓN, S.C., SWISHER, III, C.C. (2004). Early Dispersals of Homo from Africa. In: *Annual Review of Anthropology*. 2004, vol. 33, 271–296. Available at: http://www.annualreviews.org/doi/10.1146/annurev.anthro.33.070203.144024

4. KREMER, M. (1993). Population Growth and Technological Change: One Million B.C. to 1990. In: *Quarterly Journal of Economics*. 1993. vol. 108, 681–716. Available at: http://faculty.econ.ucdavis.edu/faculty/gclark/210a/readings/kremer1993.pdf

5. DAHLMAN, C. (2007). Technology, Globalization, and International Competitiveness: Challenges for Developing Countries. (seen on May 14, 2017). Available at: http://www.un.org/esa/sustdev/publications/industrial_development/1_2.pdf

6. *URBAN Population Growth*. (2015). By: World Health Organisation. (seen on July 12, 2017). Available at: http://www.who.int/gho/urban_health/situation_trends/urban_population_growth_text/en/

7. ALL Volvo Cars to be Electric or Hybrid from 2019. (2017). In: *The Guardian*; July 05, 2017. (seen on August 20, 2017). Available at: https://www.theguardian.com/business/2017/jul/05/volvo-cars-electric-hybrid-2019

8. *TESLA Model 3*. (no year given). Available at: https://twitter.com/elonmusk/status/881751358407299072?lang=en

9. *WORLD Power Consumption. Electricity Consumption. Enerdata*. (no year given). (seen on August 20, 2017). Available at: https://yearbook.enerdata.net/electricity/electricity-domestic-consumption-data.html

10. WEBBER, R. (2017). E. Photovoltaics Moving into the Terawatt Age. In: *Plenary Presentation for SPIE Optics + Photonics*. Available at: http://spie.org/spietv?video=5547205153001&SSO=1

11. *OLED Lighting Opportunities 2017–2027: Forecasts, Technologies, Players: IDTechEx*. (no year given). (seen on August 07, 2017). Available at: http://www.idtechex.com/research/reports/oled-lighting-opportunities-2017-2027-forecasts-technologies-players-000526.asp

12. TSUJIMURA, T. (2017). *OLED Display Fundamentals and Applications*. 312 pp. ISBN: 1119187311

13. GHOSH, A.P., GERENSER, L.J., JARMAN, C.M., FORNALIK, J.E. (2005). Thin-Film Encapsulation of Organic Light-Emitting Devices. In: *Applied Physics Letters*. 2005, vol. 86, 223503. Available at: http://aip.scitation.org/doi/10.1063/1.1929867

14. PLANCK, M. (1914). The Theory of Heat Radiation (edition of 1914). Open Library. (seen on August 07, 2017). Available at: https://openlibrary.org/books/OL7154661M/The_theory_of_heat_radiation

15. EINSTEIN, A. (1905). Über einen die Erzeugung und Verwandlung des Lichtes betreffenden heuristischen Gesichtspunkt. In: *Annalen der Physik*. 1905, vol. 322, 132–148. Available at: http://doi.wiley.com/10.1002/andp.19053220607

16. BOHR, N. (1913). On the Constitution of Atoms and Molecules. In: *Philosophical Magazine Series 6*. 1913, vol. 26, 1–25. Available at: http://www.tandfonline.com/doi/abs/10.1080/14786441308634955

17. SASABE, H., KIDO, J. (2013). Development of High Performance OLEDs for General Lighting. In: *Journal of Materials Chemistry C*. 2013, vol. 1, 1699. Available at: http://xlink.rsc.org/?DOI=c2tc00584k

18. BAIGENT, D.R. et al. (1994). Conjugated Polymer Light-Emitting Diodes on Silicon Substrates. In: *Applied Physics Letters*. 1994, vol. 65, 2636–2638. Available at: http://aip.scitation.org/doi/10.1063/1.112587

19. BALDO, M.A. et al. (1998). Highly Efficient Phosphorescent Emission from Organic Electroluminescent Devices. In: *Nature*. 1998, vol. 395, 151–154. Available at: http://www.nature.com/doifinder/10.1038/25954

20. KAPPAUN, S., SLUGOVC, C., LIST, E.J.W. (2008). Phosphorescent Organic Light-Emitting Devices: Working Principle and Iridium Based Emitter Materials. In: *International Journal of Molecular Sciences*. 2008, vol. 9, 1527–1547. Available at: http://www.mdpi.com/1422-0067/9/8/1527/

21. MEHATA, M.S. et al. (2015). Spin Mixed Charge Transfer States of Iridium Complex Ir(ppy): Transient Absorption and Time-Resolved Photoluminescence. In: *RSC Advances*. 2015, vol. 5, 34094–34099. Available at: http://xlink.rsc.org/?DOI=C5RA01404B

22. FÖRSTER, T. (1948). Zwischenmolekulare Energiewanderung und Fluoreszenz. In: *Annalen der Physik*. 1948, vol. 437, 55–75. Available at: http://doi.wiley.com/10.1002/andp.19484370105

23. DEXTER, D.L. (1953). A Theory of Sensitized Luminescence in Solids. In: *The Journal of Chemical Physics*. 1953, vol. 21, 836–850. Available at: http://aip.scitation.org/doi/10.1063/1.1699044

24. PARKER, C.A., HATCHARD, C.G. (1961). Triplet-Singlet Emission in Fluid Solutions. Phosphorescence of Eosin. In: *Transactions of the Faraday Society*. 1961, vol. 57, 1894. Available at: http://xlink.rsc.org/?DOI=tf9615701894

25. UOYAMA, H., GOUSHI, K., SHIZU, K., NOMURA, H., ADACHI, C. (2012). Highly Efficient Organic Light-Emitting Diodes from Delayed Fluorescence. In: *Nature*. 2012, vol. 492, 234–238. Available at: http://www.nature.com/doifinder/10.1038/nature11687

26. CHO, Y.J., JEON, S.K., LEE, J.Y. (2016). Molecular Engineering of High Efficiency and Long Lifetime Blue Thermally Activated Delayed Fluorescent Emitters for Vacuum and Solution Processed Organic Light-Emitting Diodes. In: *Advanced Optical Materials*. 2016, vol. 4, 688–693. Available at: http://doi.wiley.com/10.1002/adom.201500634

27. PARK, I.S., LEE, J., YASUDA, T. (2016). High-Performance Blue Organic

Light-Emitting Diodes with 20% External Electroluminescence Quantum Efficiency Based on Pyrimidine-Containing Thermally Activated Delayed Fluorescence Emitters. In: *Journal of Materials Chemistry C*. 2016, vol. 4, 7911–7916. Available at: http://xlink.rsc.org/?DOI=C6TC02027E

28. LI, Y., XIE, G., GONG, S., WU, K., YANG, C. (2016). Dendronized Delayed Fluorescence Emitters for Non-Doped, Solution-Processed Organic Light-Emitting Diodes with High Efficiency and Low Efficiency Roll-Off Simultaneously: Two Parallel Emissive Channels. In: *Chemical Science*. 2016, vol. 7, 5441–5447. Available at: http://xlink.rsc.org/?DOI=C6SC00943C

29. CHA, S.J. et al. (2015). Efficient Deep Blue Fluorescent Emitter Showing High External Quantum Efficiency. In: *Dyes and Pigments*. 2015, vol. 120, 200–207. Available at: http://linkinghub.elsevier.com/retrieve/pii/S0143720815001424

30. KOMATSU, R., SASABE, H., SEINO, Y., NAKAO, K., KIDO, J. (2016). Light-Blue Thermally Activated Delayed Fluorescent Emitters Realizing a High External Quantum Efficiency of 25% and Unprecedented Low Drive Voltages in OLEDs. In: *Journal of Materials Chemistry C*. 2016, vol. 4, 2274–2278. Available at: http://xlink.rsc.org/?DOI=C5TC04057D

31. ZHAN, X. et al. (2016). Benzene-Cored AIEgens for Deep-Blue OLEDs: High Performance without Hole-Transporting Layers, and Unexpected Excellent Host for Orange Emission as a Side-Effect. In: *Chemical Science*. 2016, vol. 7, 4355–4363. Available at: http://xlink.rsc.org/?DOI=C6SC00559D

32. SEINO, Y., INOMATA, S., SASABE, H., PU, Y.-J., KIDO, J. (2016). High-Performance Green OLEDs Using Thermally Activated Delayed Fluorescence with a Power Efficiency of over 100 lm W −1. In: *Advanced Materials*. 2016, vol. 28, 2638–2643. Available at: http://doi.wiley.com/10.1002/adma.201503782

33. PARK, I.S., KOMIYAMA, H., YASUDA, T. (2016). Pyrimidine-Based Twisted Donor–Acceptor Delayed Fluorescence Molecules: a New Universal Platform for Highly Efficient Blue Electroluminescence. In: *Chemical Science*. 2016, vol. 51, 913. Available at: http://xlink.rsc.org/?DOI=C6SC03793C

34. SUN, J.W. et al. (2015). Thermally Activated Delayed Fluorescence from Azasiline Based Intramolecular Charge-Transfer Emitter (DTPDDA) and a Highly Efficient Blue Light Emitting Diode. In: *Chemistry of Materials*. 2015, vol. 27, 6675–6681. Available at: http://pubs.acs.org/doi/10.1021/acs.chemmater.5b02515

35. KAN, W., DUAN, C., SUN, M., HAN, C., XU, H. (2016). Dual Encapsulation of Electron Transporting Materials to Simplify High-Efficiency Blue Thermally Activated Delayed Fluorescence Devices. In: *Chemistry of Materials*. 2016, vol. 28, 7145–7157. Available at: http://pubs.acs.org/doi/abs/10.1021/acs.chemmater.6b03518

36. LIU, X.-Y. et al. (2016). An Effective Host Material with Thermally Activated Delayed Fluorescence Formed by Confined Conjugation for Red Phosphorescent Organic Light-Emitting Diodes. In: *Chemical Communications*. 2016, vol. 52, 8149–8151. Available at: http://xlink.rsc.org/?DOI=C6CC02856J

37. LI, Y. et al. (2016). Design Strategy of Blue and Yellow Thermally Activated Delayed Fluorescence Emitters and Their All-Fluorescence White OLEDs with

External Quantum Efficiency beyond 20%. In: *Advanced Functional Materials*. 2016, vol. 26, 6904–6912. Available at: http://doi.wiley.com/10.1002/adfm.201602507

38. SAMANTA, P.K., KIM, D., COROPCEANU, V., BRÉDAS, J.-L. (2017). Up-Conversion Intersystem Crossing Rates in Organic Emitters for Thermally Activated Delayed Fluorescence: Impact of the Nature of Singlet vs Triplet Excited States. In: *Journal of the American Chemical Society*. 2017, vol. 139, 4042–4051. Available at: http://pubs.acs.org/doi/abs/10.1021/jacs.6b12124

39. SUN, H. et al. (2017). Impact of Dielectric Constant on the Singlet–Triplet Gap in Thermally Activated Delayed Fluorescence Materials. In: *The Journal of Physical Chemistry Letters*. 2017, vol. 8, 2393–2398. Available at: http://pubs.acs.org/doi/abs/10.1021/acs.jpclett.7b00688

40. SUN, H., ZHONG, C., BRÉDAS, J.-L. (2015). Reliable Prediction with Tuned Range-Separated Functionals of the Singlet–Triplet Gap in Organic Emitters for Thermally Activated Delayed Fluorescence. In: *Journal of Chemical Theory and Computation*. 2015, vol. 11, 3851–3858. Available at: http://pubs.acs.org/doi/abs/10.1021/acs.jctc.5b00431

41. HONG, M., RAVVA, M.K., WINGET, P., BRÉDAS, J.-L. (2016). Effect of Substituents on the Electronic Structure and Degradation Process in Carbazole Derivatives for Blue OLED Host Materials. In: *Chemistry of Materials*. 2016, vol. 28, 5791–5798. Available from: http://pubs.acs.org/doi/abs/10.1021/acs.chemmater.6b02069

42. HUANG, S. et al. (2013). Computational Prediction for Singlet- and Triplet-Transition Energies of Charge-Transfer Compounds. In: *Journal of Chemical Theory and Computation*. 2013, vol. 9, 3872–3877. Available at: http://pubs.acs.org/doi/abs/10.1021/ct400415r

43. GIBSON, J., MONKMAN, A.P., PENFOLD, T.J. (2016). The Importance of Vibronic Coupling for Efficient Reverse Intersystem Crossing in Thermally Activated Delayed Fluorescence Molecules. In: *ChemPhysChem*. 2016, vol. 17, 2956–2961. Available at: http://doi.wiley.com/10.1002/cphc.201600662

44. PENFOLD, T.J. (2015). On Predicting the Excited-State Properties of Thermally Activated Delayed Fluorescence Emitters. In: *The Journal of Physical Chemistry C*. 2015, vol. 119, 13535–13544. Available at: http://pubs.acs.org/doi/abs/10.1021/acs.jpcc.5b03530

45. DIAS, F.B. et al. (2013). Triplet Harvesting with 100% Efficiency by Way of Thermally Activated Delayed Fluorescence in Charge Transfer OLED Emitters. In: *Advanced Materials*. 2013, vol. 25, 3707–3714. Available at: http://www.ncbi.nlm.nih.gov/pubmed/23703877

46. DIAS, F.B. et al. (2016). The Role of Local Triplet Excited States and D–A Relative Orientation in Thermally Activated Delayed Fluorescence: Photophysics and Devices. In: *Advanced Science*. 2016, vol. 3, 1600080. Available at: http://doi.wiley.com/10.1002/advs.201600080

47. WARD, J.S. et al. (2016). The Interplay of Thermally Activated Delayed Fluorescence (TADF) and Room Temperature Organic Phosphorescence in Sterically-Constrained Donor–Acceptor Charge-Transfer Molecules. In: *Chemical*

Communications. 2016, vol. 52, 2612–2615. Available at: http://xlink.rsc.org/?DOI=C5CC09645F

48. SANTOS, P.L. et al. (2016). Engineering the Singlet–Triplet Energy Splitting in a TADF Molecule. In: *Journal of Materials Chemistry C*. 2016, vol. 4, 3815–3824. Available at: http://xlink.rsc.org/?DOI=C5TC03849A

49. ETHERINGTON, M.K. et al. (2017). Regio- and Conformational Isomerization Critical to Design of Efficient Thermally-Activated Delayed Fluorescence Emitters. In: *Nature Communications*. 2017, vol. 8, 14987. Available at: http://www.nature.com/doifinder/10.1038/ncomms14987

50. REN, Z. et al. (2016). Pendant Homopolymer and Copolymers as Solution-Processable Thermally Activated Delayed Fluorescence Materials for Organic Light-Emitting Diodes. In: *Macromolecules*. 2016, vol. 49, 5452–5460. Available at: http://pubs.acs.org/doi/abs/10.1021/acs.macromol.6b01216

51. DOS SANTOS, P.L., DIAS, F.B., MONKMAN, A.P. (2016). Investigation of the Mechanisms Giving Rise to TADF in Exciplex States. In: *The Journal of Physical Chemistry C*. 2016, vol. 120, 18259–18267. Available at: http://pubs.acs.org/doi/abs/10.1021/acs.jpcc.6b05198

52. ETHERINGTON, M.K., GIBSON, J., HIGGINBOTHAM, H.F., PENFOLD, T.J., MONKMAN, A.P. (2016). Revealing the Spin–Vibronic Coupling Mechanism of Thermally Activated Delayed Fluorescence. In: *Nature Communications*. 2016, vol. 7, 13680. Available at: http://www.nature.com/doifinder/10.1038/ncomms13680

53. DOS SANTOS, P.L., WARD, J.S., BRYCE, M.R., MONKMAN, A.P. (2016). Using Guest–Host Interactions to Optimize the Efficiency of TADF OLEDs. In: *The Journal of Physical Chemistry Letters*. 2016, vol. 7, 3341–3346. Available at: http://pubs.acs.org/doi/abs/10.1021/acs.jpclett.6b01542

54. HOSOKAI, T. et al. (2017). Evidence and Mechanism of Efficient Thermally Activated Delayed Fluorescence Promoted by Delocalized Excited States. In: *Science Advances*. 2017, vol. 3, e1603282. Available at: http://advances.sciencemag.org/lookup/doi/10.1126/sciadv.1603282

55. MOSS, K.C. et al. (2010). Tuning the Intramolecular Charge Transfer Emission from Deep Blue to Green in Ambipolar Systems Based on Dibenzothiophene S,S-Dioxide by Manipulation of Conjugation and Strength of the Electron Donor Units. In: *The Journal of Organic Chemistry*. 2010, vol. 75, 6771–6781. Available at: http://pubs.acs.org/doi/abs/10.1021/jo100898a

56. DIAS, F.B., PENFOLD, T.J., MONKMAN, A.P. (2017). Photophysics of Thermally Activated Delayed Fluorescence Molecules. In: *Methods and Applications in Fluorescence*. 2017, vol. 5, 12001. Available at: http://stacks.iop.org/2050-6120/5/i=1/a=012001?key=crossref.38b31f1c4db7cb92259d9cded9377b3d

57. JANKUS, V. et al. (2014). Highly Efficient TADF OLEDs: How the Emitter-Host Interaction Controls both the Excited State Species and Electrical Properties of the Devices to Achieve near 100% Triplet Harvesting and High Efficiency. In: *Advanced Functional Materials*. 2014, vol. 24, 6178–6186. Available at: http://doi.wiley.com/10.1002/adfm.201400948

58. LAKOWICZ, J.R. (2006). *Principles of Fluorescence Spectroscopy*. Boston, MA: Springer US. 1–954 pp. ISBN 978-0-387-31278-1

59. VALEUR, B. (2001). *Molecular Fluorescence*. Weinheim, FRG: Wiley-VCH Verlag GmbH. 402 pp. ISBN 352729919X

60. TURRO, N.J., RAMAMURTHY, V., SCAIANO, J.C. (2009). *Principles of Molecular Photochemistry: an Introduction*. University Science Books. 495 pp. ISBN 1891389572

61. LI, C. et al. (2016). Efficient Deep-Blue OLEDs Based on Phenanthro[9,10-d]Imidazole-Containing Emitters with AIE and Bipolar Transporting Properties. In: *Journal of Materials Chemistry C*. 2016, vol. 4, 10120–10129. Available at: http://pubs.rsc.org/en/Content/ArticleLanding/2016/TC/C6TC03923E

62. GODUMALA, M., CHOI, S., CHO, M.J., CHOI, D.H. (2016). Thermally Activated Delayed Fluorescence Blue Dopants and Hosts: from the Design Strategy to Organic Light-Emitting Diode Applications. In: *Journal of Materials Chemistry C*. 2016, vol. 4, 11355–11381. Available at: http://xlink.rsc.org/?DOI=C6TC04377A

63. CHA, J.-R., LEE, C.-W., GONG, M.-S. (2015). All Fused Ring Spiro Host and Dopant Materials for Efficient Blue Fluorescent Organic Light-Emitting Diodes. In: *Dyes and Pigments*. 2015, vol. 120, 251–257. Available at: http://dx.doi.org/10.1016/j.dyepig.2015.04.023

64. DUAN, L., QIAO, J., SUN, Y., QIU, Y. Strategies to Design Bipolar Small Molecules for OLEDs: Donor–Acceptor Structure and Non-Donor–Acceptor Structure. In: *Advanced Materials*. 2011, vol. 23, 1137–1144. Available at: http://doi.wiley.com/10.1002/adma.201003816

65. ZHANG, L. et al. (2016). Highly Efficient Blue Phosphorescent Organic Light-Emitting Diodes Employing a Host Material with Small Bandgap. In: *ACS Applied Materials & Interfaces*. 2016, vol. 8, 16186–16191. Available at: http://pubs.acs.org/doi/10.1021/acsami.6b01304

66. ROTHMANN, M.M. et al. (2010). Donor-Substituted 1,3,5-Triazines as Host Materials for Blue Phosphorescent Organic Light-Emitting Diodes. *Chemistry of Materials*. vol. 22, 2403–2410. Available at: http://pubs.acs.org/doi/abs/10.1021/cm9033879

67. AN, Z.-F. et al. (2011). Conjugated Asymmetric Donor-Substituted 1,3,5-Triazines: New Host Materials for Blue Phosphorescent Organic Light-Emitting Diodes. In: *Chemistry – A European Journal*. 2011, vol. 17, 10871–10878. Available at: http://doi.wiley.com/10.1002/chem.201101118

68. SON, K.S., YAHIRO, M., IMAI, T., YOSHIZAKI, H., ADACHI, C. (2008). Analyzing Bipolar Carrier Transport Characteristics of Diarylamino-Substituted Heterocyclic Compounds in Organic Light-Emitting Diodes by Probing Electroluminescence Spectra. In: *Chemistry of Materials*. 2008. vol. 20, 4439–4446. Available at: http://pubs.acs.org/doi/abs/10.1021/cm8004985

69. WANG, Y.-K. et al. (2016). Thermally Activated Delayed Fluorescence Material as Host with Novel Spiro-Based Skeleton for High Power Efficiency and Low Roll-Off Blue and White Phosphorescent Devices. In: *Advanced Functional Materials*. Available at: http://doi.wiley.com/10.1002/adfm.201603654

70. KIM, M., JEON, S.K., HWANG, S.-H., LEE, J.Y. (2015). Bicarbazole Based Donor–Acceptor Compound as a Host for Thermally Activated Delayed Fluorescent Emitter. In: *Synthetic Metals*. 2015, vol. 209, 19–23.

71. CHOU, H.-H., CHENG, C.-H. (2010). A Highly Efficient Universal Bipolar Host for Blue, Green, and Red Phosphorescent OLEDs. In: *Advanced Materials*. 2010, vol. 22, 2468–2471. Available at: http://doi.wiley.com/10.1002/adma.201000061

72. LEE, D.R. et al. (2015). Above 30% External Quantum Efficiency in Green Delayed Fluorescent Organic Light-Emitting Diodes. In: *ACS Applied Materials & Interfaces*. 2015, vol. 7, 9625–9629. Available at: http://pubs.acs.org/doi/abs/10.1021/acsami.5b01220

73. GONG, S. et al. (2011). Highly Efficient Deep-Blue Electrophosphorescence Enabled by Solution-Processed Bipolar Tetraarylsilane Host with both a High Triplet Energy and a High-Lying HOMO Level. In: *Advanced Materials*. 2011, vol. 23, 4956–4959. Available at: http://doi.wiley.com/10.1002/adma.201102758

74. WANG, C. et al. (2016). A Bipolar and Small Singlet–Triplet Splitting Energy Host with Triplet Energy Lower Than a Blue Phosphor for Phosphorescent OLEDs in Panchromatic Range. In: *Chinese Journal of Chemistry*. 2016, vol. 34, 763–770. Available at: http://doi.wiley.com/10.1002/cjoc.201600147

75. ZENG, L., LEE, T.Y.-H., MERKEL, P.B., CHEN, S.H. (2009). A New Class of Non-Conjugated Bipolar Hybrid Hosts for Phosphorescent Organic Light-Emitting Diodes. In: *Journal of Materials Chemistry*. 2009, vol. 19, 8772. Available at: http://xlink.rsc.org/?DOI=b909787b

76. WAGNER, D. et al. (2013). Triazine Based Bipolar Host Materials for Blue Phosphorescent OLEDs. In: *Chemistry of Materials*. 2013, vol. 25, 3758–3765. Available at: http://pubs.acs.org/doi/abs/10.1021/cm4023216

77. LIN, C.-C. et al. (2017). Molecular Design of Highly Efficient Thermally Activated Delayed Fluorescence Hosts for Blue Phosphorescent and Fluorescent Organic Light-Emitting Diodes. in: *Chemistry of Materials*. 2017, vol. 29, 1527–1537. Available at: http://pubs.acs.org/doi/abs/10.1021/acs.chemmater.6b03979

78. HUANG, B. et al. (2014). A Novel, Bipolar Host Based on Triazine for Efficient Solution-Processed Single-Layer Green Phosphorescent Organic Light-Emitting Diodes. In: *Dyes and Pigments*. 2014, vol. 101, 9–14. Available at: http://linkinghub.elsevier.com/retrieve/pii/S0143720813003422

79. KIM, M., JEON, S.K., HWANG, S.-H., LEE, J.Y. (2015). Molecular Design of Triazine and Carbazole Based Host Materials for Blue Phosphorescent Organic Emitting Diodes. In: *Physical Chemistry Chemical Physics*. 2015, vol. 17, 13553–13558. Available at: http://xlink.rsc.org/?DOI=C5CP01676B

80. LIANG, K. et al. (2016). Theoretical Investigation of the Singlet–Triplet Splittings for Carbazole-Based Thermally Activated Delayed Fluorescence Emitters. In: *Physical Chemistry Chemical Physics*. 2016, vol. 18, 26623–26629. Available at: http://xlink.rsc.org/?DOI=C6CP04545F

81. ALBRECHT, K., MATSUOKA, K., FUJITA, K., YAMAMOTO, K. (2015). Carbazole Dendrimers as Solution-Processable Thermally Activated Delayed-

Fluorescence Materials. In: *Angewandte Chemie International Edition*. 2015, vol. 54, 5677–5682. Available at: http://doi.wiley.com/10.1002/anie.201500203

82. LI, J., DONG, S.-C., OPITZ, A., LIAO, L.-S., KOCH, N. (2017). Design Principles of Carbazole/Dibenzothiophene Derivatives as Host Material in Modern Efficient Organic Light-Emitting Diodes. In: *Journal of Materials Chemistry C*. 2017, vol. 90, 203512. Available at: http://xlink.rsc.org/?DOI=C7TC02248D

83. CHA, J.-R., LEE, C.W., LEE, J.Y., GONG, M.-S. (2016). Design of Ortho-Linkage Carbazole-Triazine Structure for High-Efficiency Blue Thermally Activated Delayed Fluorescent Emitters. In: *Dyes and Pigments*. 2016, vol. 134, 562–568. Available at: http://linkinghub.elsevier.com/retrieve/pii/S0143720816304259

84. BAN, X. et al. (2016). Self-Host Thermally Activated Delayed Fluorescent Dendrimers with Flexible Chains: an Effective Strategy for Non-Doped Electroluminescent Devices Based On Solution Processing. In: *Journal of Materials Chemistry C*. 2016, vol. 4, 8810–8816. Available at: http://xlink.rsc.org/?DOI=C6TC03063G

85. FAN, S. et al. (2016). A Bipolar Emitting Material for High Efficient Non-Doped Fluorescent Organic Light-Emitting Diode Approaching Standard Deep Blue. In: *Dyes and Pigments*. 2016, vol. 129, 34–42. Available at: http://linkinghub.elsevier.com/retrieve/pii/S0143720816300249

86. PARK, W.J. et al. (2015). Effective Thermally Activated Delayed Fluorescence Emitter and Its Performance in OLED Device. In: *Synthetic Metals*. 2015, vol. 209, 99–104.

87. YOO, S.G., SONG, W., LEE, J.Y. (2016). Molecular Engineering of Donor Moiety of Donor–Acceptor Structure for Management of Photophysical Properties and Device Performances. In: *Dyes and Pigments*. 2016, vol. 128, 201–208.

88. IM, J.B., LAMPANDE, R., KIM, G.H., LEE, J.Y., KWON, J.H. (2017). Thermally Activated Delayed Fluorescence Behavior Investigation in the Different Polarity Acceptor and Donor Molecules. In: *The Journal of Physical Chemistry C*. 2017, vol. 121, 1305–1314. Available from: http://pubs.acs.org/doi/abs/10.1021/acs.jpcc.6b10854

89. SHIZU, K. et al. (2015). Meta-Linking Strategy for Thermally Activated Delayed Fluorescence Emitters with a Small Singlet-Triplet Energy Gap. In: *ITE Transactions on Media Technology and Applications*. 2015, vol. 3, 108–113. Available at: https://www.jstage.jst.go.jp/article/mta/3/2/3_108/_pdf

90. MÉHES, G., GOUSHI, K., POTSCAVAGE, W.J., ADACHI, C. (2014). Influence of Host Matrix on Thermally-Activated Delayed Fluorescence: Effects on Emission Lifetime, Photoluminescence Quantum Yield, and Device Performance. In: *Organic Electronics*. 2014, vol. 15, 2027–2037. Available at: http://linkinghub.elsevier.com/retrieve/pii/S1566119914002067

91. MARIAN, C.M. (2016). Mechanism of the Triplet-to-Singlet Upconversion in the Assistant Dopant ACRXTN. In: *The Journal of Physical Chemistry C*. 2016, vol. 120, 3715–3721. Available at:

http://pubs.acs.org/doi/abs/10.1021/acs.jpcc.6b00060

92. PAN, K.-C. et al. (2016). Efficient and Tunable Thermally Activated Delayed Fluorescence Emitters Having Orientation-Adjustable CN-Substituted Pyridine and Pyrimidine Acceptor Units. In: *Advanced Functional Materials*. 2016, Available at: http://doi.wiley.com/10.1002/adfm.201602501

93. KIM, J.H., EUM, M., KIM, T.H., LEE, J.Y. (2017). A Novel Pyrrolocarbazole Donor for Stable and Highly Efficient Thermally Activated Delayed Fluorescent Emitters. In: *Dyes and Pigments*. 2017, vol. 136, 529–534.

94. RAJAMALLI, P. et al. (2016). A Method for Reducing the Singlet–Triplet Energy Gaps of TADF Materials for Improving the Blue OLED Efficiency. In: *ACS Applied Materials & Interfaces*. 2016, acsami.6b10678. Available at: http://pubs.acs.org/doi/abs/10.1021/acsami.6b10678

95. BERGMANN, L., ZINK, D.M., BRÄSE, S., BAUMANN, T., VOLZ, D. (2016). Metal–Organic and Organic TADF-Materials: Status, Challenges and Characterization. In: *Topics in Current Chemistry*. 2016, vol. 374, 22. Available at: http://link.springer.com/10.1007/s41061-016-0022-6

96. LIN, T.-A. et al. (2016). Sky-Blue Organic Light Emitting Diode with 37% External Quantum Efficiency Using Thermally Activated Delayed Fluorescence from Spiroacridine-Triazine Hybrid. In: *Advanced Materials*. 2016, vol. 28, 6976–6983. Available at: http://doi.wiley.com/10.1002/adma.201601675

97. WANG, Y. et al. (2016). Engineering the Interconnecting Position of Star-Shaped Donor-π-Acceptor Molecules Based on Triazine, Spirofluorene, and Triphenylamine Moieties for Color Tuning from Deep Blue to Green. In: *Chemistry – An Asian Journal*. 2016, vol. 11, 2555–2563. Available at: http://doi.wiley.com/10.1002/asia.201600727

98. TANAKA, H., SHIZU, K., NAKANOTANI, H., ADACHI, C. (2014). Dual Intramolecular Charge-Transfer Fluorescence Derived from a Phenothiazine-Triphenyltriazine Derivative. In: *The Journal of Physical Chemistry C*. 2014, vol. 118, 15985–15994. Available at: http://pubs.acs.org/doi/abs/10.1021/jp501017f

99. XIAO, J., LIU, X.-K., WANG, X.-X., ZHENG, C.-J., LI, F. (2014). Tailoring Electronic Structure of Organic Host for High-Performance Phosphorescent Organic Light-Emitting Diodes. In: *Organic Electronics*. 2014, vol. 15, 2763–2768. Available at: http://linkinghub.elsevier.com/retrieve/pii/S1566119914003243

100. CHEN, D.-Y. et al. (2016). Isomeric Thermally Activated Delayed Fluorescence Emitters for Color Purity-Improved Emission in Organic Light-Emitting Devices. In: *ACS Applied Materials & Interfaces*. 2016, vol. 8, 16791–16798. Available at: http://pubs.acs.org/doi/10.1021/acsami.6b03954

101. CHEN, W.-C., LEE, C.-S., TONG, Q.-X. (2015). Blue-Emitting Organic Electrofluorescence Materials: Progress and Prospective. In: *Journal of Materials Chemistry C*. 2015, vol. 3, 10957–10963. Available at: http://xlink.rsc.org/?DOI=C5TC02420J

102. GUO, K. et al. (2017). Stable Green Phosphorescence Organic Light-Emitting Diodes with Low Efficiency Roll-off Using a Novel Bipolar Thermally Activated Delayed Fluorescence Material as Host. In: *Chemical Science*. 2017,

vol. 8, 1259–1268. Available at: http://xlink.rsc.org/?DOI=C6SC03008D

103. NODA, H., KABE, R., ADACHI, C. (2016). Blue Thermally Activated Delayed Fluorescence Molecule Having Acridane and Cyanobenzene Units. In: *Chemistry Letters*. 2016, vol. 45, 1463–1466. Available at: http://www.journal.csj.jp/doi/10.1246/cl.160814

104. LI, B. et al. (2014). Dicarbazolyldicyanobenzenes as Thermally Activated Delayed Fluorescence Emitters: Effect of Substitution Position on Photoluminescent and Electroluminescent Properties. In: *Chemistry Letters*. 2014, vol. 43, 319–321. Available at: http://www.journal.csj.jp/doi/10.1246/cl.130907

105. CHEN, T. et al. (2015). Understanding the Control of Singlet–Triplet Splitting for Organic Exciton Manipulating: A Combined Theoretical and Experimental Approach. In: *Scientific Reports*. 2015, vol. 5, 10923. Available at: http://www.nature.com/articles/srep10923

106. GUO, J. et al. (2017). Robust Luminescent Materials with Prominent Aggregation-Induced Emission and Thermally Activated Delayed Fluorescence for High-Performance Organic Light-Emitting Diodes. In: *Chemistry of Materials*. 2017, vol. 29, 3623–3631. Available at: http://pubs.acs.org/doi/abs/10.1021/acs.chemmater.7b00450

107. PARK, I.S., LEE, S.Y., ADACHI, C., YASUDA, T. (2016). Full-Color Delayed Fluorescence Materials Based on Wedge-Shaped Phthalonitriles and Dicyanopyrazines: Systematic Design, Tunable Photophysical Properties, and OLED Performance. In: *Advanced Functional Materials*. 2016, vol. 26, 1813–1821. Available at: http://doi.wiley.com/10.1002/adfm.201505106

108. WANG, S. et al. (2015). Achieving High Power Efficiency and Low Roll-Off OLEDs Based on Energy Transfer from Thermally Activated Delayed Excitons to Fluorescent Dopants. In: *Chemical Communications*. 2015, vol. 51, 11972–11975. Available at: http://xlink.rsc.org/?DOI=C5CC04469C

109. CHANG, C.-H. et al. (2012). A Dicarbazole–Triazine Hybrid Bipolar Host Material for Highly Efficient Green Phosphorescent OLEDs. In: *Journal of Materials Chemistry*. 2012, vol. 22, 3832. Available at: http://xlink.rsc.org/?DOI=c2jm14686j

110. INOMATA, H. et al. (2004). High-Efficiency Organic Electrophosphorescent Diodes Using 1,3,5-Triazine Electron Transport Materials. In: *Chemistry of Materials*. 2004, vol. 16, 1285–1291. Available at: http://pubs.acs.org/doi/abs/10.1021/cm034689t

111. ROTHMANN, M.M. et al. (2011). Designing a Bipolar Host Material for Blue Phosphorescent OLEDs: Phenoxy-Carbazole Substituted Triazine. In: *Organic Electronics*. 2011, vol. 12, 1192–1197. Available at: http://linkinghub.elsevier.com/retrieve/pii/S1566119911001236

112. SEREVIČIUS, T. et al. (2013). Enhanced Electroluminescence Based on Thermally Activated Delayed Fluorescence from a Carbazole–Triazine Derivative. In: *Physical Chemistry Chemical Physics*. 2013, vol. 15, 15850. Available at: http://xlink.rsc.org/?DOI=c3cp52255e

113. LIU, X.-K. et al. (2012). Novel Bipolar Host Materials Based on 1,3,5-Triazine Derivatives for Highly Efficient Phosphorescent OLEDs with Extremely

Low Efficiency Roll-off. In: *Physical Chemistry Chemical Physics*. 2012, vol. 14, 14255. Available at: http://xlink.rsc.org/?DOI=c2cp41542a

114. XU, F., WANG, Z., GONG, Q. (2007). Synthesis, Characterization, and Optical Properties of Two-Photon-Absorbing Octupolar Molecule with an s-Triazine Core. In: *Optical Materials*. 2007, vol. 29, 723–727. Available at: http://linkinghub.elsevier.com/retrieve/pii/S0925346705005197

115. JIANG, Y. et al. (2011). Synthesis, Two-Photon Absorption and Optical Limiting Properties of Multi-branched Styryl Derivatives Based on 1,3,5-Triazine. In: *Chemistry – An Asian Journal*. 2011, vol. 6, 157–165. Available at: http://doi.wiley.com/10.1002/asia.201000536

116. MAITI, S.K. et al. (2013). Divergent Route to the Preparation of Hybrid Pt–Fe 2,4,6-Tris(4-ethynyl)phenyl-1,3,5-triazine Metallodendrimers for Nonlinear Optics. In: *Organometallics*. 2013, vol. 32, 406–414. Available at: http://pubs.acs.org/doi/abs/10.1021/om300745v

117. LIU, R. et al. (2017). Star-Shaped D-π-A Compounds with a 1,3,5-Triazine Core and N-Aryl Chromophore Substituted Fluorene Arms: Synthesis, aggregation induced emission and two-photon absorption. In: *Dyes and Pigments*. 2017, vol. 137, 174–181. Available at: http://linkinghub.elsevier.com/retrieve/pii/S014372081630941X

118. SU, S.-J., CAI, C., TAKAMATSU, J., KIDO, J. (2012). A Host Material with a Small Singlet–Triplet Exchange Energy for Phosphorescent Organic Light-Emitting Diodes: Guest, Host, and Exciplex Emission. In: *Organic Electronics*. 2012, vol. 13, 1937–1947. Available at: http://linkinghub.elsevier.com/retrieve/pii/S1566119912002625

119. LI, W., LI, J., LIU, D., WANG, F., ZHANG, S. (2015). Bipolar Host Materials for High-Efficiency Blue Phosphorescent and Delayed-Fluorescence OLEDs. In: *Journal of Materials Chemistry C*. 2015, vol. 3, 12529–12538. Available at: http://xlink.rsc.org/?DOI=C5TC02997J

120. DENG, L., LI, J., WANG, G.-X., WU, L.-Z. (2013). Simple Bipolar Host Materials Incorporating CN Group for Highly Efficient Blue Electrophosphorescence with Slow Efficiency Roll-off. In: *Journal of Materials Chemistry C*. 2013, vol. 1, 8140. Available at: http://xlink.rsc.org/?DOI=c3tc31893a

121. KIM, M., JEON, S.K., HWANG, S.-H., LEE, J.Y. (2015). Stable Blue Thermally Activated Delayed Fluorescent Organic Light-Emitting Diodes with Three Times Longer Lifetime than Phosphorescent Organic Light-Emitting Diodes. In: *Advanced Materials*. 2015, vol. 27, 2515–2520. Available at: http://doi.wiley.com/10.1002/adma.201500267

122. LEE, D.R. et al. (2015). Design Strategy for 25% External Quantum Efficiency in Green and Blue Thermally Activated Delayed Fluorescent Devices. In: *Advanced Materials*. 2015, vol. 27, 5861–5867. Available at: http://doi.wiley.com/10.1002/adma.201502053

123. CHO, Y.J., JEON, S.K., LEE, S.-S., YU, E., LEE, J.Y. (2016). Donor Interlocked Molecular Design for Fluorescence-like Narrow Emission in Deep Blue Thermally Activated Delayed Fluorescent Emitters. In: *Chemistry of*

Materials. 2016, vol. 28, 5400–5405. Available at: http://pubs.acs.org/doi/abs/10.1021/acs.chemmater.6b01484

124. TSAI, W.-L. et al. (2015). A Versatile Thermally Activated Delayed Fluorescence Emitter for both Highly Efficient Doped and Non-Doped Organic Light Emitting Devices. In: *Chemical Communications.* 2015, vol. 51, 13662–13665. Available at: http://xlink.rsc.org/?DOI=C5CC05022G

125. WONG, M.Y., ZYSMAN-COLMAN, E. (2017). Purely Organic Thermally Activated Delayed Fluorescence Materials for Organic Light-Emitting Diodes. In: *Advanced Materials.* 2017, vol. 29, 1605444. Available at: http://doi.wiley.com/10.1002/adma.201605444

126. DE MELLO, J.C., WITTMANN, H.F., FRIEND, R.H. (1997). An Improved Experimental Determination of External Photoluminescence Quantum Efficiency. In: *Advanced Materials.* 1997, vol. 9, 230–232. Available at: http://doi.wiley.com/10.1002/adma.19970090308

127. MIYAMOTO, E., YAMAGUCHI, Y., YOKOYAMA, M. (1989). Ionization Potential of Organic Pigment Film by Atmospheric Photoelectron Emission Analysis. In: *Electrophotography.* 1989, vol. 28, 364–370. Available at: https://www.jstage.jst.go.jp/article/isjepj/28/4/28_4_364/_article

128. MONTRIMAS, E., GAIDELIS, V., PAZERA, A. (1966). The Discharge Kinetics of Negatively Charged Se Electrophotographic Layers. In: *Lithuanian Journal of Physics.* 1966, vol. 6, 569–576. Available at: http://www.scopus.com/record/display.url?eid=2-s2.0-0011180578&origin=inward&txGid=65AF7BE39D87CF06CB8F7AFB6C2F6561.I0QkgbIjGqqLQ4Nw7dqZ4A:2

129. VAEZI-NEJAD, S.M. (1987). Xerographic Time of Flight Experiment for the Determination of Drift Mobility in High Resistivity Semiconductors. In: *International Journal of Electronics.* 1987, vol. 62, 361–384. Available at: http://www.tandfonline.com/doi/abs/10.1080/00207218708920988

130. REGHU, R.R. et al. (2012). Glass-Forming Carbazolyl and Phenothiazinyl Tetra Substituted Pyrene Derivatives: Photophysical, Electrochemical, and Photoelectrical Properties. In: *The Journal of Physical Chemistry C.* 2012, vol. 116, 15878–15887. Available at: http://pubs.acs.org/doi/abs/10.1021/jp3019952

131. VAJIRAVELU, S. et al. (2009). Effect of Substituents on the Electron Transport Properties of Bay Substituted Perylene Diimide Derivatives. In: *Journal of Materials Chemistry.* 2009, vol. 19, 4268. Available at: http://xlink.rsc.org/?DOI=b901847f

132. GENEVIČIUS, K., ÖSTERBACKA, R., JUŠKA, G., ARLAUSKAS, K., STUBB, H. (2002). Charge Transport in π-Conjugated Polymers from Extraction Current Transients. In: *Thin Solid Films.* 2002, vols. 403–404, 415–418. Available at: http://linkinghub.elsevier.com/retrieve/pii/S0040609001015838

133. FRISCH, M.J. et al. (2009). *Gaussian Citation.* Available at: http://www.gaussian.com/g_tech/g_ur/m_citation.htm

134. CALAIS, J.-L. (1993). D*ensity-Functional Theory of Atoms and Molecules.* (edited by PARR, R.G. and YANG, W.). New York, Oxford: Oxford University Press. In: *International Journal of Quantum Chemistry.* 1993, vol. 47, 101.

Available at: http://books.google.com/books?id=mGOpScSIwU4C

135. BECKE, A.D. (1993). Density-Functional Thermochemistry. III. The Role of Exact Exchange. In: *The Journal of Chemical Physics*. 1993, vol. 98, 5648–5652. Available at: http://aip.scitation.org/doi/10.1063/1.464913

136. LEE, C., YANG, W., PARR, R.G. (1988). Development of the Colle-Salvetti Correlation-Energy Formula into a Functional of the Electron Density. In: *Physical Review B*. 1988, vol. 37, 785–789. Available at: https://link.aps.org/doi/10.1103/PhysRevB.37.785

137. GROSS, E.K.U., KOHN, W. (1986). Local Density-Functional Theory of Frequency-Dependent Linear Response. In: *Physical Review Letters*. 1986, vol. 57, 2850–2852. Available at: https://journals.aps.org/prl/abstract/10.1103/PhysRevLett.55.2850

138. BAUERNSCHMITT, R., AHLRICHS, R. (1996). Treatment of Electronic Excitations within the Adiabatic Approximation of Time Dependent Density Functional Theory. In: *Chemical Physics Letters*. 1996, vol. 256, 454–464. Available at: http://linkinghub.elsevier.com/retrieve/pii/000926149600440X

139. THANTHIRIWATTE, K.S., GWALTNEY, S.R. (2006). Excitation Spectra of Dibenzoborole Containing π-Electron Systems: Controlling the Electronic Spectra by Changing the p π−π* Conjugation. In: *The Journal of Physical Chemistry A*. 2006, vol. 110, 2434–2439. Available at: http://pubs.acs.org/doi/abs/10.1021/jp0545492

140. STAROVEROV, V.N., SCUSERIA, G.E., TAO, J., PERDEW, J.P. (2003). Comparative Assessment of a New Nonempirical Density Functional: Molecules and Hydrogen-Bonded Complexes. In: *The Journal of Chemical Physics*. 2003. vol. 119, 12129–12137. Available at: http://aip.scitation.org/doi/10.1063/1.1626543

141. ZHAO, Y., TRUHLAR, D.G. (2005). Benchmark Databases for Nonbonded Interactions and Their Use to Test Density Functional Theory. In: *Journal of Chemical Theory and Computation*. 2005, vol. 1, 415–432. Available at: http://pubs.acs.org/doi/abs/10.1021/ct049851d

142. ZHAO, Y., TRUHLAR, D.G. (2008). The M06 Suite of Density Functionals for Main Group Thermochemistry, Thermochemical Kinetics, Noncovalent Interactions, Excited States, and Transition Elements: Two New Functionals and Systematic Testing of Four M06-Class Functionals and 12 Other Functions. In: *Theoretical Chemistry Accounts*. 2008, vol. 120, 215–241. Available at: http://link.springer.com/10.1007/s00214-007-0310-x

143. ZHAO, Y., TRUHLAR, D.G. (2004). Hybrid Meta Density Functional Theory Methods for Thermochemistry, Thermochemical Kinetics, and Noncovalent Interactions: The MPW1B95 and MPWB1K Models and Comparative Assessments for Hydrogen Bonding and van der Waals Interactions. In: *The Journal of Physical Chemistry A*. 2004, vol. 108, 6908–6918. Available at: http://pubs.acs.org/doi/abs/10.1021/jp048147q

144. BOESE, A.D., MARTIN, J.M.L. (2004). Development of Density Functionals for Thermochemical Kinetics. In: *The Journal of Chemical Physics*. 2004, vol. 121, 3405–3416. Available at:

http://aip.scitation.org/doi/10.1063/1.1774975

145. ZHAO, Y., TRUHLAR, D.G. (2008). Density Functionals with Broad Applicability in Chemistry. In: *Accounts of Chemical Research*. 2008, vol. 41, 157–167. Available at: http://pubs.acs.org/doi/abs/10.1021/ar700111a

146. CHAI, J.-D., HEAD-GORDON, M. (2008). Long-Range Corrected Hybrid Density Functionals with Damped Atom–Atom Dispersion Corrections. In: *Physical Chemistry Chemical Physics*. 2008, vol. 10, 6615. Available at: http://xlink.rsc.org/?DOI=b810189b

147. MARTIN, R.L. (2003). Natural Transition Orbitals. In: *The Journal of Chemical Physics*. 2003, vol. 118, 4775–4777. Available at: http://aip.scitation.org/doi/10.1063/1.1558471

148. O'BOYLE, N.M., TENDERHOLT, A.L., LANGNER, K.M. (2008). cclib: A Library for Package-Independent Computational Chemistry Algorithms. In: *Journal of Computational Chemistry*. 2008, vol. 29, 839–845. Available at: http://doi.wiley.com/10.1002/jcc.20823

149. LU, T., CHEN, F. Multiwfn: A Multifunctional Wavefunction Analyzer. In: *Journal of Computational Chemistry*. 2012, vol. 33, 580–592. Available at: http://doi.wiley.com/10.1002/jcc.22885

150. HARWOOD, L.M., MOODY, C.J. (1990). *Experimental Organic Chemistry: Principles and Practice*. Oxford: Blackwell Scientific. ISBN: 0632020164; 0632020172.

151. NEUGEBAUER, F.A., FISCHER, H. (1972). tert.-Butyl-substituierte Carbazole. In: *Chemische Berichte*. 1972, vol. 105, 2686–2693. Available at: http://doi.wiley.com/10.1002/cber.19721050829

152. BUDÉN, M.E., VAILLARD, V.A., MARTIN, S.E., ROSSI, R.A. (2009). Synthesis of Carbazoles by Intramolecular Arylation of Diarylamide Anions. In: *The Journal of Organic Chemistry*. 2009, vol. 74, 4490–4498. Available at: http://pubs.acs.org/doi/abs/10.1021/jo9006249

153. CHEN, H.-Y., CHEN, C.-T., CHEN, C.-T. (2010). Synthesis and Characterization of a New Series of Blue Fluorescent 2,6-Linked 9,10-Diphenylanthrylenephenylene Copolymers and Their Application for Polymer Light-Emitting Diodes. In: *Macromolecules*. 2010, vol. 43, 3613–3623. Available at: http://pubs.acs.org/doi/abs/10.1021/ma100195m

154. GORLUSHKO, D.A. et al. (2008). Iodination of Aryl Amines in a Water-Paste Form via Stable Aryl Diazonium Tosylates. In: *Tetrahedron Letters*. 2008, vol. 49, 1080–1082. Available at: http://linkinghub.elsevier.com/retrieve/pii/S004040390702415X

155. WANG, L. et al. (2004). Design, Synthesis, and Biological Activity of 4-[(4-Cyano-2-arylbenzyloxy)-(3-methyl-3H-imidazol-4-yl)methyl]benzonitriles as Potent and Selective Farnesyltransferase Inhibitors. In: *Journal of Medicinal Chemistry*. 2004, vol. 47, 612–626. Available at: http://pubs.acs.org/doi/abs/10.1021/jm030434f

156. UCHIYAMA, M., NAKA, H., MATSUMOTO, Y., OHWADA, T. (2004). Regio- and Chemoselective Direct Generation of Functionalized Aromatic Aluminum Compounds Using Aluminum Ate Base. In: *Journal of the American*

Chemical Society. 2004, vol. 126, 10526–10527. Available at: http://pubs.acs.org/doi/abs/10.1021/ja0473236

157. HAYAMI, S., INOUE, K. (1999). Structure and Magnetic Property of the Organic Triradical with Triazine Skeleton; 2,4,6-Tris{p-(N-oxy-N-tert-butylamino)phenyl}triazine. In: *Chemistry Letters*. 1999, vol. 28, 545–546. Available at: https://www.jstage.jst.go.jp/article/cl/28/7/28_7_545/_article

158. TUCKER, S.H. (1926). LXXIV.-Iodination in the Carbazole Series. In: *Journal of the Chemical Society (Resumed)*. 1926, vol. 129, 546. Available at: http://xlink.rsc.org/?DOI=jr9262900546

159. BEGINN, C., GRAŽULEVIČIUS, J. V., STROHRIEGL, P., SIMMERER, J., HAARER, D. (1994). Synthesis of poly(9-hexyl-3,6-carbazolyleneethynylene) and Its Model Compounds. In: *Macromolecular Chemistry and Physics*. 1994, vol. 195, 2353–2370. Available at: http://doi.wiley.com/10.1002/macp.1994.021950706

160. MANOLIKAKES, G., KNOCHEL, P. (2009). Radical Catalysis of Kumada Cross-Coupling Reactions Using Functionalized Grignard Reagents. In: *Angewandte Chemie International Edition*. 2009, vol. 48, 205–209. Available at: http://doi.wiley.com/10.1002/anie.200803730

161. WEINGARTEN, H. (1964). Ullmann Condensation. In: *The Journal of Organic Chemistry*. 1964, vol. 29, 977–978. Available at: http://pubs.acs.org/doi/abs/10.1021/jo01027a529

162. YANG, X. et al. (2008). Novel Carbazole-Based Organogels Modulated by Tert-Butyl Moieties. In: *Chemical Communications*. 2008, vol. 108, 453–455. Available at: http://xlink.rsc.org/?DOI=B713734F

163. KOELSCH, C.F., WHITNEY, A.G. (1941). The Rosenmund-von Braun Nitrile Synthesis 1. In: *The Journal of Organic Chemistry*. 1941, vol. 6, 795–803. Available at: http://pubs.acs.org/doi/abs/10.1021/jo01206a002

164. DRIVER, M.S., HARTWIG, J.F. (1996). A Second-Generation Catalyst for Aryl Halide Amination: Mixed Secondary Amines from Aryl Halides and Primary Amines Catalyzed by (DPPF)PdCl 2. In: *Journal of the American Chemical Society*. 1996, vol. 118, 7217–7218. Available at: http://pubs.acs.org/doi/abs/10.1021/ja960937t

165. MATULAITIS, T. et al. (2016). Synthesis and Properties of Bipolar Derivatives of 1,3,5-triazine and Carbazole. In: *Dyes and Pigments*. 2016, vol. 127, 45–58. Available at: http://linkinghub.elsevier.com/retrieve/pii/S0143720815004283

166. THORAND, S., KRAUSE, N. (1998). Improved Procedures for the Palladium-Catalyzed Coupling of Terminal Alkynes with Aryl Bromides (Sonogashira Coupling). In: *The Journal of Organic Chemistry*. 1998, vol. 63, 8551–8553. Available at: http://pubs.acs.org/doi/abs/10.1021/jo9808021

167. TAO, Y.-M. et al. (2011). Synthesis and Characterization of Efficient Luminescent Materials Based on 2,1,3-benzothiadiazole with Carbazole Moieties. In: *Synthetic Metals*. 2011, vol. 161, 718–723. Available at: http://dx.doi.org/10.1016/j.synthmet.2011.01.020

168. REICHARDT, C. (2002). *Solvents and Solvent Effects in Organic*

Chemistry. Weinheim, FRG: Wiley-VCH Verlag GmbH & Co. KGaA. 534 pp. ISBN: 3527306188

169. LIPPERT, E. (1955). Dipolmoment und Elektronenstruktur von angeregten Molekülen. In: *Zeitschrift für Naturforschung A*. 1955, vol. 10, 541–545. Available at: http://www.degruyter.com/view/j/zna.1955.10.issue-7/zna-1955-0707/zna-1955-0707.xml

170. MATAGA, N., KAIFU, Y., KOIZUMI, M. (1956). Solvent Effects upon Fluorescence Spectra and the Dipolemoments of Excited Molecules. In: *Bulletin of the Chemical Society of Japan*. 1956, vol. 29, 465–470. Available at: http://joi.jlc.jst.go.jp/JST.Journalarchive/bcsj1926/29.465?from=CrossRef

171. KUKHTA, N.A. et al. (2014). Effect of Linking Topology on the Properties of Star-Shaped Derivatives of Triazine and Fluorene. In: *Synthetic Metals*. 2014, vol. 195, 266–275. Available at: http://dx.doi.org/10.1016/j.synthmet.2014.06.019

172. HUANG, B. et al. (2015). Thermally Activated Delayed Fluorescence of N-phenylcarbazole and Triphenylamine Functionalised Tris(aryl)triazines. In: *Dyes and Pigments*. 2015, vol. 117, 141–148. Available at: http://linkinghub.elsevier.com/retrieve/pii/S0143720815000571

173. WANG, Q. et al. (2013). Evaluation of Propylene-, Meta-, and Para-Linked Triazine and Tert-Butyltriphenylamine as Bipolar Hosts for Phosphorescent Organic Light-Emitting Diodes. In: *Journal of Materials Chemistry C*. 2013, vol. 1, 2224. Available at: http://xlink.rsc.org/?DOI=c3tc00588g

174. BRASLAVSKY, S.E. (2007). Glossary of Terms Used in Photochemistry, 3rd edition (IUPAC Recommendations 2006). In: *Pure and Applied Chemistry*. 2007, vol. 79, 293–465. Available at: http://www.degruyter.com/view/j/pac.2007.79.issue-3/pac200779030293/pac200779030293.xml

175. AMBROSE, J.F., NELSON, R.F. (1968). Anodic Oxidation Pathways of Carbazoles. In: *Journal of The Electrochemical Society*. 1968, vol. 115, 1159. Available at: http://jes.ecsdl.org/cgi/doi/10.1149/1.2410929

176. CHIU, S.-K., CHUNG, Y.-C., LIOU, G.-S., SU, Y.O. (2012). Electrochemical and Spectral Characterizations of 9-Phenylcarbazoles. In: *Journal of the Chinese Chemical Society*. 2012, vol. 59, 331–337. Available at: http://doi.wiley.com/10.1002/jccs.201100601

177. REGHU, R.R. et al. (2013). Glass Forming Donor-Substituted s-Triazines: Photophysical and Electrochemical Properties. In: *Dyes and Pigments*. 2013, vol. 97, 412–422. Available at: http://linkinghub.elsevier.com/retrieve/pii/S0143720813000211

178. DATA, P. et al. (2014). Unusual Properties of Electropolymerized 2,7- and 3,6- carbazole Derivatives. In: *Electrochimica Acta*. 2014, vol. 128, 430–438. Available from: http://dx.doi.org/10.1016/j.electacta.2013.12.108

179. LUKEŠ, V., RAPTA, P., IDZIK, K.R., BECKERT, R., DUNSCH, L. (2011). Charged States of 1,3,5-Triazine Molecules as Models for Star-Shaped Molecular Architecture: A DFT and Spectroelectrochemical Study. In: *The Journal of Physical Chemistry B*. 2011, vol. 115, 3344–3353. Available at: http://pubs.acs.org/doi/abs/10.1021/jp111297y

180. BOS, F.C., BURLAND, D.M. Hole Transport in Polyvinylcarbazole: The Vital Importance of Excitation-Light Intensity. In: *Physical Review Letters*. 1987. vol. 58, 152–155. Available at: https://link.aps.org/doi/10.1103/PhysRevLett.58.152

181. BOLINK, H.J., SANTAMARIA, S.G., SUDHAKAR, S., ZHEN, C., SELLINGER, A. (2008). Solution Processable Phosphorescent Dendrimers Based on Cyclic Phosphazenes for Use in Organic Light Emitting Diodes (OLEDs). In: *Chemical Communications*. 2008, 618–620. Available at: http://xlink.rsc.org/?DOI=B715239F

182. YAP, C.C., YAHAYA, M., SALLEH, M.M. (2009). Influence of Tetrabutylammonium Hexafluorophosphate (TBAPF6) Doping Level on the Performance of Organic Light Emitting Diodes Based on PVK:PBD Blend Films. In: *Current Applied Physics*. 2009, vol. 9, 722–726. Available at: http://dx.doi.org/10.1016/j.cap.2008.06.013

183. HUANG, J., HOU, W.-J., LI, J.-H., LI, G., YANG, Y. (2006). Improving the Power Efficiency of White Light-Emitting Diode by Doping Electron Transport Material. In: *Applied Physics Letters*. 2006, vol. 89, 133509. Available at: http://link.aip.org/link/APPLAB/v89/i13/p133509/s1&Agg=doi

184. CÉSPEDES-GUIRAO, F.J., GARCÍA-SANTAMARÍA, S., FERNÁNDEZ-LÁZARO, F., SASTRE-SANTOS, A., BOLINK, H.J. (2009). Efficient Electroluminescence from a Perylenediimide Fluorophore Obtained from a Simple Solution Processed OLED. In: *Journal of Physics D: Applied Physics*. 2009, vol. 42, 105106. Available at: http://stacks.iop.org/0022-3727/42/i=10/a=105106?key=crossref.7f815e506cb5132fa690ba2e41baa896

185. LUSZCZYNSKA, B. et al. (2006). Poly(N-vinylcarbazole) Doped with a Pyrazoloquinoline Dye: a Deep Blue Light-Emitting Composite for Light-Emitting Diode Applications. In: *Journal of Applied Physics*. 2006, vol. 99, 24505. Available at: http://scitation.aip.org/content/aip/journal/jap/99/2/10.1063/1.2162268

186. CHERPAK, V. et al. (2015). Mixing of Phosphorescent and Exciplex Emission in Efficient Organic Electroluminescent Devices. In: *ACS Applied Materials & Interfaces*. 2015, vol. 7, 1219–1225. Available at: http://pubs.acs.org/doi/abs/10.1021/am507050g

187. SUN, J.W. et al. (2014). A Fluorescent Organic Light-Emitting Diode with 30% External Quantum Efficiency. In: *Advanced Materials*. 2014, vol. 26, 5684–5688. Available at: http://doi.wiley.com/10.1002/adma.201401407

188. STAKHIRA, P. et al. (2012). Blue Organic Light-Emitting Diodes Based on Pyrazoline Phenyl Derivative. In: *Synthetic Metals*. 2012, vol. 162, 352–355. Available at: http://dx.doi.org/10.1016/j.synthmet.2011.12.017

189. SEO, J.H. et al. (2010). Phosphorescent Organic Light-Emitting Diodes with Simplified Device Architecture. In: *Japanese Journal of Applied Physics*. 2010, vol. 49, 08JG04. Available at: http://stacks.iop.org/1347-4065/49/08JG04

190. LEE, I.-H., GONG, M.-S. (2011). New Fluorescent Blue OLED Host and Dopant Materials Based on the Spirobenzofluorene. In: *Bulletin of the Korean Chemical Society*. 2011, vol. 32, 1475–1482. Available at:

http://koreascience.or.kr/journal/view.jsp?kj=JCGMCS&py=2011&vnc=v32n5&sp=1475

191. ZHOU, X. et al. (2002). High-Efficiency Electrophosphorescent Organic Light-Emitting Diodes with Double Light-Emitting Layers. In: *Applied Physics Letters*. 2002, vol. 81, 4070. Available at: http://scitation.aip.org/content/aip/journal/apl/81/21/10.1063/1.1522495

192. IM, Y. et al. (2017). Molecular Design Strategy of Organic Thermally Activated Delayed Fluorescence Emitters. In: *Chemistry of Materials*. 2017, vol. 29, 1946–1963. Available at: http://pubs.acs.org/doi/abs/10.1021/acs.chemmater.6b05324

193. MATULAITIS, T. et al. (2017). Impact of Donor Substitution Pattern on the TADF Properties in the Carbazolyl-Substituted Triazine Derivatives. In: *The Journal of Physical Chemistry C*. acs.jpcc.7b08034. Available at: http://pubs.acs.org/doi/abs/10.1021/acs.jpcc.7b08034

194. BRÉDAS, J.-L. (2017). Organic Electronics: Does a Plot of the HOMO–LUMO Wave Functions Provide Useful Information? In: *Chemistry of Materials*. 2017, vol. 29, 477–478. Available at: http://pubs.acs.org/doi/abs/10.1021/acs.chemmater.6b04947

195. KUKHTA, N.A., DA SILVA FILHO, D.A., VOLYNIUK, D., GRAZULEVICIUS, J.V., SINI, G. (2017). Can Fluorenone-Based Compounds Emit in the Blue Region? Impact of the Conjugation Length and the Ground-State Aggregation. In: *Chemistry of Materials*. 2017, vol. 29, 1695–1707. Available at: http://pubs.acs.org/doi/abs/10.1021/acs.chemmater.6b05158

196. KIM, M., CHOI, J.M., LEE, J.Y. (2016). Simultaneous Improvement of Emission Color, Singlet–Triplet Energy Gap, and Quantum Efficiency of Blue Thermally Activated Delayed Fluorescent Emitters Using a 1-Carbazolylcarbazole Based Donor. In: *Chemical Communications*. 2016, vol. 52, 10032–10035. Available at: http://xlink.rsc.org/?DOI=C6CC04516B

197. HIRATA, S. et al. (2014). Highly Efficient Blue Electroluminescence Based on Thermally Activated Delayed Fluorescence. In: *Nature Materials*. 2014, vol. 14, 330–336. Available at: http://www.nature.com/doifinder/10.1038/nmat4154

198. CUI, L.-S. et al. (2017). Controlling Singlet–Triplet Energy Splitting for Deep-Blue Thermally Activated Delayed Fluorescence Emitters. In: *Angewandte Chemie International Edition*. 2017, vol. 56, 1571–1575. Available at: http://doi.wiley.com/10.1002/anie.201609459

199. YANG, Z. et al. (2017). Recent Advances in Organic Thermally Activated Delayed Fluorescence Materials. In: *Chemical Society Reviews*. 2017, vol. 46, 915–1016. Available at: http://xlink.rsc.org/?DOI=C6CS00368K

200. WILLIAMS, R.T., BRIDGES, J.W. (1964). Fluorescence of Solutions: A Review. In: *Journal of Clinical Pathology*. 1964, vol. 17, 371–94. Available at: http://www.ncbi.nlm.nih.gov/pubmed/14195623

201. BLUMSTEIN, R.B. (1997). Thermal Characterization of Polymeric Materials. 2nd Edition; vols. 1 & 2 Edited by TURI, E.A. (Polytechnic University, New York). San Diego: Academic Press. 1997. xxiv + 2420 pp. ISBN 0-12-703783-7. In: *Journal of the American Chemical Society*. 1997, vol. 119, 9589–

9590. Available at: http://pubs.acs.org/doi/10.1021/ja975533v

202. BERGEMANN, K.J., KRASNY, R., FORREST, S.R. (2012). Thermal Properties of Organic Light-Emitting Diodes. In: *Organic Electronics*. 2012, vol. 13, 1565–1568. Available at: http://linkinghub.elsevier.com/retrieve/pii/S156611991200184X

203. ZHU, Y. et al. (2016). Synthesis and Electroluminescence of a Conjugated Polymer with Thermally Activated Delayed Fluorescence. In: *Macromolecules*. 2016, vol. 49, 4373–4377. Available at: http://pubs.acs.org/doi/abs/10.1021/acs.macromol.6b00430

204. CAI, X., GAO, B., LI, X.-L., CAO, Y., SU, S.-J. (2016). Singlet-Triplet Splitting Energy Management via Acceptor Substitution: Complanation Molecular Design for Deep-Blue Thermally Activated Delayed Fluorescence Emitters and Organic Light-Emitting Diodes Application. In: *Advanced Functional Materials*. Available at: http://doi.wiley.com/10.1002/adfm.201603520

205. XIE, G. et al. (2016). Polarity-Tunable Host Materials and Their Applications in Thermally Activated Delayed Fluorescence Organic Light-Emitting Diodes. In: *ACS Applied Materials & Interfaces*. acsami.6b08738. Available at: http://pubs.acs.org/doi/abs/10.1021/acsami.6b08738

206. LEE, I., LEE, J.Y. (2016). Molecular Design of Deep Blue Fluorescent Emitters with 20% External Quantum Efficiency and Narrow Emission Spectrum. In: *Organic Electronics*. 2016, vol. 29, 160–164. Available at: http://linkinghub.elsevier.com/retrieve/pii/S1566119915302251

207. ZHANG, Q. et al. (2014). Efficient Blue Organic Light-Emitting Diodes Employing Thermally Activated Delayed Fluorescence. In: *Nature Photonics*. 2014, vol. 8, 326–332. Available at: http://www.nature.com/doifinder/10.1038/nphoton.2014.12

208. KAJI, H. et al. (2015). Purely Organic Electroluminescent Material Realizing 100% Conversion from Electricity to Light. In: *Nature Communications*. 2015, vol. 6, 8476. Available at: http://www.nature.com/doifinder/10.1038/ncomms9476

209. FANG, L. et al. (2016). Fluorine-Containing Low-Energy-Gap Organic Dyes with Low Voltage Losses for Organic Solar Cells. In: *Synthetic Metals*. 2016, vol. 222, 232–239. Available at: http://linkinghub.elsevier.com/retrieve/pii/S0379677916303551

210. LIN, L.-Y. et al. (2011). A Low-Energy-Gap Organic Dye for High-Performance Small-Molecule Organic Solar Cells. In: *Journal of the American Chemical Society*. 2011. vol. 133, 15822–15825. Available at: http://pubs.acs.org/doi/abs/10.1021/ja205126t

211. DOROK, S., WUTKE, J., KLOSE, M., BROTHAGEN, J. (2015). *Google Patents*, 2015. EP Patent App. EP20,130,176,542. Available at: https://encrypted.google.com/patents/EP2826768A1?cl=en

212. WRACKMEYER, M.S., HUMMERT, M., HARTMANN, H., RIEDE, M.K., LEO, K. (2010). Structure–Property Relationship of Acceptor-Substituted Oligothiophenes. In: *Tetrahedron*. 2010, vol. 66, 8729–8733. Available at:

http://www.sciencedirect.com/science/article/pii/S0040402010013293

213. FITZNER, R. et al. (2011). Dicyanovinyl-Substituted Oligothiophenes: Structure-Property Relationships and Application in Vacuum-Processed Small Molecule Organic Solar Cells. In: *Advanced Functional Materials*. 2011, vol. 21, 897–910. Available at: http://doi.wiley.com/10.1002/adfm.201001639

214. CHEN, Y.-H. et al. (2012). Vacuum-Deposited Small-Molecule Organic Solar Cells with High Power Conversion Efficiencies by Judicious Molecular Design and Device Optimization. In: *Journal of the American Chemical Society*. 2012, vol. 134, 13616–13623. Available at: http://pubs.acs.org/doi/10.1021/ja301872s

215. WANG, J., LIU, K., MA, L., ZHAN, X. (2016). Triarylamine: Versatile Platform for Organic, Dye-Sensitized, and Perovskite Solar Cells. In: *Chemical Reviews*. 2016, vol. 116, 14675–14725. Available at: http://pubs.acs.org/doi/abs/10.1021/acs.chemrev.6b00432

7. LIST OF PUBLICATIONS ON THE SUBJECT OF THE THESIS

Scientific publications:

1. **Matulaitis, T.**, Imbrasas, P., Kukhta, N.A., Baronas, P., Bučiūnas, T., Banevičius, D., Kazlauskas, K., Gražulevičius, J.V., Juršėnas, S. (2017). Impact of Donor Substitution Pattern on the TADF Properties in the Carbazolyl-Substituted Triazine Derivatives // Journal of Physical Chemistry C. 2017, vol. 121 (42), pp. 23618–23625.

2. Fang, L., Holzmueller, F., **Matulaitis, T.**, Baasner, A., Hauenstein, C., Benduhn, J., Schwarze, M., Petrich, A., Piersimoni, F., Scholz, R., Zeika, O., Koerner, C., Neher, D., Vandewal, K., Leo, K. (2016). Fluorine-Containing Low-Energy-Gap Organic Dyes with Low Voltage Losses For Organic Solar Cells // Synthetic Metals. 2016, vol. 222, pp. 232–239.

3. **Matulaitis, T.**, Kostiv, N., Grazulevicius, J.V., Peciulyte, L., Simokaitiene, J., Jankauskas, V., Luszczynska, B., Ulanski, J. (2016). Synthesis and Properties of Bipolar Derivatives of 1,3,5-triazine and Carbazole // Dyes and Pigments. 2016, vol. 127, pp. 45–58.

Patents:

1. **Matulaitis, T**, Fang, L., Zeika, O., Körner, C., Leo, K., Holzmüller, F., Vandewal, K. *Organische Donor-Akzeptor-Farbstoffe für die Verwendung in elektronischen und optoelektronischen Bauteilen* (Organic Donor-Acceptor Dyes for Use in Electric and Optoelectronic Devices). DE 10 2014 217 817 A1, German Patent and Trade Mark Office. Date: March 24, 2016.

8. LIST OF PRESENTATIONS AT INTERNATIONAL CONFERENCES

1. **Matulaitis, T.**, Baronas, P., Gražulevičius, J.V., Juršėnas, S. (2017). Isomeric Derivatives of 1,3,5-triazine and Carbazole as Effective Blue Emitters // *12th International Conference on Optical Probes of Organic and Hybrid Semiconductors*, June 19–23, 2017, Quebec, Canada. **Poster presentation**.
2. **Matulaitis, T.**, Gražulevičius, J.V., Volyniuk, D. (2017). Structure-Property Relationship of Bipolar Organic Semiconductors // 60th International Conference for Students of Physics and Natural Sciences *Open Readings* 2017, March 14–17, 2017, Vilnius, Lithuania. **Poster presentation**.
3. **Matulaitis, T.**, Gražulevičius, J.V., Pečiulytė, L., Monkman, A.P. (2016). Carbazole-Benzonitrile Hybrid Materials: a Consistent Study of Optical, Photophysical, Thermal and Electrochemical Properties // *Organic Semiconductors*, September 22–25, 2016, Dubrovnik, Croatia. **Poster presentation**.
4. **Matulaitis, T.**, Gražulevičius, J.V., Volyniuk, D. (2016). Synthesis and Semiconducting Properties of New Bipolar Carbazole and Benzonitrile Derivatives // *ICEPOM-10*, May 23–27, 2016, Ternopil, Ukraine. **Oral presentation**.
5. **Matulaitis, T.**, Gražulevičius, J.V. (2015). Effect of the Spacer on The Thermal Properties of Bipolar Molecular Materials // *Baltic Polymer Symposium 2015*, September 16–18, 2015, Sigulda, Latvia. **Oral presentation**.
6. **Matulaitis, T.**, Gražulevičius, J.V., Reina, J.A. (2014). Synthesis and Liquid Crystalline Behavior of the Novel Star-Shaped Triazine and Carbazole Hybrid Compound // *Baltic Polymer Symposium* 2014, September 24–26, 2014, Laulasmaa, Estonia. **Poster presentation**.
7. **Matulaitis, T.**, Gražulevičius, J.V. (2014). Synthesis and Comparative Study of the Properties of Conjugated Dendritic Triphenylamine End-Capped Derivatives // *Stability, Reliability and Promises of Organic Systems*, August 18–22, 2014, Sonderborg, Denmark. **Poster and oral presentations**.
8. **Matulaitis, T.**, Gražulevičius, J.V. (2014). From D-D-D to D-A-D in the Conjugated Star-Shaped Systems: Synthesis and Comparative Study of the Properties of Star-Shaped Triphenylamine End-Capped Derivatives // *Balticum Organicum Syntheticum* 2014, July 6–9, 2014, Vilnius, Lithuania. **Poster presentation**.
9. **Matulaitis, T.**, Gražulevičius, J.V. (2013). Glass-Forming Dendritic Derivatives of Triphenylamine // *Baltic Polymer Symposium 2013*, September 18–21, 2013, Trakai, Lithuania. **Oral presentation**.

9. ACKNOWLEDGEMENTS

I wish to express my most sincere gratitude to my supervisor and all the colleagues and co-workers with whom I have had great pleasure to work with.